Zur Homepage der Dissertation

Path integral Monte Carlo simulations and their relation to recent advances in nanophysics

Am Fachbereich Physik der Universität Oldenburg
zur Erlangung des Grades eines

Doktors der Naturwissenschaften (Dr. rer. nat.)

angenommene Dissertation von

Jens Harting

geboren am 09.01.1974 in Twistringen.

Erstreferent: PD Dr. Peter Borrmann
Korreferenten: Prof. Dr. Martin Holthaus
Prof. Dr. Matti Manninen

Tag der Disputation: 14. Dezember 2001

Zur Homepage der Dissertation

Path integral Monte Carlo simulations and their relation to recent advances in nanophysics

Am Fachbereich Physik der Universität Oldenburg
zur Erlangung des Grades eines

Doktors der Naturwissenschaften (Dr. rer. nat.)

angenommene Dissertation von

Jens Harting

geboren am 09.01.1974 in Twistringen.

Erstreferent: PD Dr. Peter Borrmann
Korreferenten: Prof. Dr. Martin Holthaus
Prof. Dr. Matti Manninen

Tag der Disputation: 14. Dezember 2001

There is plenty of room at the bottom.

Richard P. Feynman (1960)

Contents

Introduction **1**

I Introduction to path integral Monto Carlo simulations and recent advances in nanotechnology **5**

1 Semiconductor structures – wells, wires, dots, and rings **7**

1 Historical background 7

2 Production techniques 9

2.1 Quantum dots 9

2.2 From dots to rings 11

3 Selected physical properties of few-electron quantum dots 12

4 Theoretical concepts to describe quantum dots 14

2 Path integrals and Monte Carlo simulations **17**

1 The Feynman path integral 17

2 The thermodynamic path integral 18

2.1 The Metropolis Monte Carlo algorithm 21

2.2 Computational problems 23

2.3 Electron densities, pair correlation functions, and energy expectation values 25

3 Convergence and computational effort 27

3.1 Optimizing simulation parameters 27

3.2 Organization of large scale simulations 31

II Application of the path integral Monte Carlo technique on selected systems **33**

1 Interplay between shell effects and electron correlations in quantum dots
J. HARTING, O. MÜLKEN, AND P. BORRMANN
Physical Review B 62, 10207 (2000) **35**

2 Order-disorder transition in nanoscopic semiconductor quantum rings
P. BORRMANN AND J. HARTING
Physical Review Letters 86, 3120 (2001) **41**

3 Multi-functional nano-sized electronic components **47**
1 Introduction 47
2 The double quantum dot 47
3 Logical functions at high temperatures 52
4 Conclusion 55

4 The geometric structure of small sodium clusters **57**
1 Introduction 57
2 The path integral Monte Carlo technique 58
3 Conclusion and outlook 63

III Thermodynamic properties of selected finite systems **65**

1 Calculation of thermodynamic properties of finite Bose-Einstein systems
P. BORRMANN, J. HARTING, O. MÜLKEN, AND E.R. HILF
Physical Review A 60, 1519 (1999) **67**

2 Classification of phase transitions in small systems
P. BORRMANN, O. MÜLKEN, AND J. HARTING
Physical Review Letters 84, 3511 (2000) **73**

3 Classification of phase transitions of finite Bose-Einstein condensates in power law traps by Fisher zeros
O. MÜLKEN, P. BORRMANN, J. HARTING, AND H. STAMERJOHANNS
Physical Review A 64, 013611 (2001) **79**

Bibliography **87**

Acknowledgment **103**

Curriculum Vitae **105**

Statements **107**

Introduction

This thesis consists of three parts and is of cumulative type. It contains a presentation of the results I have obtained in collaboration with my colleagues Peter Borrmann, Oliver Mülken, Eberhard R. Hilf, and Heinrich Stamerjohanns. This introduction gives a short overview of the structure of this thesis.

I Introduction to path integral Monte Carlo simulations and recent advances in nanotechnology

Recently, the words ’nanotechnology’ and ’nanoscience’ have become very popular and can be found in many articles in scientific and popular magazines that cover current research.

From a physics point of view, these articles are usually focused on experimental semiconductor physics, material physics, or the engineering of tiny mechanical machines. Biology and chemistry also offer challenging new possibilities which go beyond the scope of this thesis.

Most of the techniques used to fabricate miniature systems and study them theoretically have been developed in the last few decades [88, 136, 198]. The latest breakthroughs in nanophysics would not have been possible without basic applied research in different fields including atomic, nuclear, solid state, and condensed matter physics.

Nevertheless, in recent years these breakthroughs have lead to a number of fascinating possibilities. Scanning probe microscopes can now be used to monitor and manipulate single atoms on surfaces [59, 155, 220]. Semiconductor physicists have managed to fabricate well-defined structures of nanoscopic size. While most of these systems are far from having a practical use, they give us opportunities to study quantum mechanical effects in great detail.

A boost in this field of research has been provided by the United States Government in establishing nanotechnology as a new national research topic. An interdisciplinary description of the planned research and development in the next decade is presented in a report published by the ’Interagency Working Group on Nanoscience, Engineering and Technology’ (IWGN) [190, 220].

In Chapter I-1 of this thesis a short overview of quantum wells, wires, dots and rings is presented. Following a description of the innovations in experimental research which made the fabrication of these structures possible, the reader is given an introduction into selected theoretical approaches used to study the physical properties of nanoscopic semiconductor structures.

Chapter I-2 contains a description of the path integral Monte Carlo method (PIMC). This technique starts by transforming differential equations to integral equations and makes use of the exact numerical approach instead of analytical approximations. Thus, instead of solving an approximative problem exactly, the true problem is approximately solved to the extent and accuracy the allocated computer resources allow. An explanation of the algorithm we use, as well as a discussion of the advantages and problems of the method are then presented.

In the last chapter of Part I, convergence studies are presented to introduce the reader to the algorithm used to find parameters which are best suited for limiting the computational effort and maximizing the accuracy of the simulations.

II Application of the path integral Monte Carlo technique on selected systems

Part II contains four chapters on the application of the path integral Monte Carlo method to different systems and is the ’heart’ of this thesis.

Two of the chapters, namely ’**Interplay between shell effects and electron correlations in quantum dots**’ [96] and ’**Order-disorder transition in nanoscopic semiconductor quantum rings** [30],’ are reprints of already published articles.

In Chapter II-1, single GaAs quantum dots corresponding to the experiments of Seigo Tarucha et al. are modeled [206] and shell effects and electron correlations of dots with up to 12 electrons are investigated. It is demonstrated that the path integral Monte Carlo method is able to reproduce the experimental addition energies, i.e., the energies necessary to allow additional electrons to enter the dot, and to study the validity of Hund’s rule. Furthermore, detailed studies of Wigner crystallization depending on the temperature and the dielectric constant κ are presented.

Axel Lorke et al. have recently fabricated nanoscopic quantum rings [147]. Next to quantum wires, these systems are probably the best prototypes of quasi one-dimensional quantum systems. By varying the ring diameter or the potential strength, it is possible to tune them from quasi one-dimensional to two-dimensional systems. It is shown in Chapter II-2 that nanoscopic quantum rings with up to eight electrons undergo a smooth transition between spin ordered and disordered Wigner crystals. This transition strongly depends on the chosen ring diameter, temperature and number of electrons inside the ring. Due to the small number of particles, the transition extends over a broad temperature range and is clearly identifiable from the electron-electron pair correlation functions. It is also demonstrated that the addition energies reflect the predicted shell effects and are in good agreement with the results of Warburton et al. [215].

The focus of Chapter II-3, ’**Multi-functional nano-sized electronic components**,’ is on a new approach for utilizing quantum dot molecules as single photon detectors or transistors. Coupled systems of two and three dots of different sizes are utilized to study the effect of spin flipping or adding an additional electron to one of the implied dots on the electron density in a different dot.

In order to develop high performance electronic devices for applications in computing and modern information technology, the number of transistors per chip has to be increased and the power consumption reduced. Quantum dot molecules are very promising candidates to accomplish this task because of their precisely tunable physical properties. The path integral Monte Carlo simulations show that three coupled quantum dots can be utilized to perform logical ’AND’ and ’OR’ operations.

The last chapter that utilizes the path integral Monte Carlo method is Chapter II-4, ’**The geometric structure of small sodium clusters**.’

After a short introduction to the field of clusters and in particular sodium clusters, the method used to study them is presented. The sodium cores including the nucleus and all electrons in closed shells, are treated as classical particles obeying Boltzmann statistics. The valence electrons are described as quantum mechanical particles and the electron-core interaction is modeled by a pseudopotential taken from density functional studies. It is shown in this chapter that the path integral Monte Carlo method is able to reproduce the geometry of small sodium clusters. For Na_3^+ and Na_4^+, the bond lengths are compared with results from other authors.

III Thermodynamic properties of selected finite systems

Part III is only loosely connected to the previous ones. The reprints of published articles presented here are concerned with the thermodynamics of selected finite systems.

In Chapter III-1, ’**Calculation of thermodynamic properties of finite Bose-Einstein systems** [31],’ an exact recursion formula is presented for the canonical occupation number $\eta_i(N, \beta)$ of ideal Fermi- and Bose-gases based on the one-particle energy eigenstates ϵ_i. In addition, a recursion for the fluctuation of the occupation probabilities is derived. The formulae are applicable for canonical systems where the particles can be approximated as noninteracting, e.g., Bose-Einstein condensates in magnetic traps.[1]

To demonstrate the usefulness of the recursion formulae, the specific heat and relative ground-state fluctuations for an ideal Bose-system of ^{4}He atoms with up to 10000 particles are calculated. The atoms are confined by different three-dimensional potentials.

This article already appeared in my graduate thesis [95], but since the recursion formula is used to calculate some of the results in the following chapters, it is included here as well. Furthermore, the algorithm has been utilized for the generation of the exact energy expectation values in Chapter I-3.

---

[1] E.A. Cornell, W. Ketterle, and C.E. Wieman were awarded the Nobel prize in 2001 for the achievement of Bose-Einstein condensation in dilute gases of alkali atoms.

In Chapter III-2, '**Classification of phase transitions in small systems** [34],' the complex zeroes $\mathcal{B}_k = \beta_k + i\tau_k$ of the canonical partition function are used to classify phase transitions in finite systems.

The classification scheme is an extension of the approach of Grossmann et al., who analyzed the distributions of zeros of the canonical partition function in the complex temperature plane in order to describe phase transitions in macroscopic systems [85, 86, 87].

All thermodynamic properties of the system can be expressed by the distribution of zeros. It is pointed out in Chapter III-2 that the thermodynamic properties of a system are determined by the zeros close to the real axis. Three parameters are introduced to describe the distribution of zeros close to the real axis. The shape of the distribution gives rise to different orders of phase transitions.

The new classification scheme is consistent with Ehrenfest's definition in the thermodynamic limit.

As an example of a higher order phase transition in a finite system, the classification scheme is applied to Bose-Einstein condensates in a harmonic trap. Since it is a difficult task to calculate the zeros of the partition function directly, the recursion formula as given in Chapter III-1 is utilized to calculate the ground state occupation number. Because most thermodynamic properties are derivatives of the logarithm of the partition function, the poles of the occupation number correspond to the zeros of the partition function. The finite size effects and order of the phase transition are well reflected by the classification parameters.

By applying the scheme on Argon clusters, the density of zeros helps to understand the complex melting and isomer hopping processes. In the case of this system, the zeros are detected by calculating the specific heat using Monte Carlo methods. Obviously, the poles of the specific heat correspond to the zeros of the partition function as well.

In the following chapter, '**Classification of phase transitions of finite Bose-Einstein condensates in power-law traps by Fisher zeros** [166],' the new classification scheme is applied to finite, non-interacting Bose-Einstein systems in power-law traps with an effective one-particle density of states $\Omega(E) = E^{d-1}$. This is formally equivalent to a d-dimensional harmonic oscillator or a $2d$-dimensional ideal gas. Additionally, the scheme is applied to a Bose-gas in a harmonic potential with discrete energy levels. It is shown that the order of the phase transition sensitively depends on the single-particle density of states, which is generated by the confining potential. Furthermore, even if the thermodynamic properties usually used, for example the specific heat, fail to describe the order of the phase transition properly, the distribution of zeros allows us to clearly classify it.

I

Introduction to path integral Monto Carlo simulations and recent advances in nanotechnology

1 Semiconductor structures – wells, wires, dots, and rings

1 Historical background

In 1974, the production of so-called quantum wells was reported by Chang and Dingle [47, 54]. Quantum wells were the first devices to allow the study of two-dimensional electronic structures. They are very thin, almost flat semiconductor layers sandwiched between two layers of a different semiconductor material with a higher conduction band. Quantum wells are usually fabricated using GaAs and $\mathrm{Al}_x\mathrm{Ga}_{1-x}$ for the barrier layers. The electrons stay inside the enclosed layer because their de-Broglie wavelength – resulting from their small effective mass in semiconductors – is long and restricts the movement to two dimensions. As a consequence, the density of states becomes quantized and after determining the layer thickness belonging to a given energy level, precise electronic characteristics of a device can be designed.

The previously unknown properties of the new two-dimensional systems inspired many researchers. The most popular results are the discovery of the integer quantum Hall effect by K. v. Klitzing [124] and the fractional quantum Hall effect by D.C. Tsui, H.L. Störmer and R.B. Laughlin [144, 211]. Their work was honored with the Nobel prize in 1985 and 1998. Today, the properties of quasi two-dimensional structures are well understood and quantum wells are present in our daily life – for example, in the laser diodes of CD-players and microwave receivers used for satellite television [112, 198].

The next step in confining electrons to a limited number of dimensions was the development of quantum wires by P.M. Petroff and colleagues [180]. These quasi one-dimensional structures were produced by etching stripes in a sample with a quantum well.

The first quantum dots, which made it possible to confine electrons in a quasi 'zero-dimensional' potential, were produced by industrial research centers using lithographic techniques. Soon after the publication of the results from Texas Instruments [188], AT&T [50, 207] and Bell [118] produced quantum dots with diameters from 30 to 250 nm. Since the first objects had the shape of a square and were comparably large, they are also called 'quantum boxes'. Now researchers had devices in which the movement of electrons is quantized in all directions. Due to the small number of unbound electrons in these semiconductor devices, usually only 10 to 100 electrons are captured inside a quantum dot. This is why they are often referred to as 'artificial atoms' or 'quantum dot atoms' [187]. It is possible to very precisely control the shape, structure of electron levels, and the number of confined electrons using, for example, magnetic fields or varying applied voltages. Nevertheless, it is important to keep in mind the main difference between 'artificial' and 'real' atoms: While the attraction of the nucleus holds the electrons inside a real atom, in quantum dots, electrons are trapped within barriers formed by semiconductor materials.

Very shortly after the development of quantum dots, physicists became interested in coupled systems like quantum dot molecules consisting of two or more quantum dots. These coupled systems can nowadays routinely be fabricated in the horizontal plane [173] or as vertical systems with an arbitrary amount of stacked dots [174, 196]. Quantum dot molecules can be used to study new physical phenomena or eventually for quantum computation. As will be shown later in Chapter 3 of Part II, they are also possible candidates for a nano-sized replacement of classical transistors.

Quantum rings of nanoscopic size have been experimentally realized recently by the group of A. Lorke using self-assembly techniques [147]. Nevertheless, mesoscopic circular shaped devices have already been investigated in depth experimentally and theoretically [152, 217, 218]. Next to quantum wires, nanoscopic quantum rings are probably the best prototypes for quasi one-dimensional electron systems. The new experiments of Lorke's group lead researchers to study these new devices and compare the results to the already known properties of quantum dots.

What's next? Due to the great advances in the field of nano-sized semiconductor physics, applications in microelectronics are becoming more and more interesting and promising. The properties of these devices can be controlled very precisely and it is becoming possible to fabricate very tiny structures in order to minimize the amount of space required for electronic circuits. Smaller circuits consume less power than conventional ones and can also be operated at higher speed. Furthermore, more precisely tunable laser diodes and microwave devices will profit from the huge amount of research invested in the study of optical properties of quantum dots and rings.

A very interesting example of the application of quantum wells is the 'quantum cascade laser' built at Bell labs by F. Capasso's group [67] after an original concept by R.F. Kazarinov and R.A. Suris [121]. They grew about 75 layers a few atoms thick on top of each other. A set of three wells is a so-called 'active region'. Depending on the width of the wells, an electron can emit a photon with a specific wavelength while descending from a higher to a lower energy level. The novel characteristic of this kind of laser is that it generates photons from 25 regions, since they are arranged in series. Each region has a lower energy than the one before and in between them are injector/relaxation regions, where the electrons are collected after tunneling out of one active region and before tunneling into the next. With this technique, it is possible to fabricate lasers that cover the full mid-infrared spectrum from 3.4 to 17 μm and that can simultaneously emit several laser wavelengths. In pulsed mode, these devices already work at room temperature and it will probably be possible to use them in continuous mode in the near future. Both modes have already been demonstrated at 80 K. Since the optical power and specific wavelength of quantum cascade lasers have not been available with conventional semiconductor laser diodes before, many new applications are conceivable.

The more precisely a device needs to be controlled, the smaller it has to be in order to minimize phonon couplings. Another breakthrough will be necessary for industrial production to fabricate devices small enough to work at room temperature and make it possible to utilize nanoscopic quantum dots, rings, and wires for popular consumer products. Quantum well lasers and other optoelectronic elements are possible applications for the new devices. Since silicon, which is usually used in the semiconductor industry, is not able to emit light, gallium-arsenide or more complex compounds, which are more expensive, have to be used.

2 Production techniques

2.1 Quantum dots

All techniques described in this section for producing quantum dot structures were made possible by the development of **molecular beam epitaxy (MBE)** in the early 1970s [48, 49]. With this technique, it is possible to routinely fabricate high purity epitaxial layers which are only a few atoms thick.

In an MBE apparatus, the substrates are fixed on a heated rotating holder inside a vacuum chamber (see Fig. 1.1). On the opposite side of the chamber, effusion cells including the materials to be grown are placed and sealed by a shutter system. The molecular beams are created by thermally evaporating the constituents. By opening only one effusion cell at a time, high purity layers can be grown. It is essential that the materials used are very clean and that the whole process takes place in an ultra high vacuum environment. Nearly atomically, transitions of different materials are possible because the growth rates are usually of the order of a few Angstrom per second and hence the beams can easily be shuttered quickly enough.

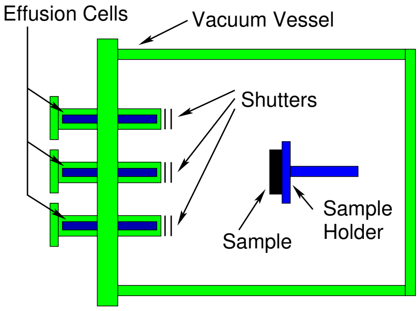

Figure 1.1: Schematic view of a typical MBE setup

The first quantum dots were produced by Reed et al. [188] using **etching techniques** common in the semiconductor industry. They covered a sample containing some quantum wells with a polymer mask and exposed it to an electron or ion beam. Afterwards, the mask was removed at the exposed areas and the whole structure covered with a protective metal film. A special solution was used to remove the polymer and metal films resulting in a clean sample surface. The metal layer only remained at the previously exposed areas and behaved as a protective shield when chemical etching was applied. Using this method, quantum dots with diameters in the range of 10-100 nm were cut out from quantum wells [112]. Etched dots can have almost any shape or size. An example of the different possibilities is shown in Fig. 1.2 [133].

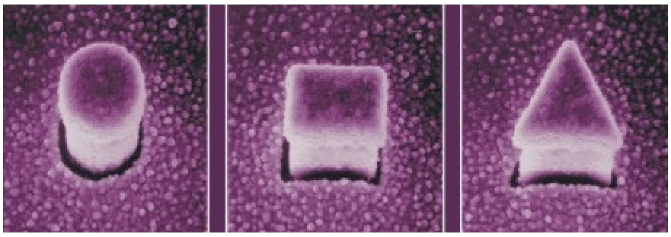

Figure 1.2: Possible shapes of quantum dots as fabricated by L. Kouwenhoven's group [133]. The dots have a width of about 0.5μm.

Edge effects are one of the limitations of quantum dots which are fabricated by etching techniques. One can overcome this problem by using lithography to create tiny electrodes on top of a semiconductor surface. A **spatially modulated electric field** can be obtained in this way [10]. The electrons are localized in a small area between the electrodes. This technique also makes it possible to fabricate additional structures around the dot for further measurements or experiments. For example, small microwave antennas are suitable for spectroscopy [22] or sources of magnetic fields can be produced to study the field dependence of a dot. Another advantage of the use of spatially modulated electric fields is that the parameters of the confining potential can be varied easily by changing the applied voltages. A quantum dot used by Folk et al. [74] which was produced with the aid of this technique is shown in Fig. 1.3.

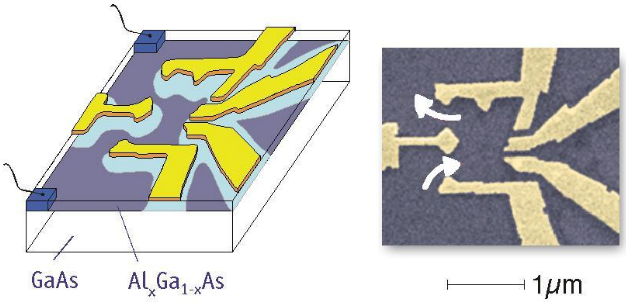

Figure 1.3: On the left is a schematic drawing of Folk's quantum dot. The right picture shows a scanning electron micrograph of the same device. The lateral confinement is achieved by applying a negative voltage to the metal electrodes. Electrons can enter or leave the dot through two leads (white arrows) [74].

A novel approach is the use of atomic force microscopes for patterning the surface by **local anodic oxidation**. In a humid surrounding, the tip of the microscope is biased on top of the surface. Under some conditions, the surface can be oxidized and hence electronically modified [149].

Ekimov et al. [64] have shown that it is possible to fabricate quantum dots out of semiconductor **crystals embedded in glass dielectric matrices**. They doped silicate glass with semiconducting copper compounds and heated it for a few hours at several hundred degrees. Crystals of almost equal size formed and their diameters were defined by the temperature and heating time.

A focused laser beam is an ideal candidate to **heat two sandwiched quantum wells of different materials locally**. Moving the laser around a small area results in an interdiffusion of atoms from one well to the other. As demonstrated by Brunner et al., the band structure is modified at the borders and a quantum dot emerges between the illuminated areas [39].

Selective Growth utilizes a material with a wider band gap (for example AlGaAs) covered by a mask [78]. Miniature triangles are etched in the sample. Using chemical vapor deposition, small pyramids are grown on the areas not covered by the mask. The first layers of the pyramids usually consist of the substrate material and only the top is made of a semiconductor material with a narrower band gap (for example GaAs). The advantage of using the substrate compound for the bottom of the pyramids is the ability to fabricate dots with diameters of some tens of nanometers.

Self-assembled or **self-organized** quantum dots enabled experimenters to fabricate very small dots of nanometer proportions. The sizes and shapes are very uniform and, due to a perfect crystal structure, there are no impurity effects. Furthermore, no complicated deposition of electrodes or etching are necessary, facilitating the production process substantially. This technique was introduced in 1994 by P.M. Petroff et al. [179] and is presently the most promising technique for smaller and more sophisticated semiconductor structures. Self assembling techniques utilize different lattice constants of the substrate and the crystallized material. A very common combination is GaAs and InAs. Only the first deposited monolayers crystallize in a strained way with a lattice constant equal to the substrate's. The strain results in a breakdown of this order as soon as a critical thickness is reached. Randomly arranged islands of regular shape and size start to form. This phase transition is called Stranski-Krastanow transition and was first published in 1939 [203]. Depending on the materials used, the temperature, and the growth rate, the islands have the shape of pyramids, lenses, or droplets. Figure 1.4 shows an AFM image of PbSe quantum dots on PbTe of the group of G. Springholz [199].

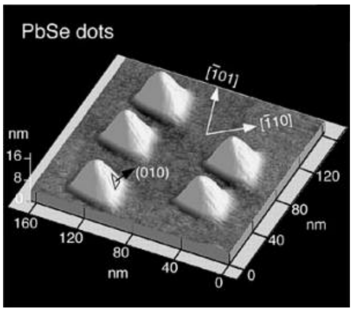

Figure 1.4: AFM image of self-assembled PbSe quantum dots on PbTe by Springholz et al. [199].

2.2 From dots to rings

Semiconductor quantum rings were fabricated shortly after the creation of the first quantum dots. They provide an opportunity to study quasi one-dimensional quantum systems in detail. These rings have been produced using lithographic techniques and were rather big, i.e. the diameters were a few hundred nanometers or even micrometers.

To study the influence of strong quantum effects on ring-shaped systems, the diameter has to be decreased to orders of magnitude which cannot be achieved using lithography.

As known from quantum dots already, self-assembling techniques are very promising if one seeks to achieve miniature scale. A. Lorke's and P.M. Petroff's groups have succeeded in applying a modified procedure and assembling the first nanoscopic semiconductor rings [147].

They grew self-assembled InAs quantum dots on a GaAs layer and covered them with another thin GaAs layer. Annealing the sample at growth temperature for about one minute resulted in a drastic change of the morphology: The lens-shaped dots became 'volcanos' with an increased lateral size, a reduced height and a well defined center hole. The thickness of the cover layer has a great influence on the results since it is responsible for the size and the structure of the resulting rings. Figure 1.5 shows a sample with rings of 50 nm diameter.

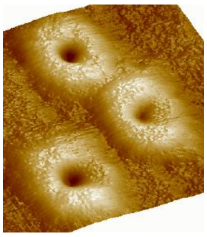

Figure 1.5: A sample with nanoscopic InAs quantum rings as described in [147].

3 Selected physical properties of few-electron quantum dots

Experimenters have managed to fabricate different kinds of quantum dots with very different physical properties. For example, it is important to distinguish between open dots, i.e., devices with attached point contacts allowing classical movements of electrons across the dot-lead junctions, and closed dots. In closed dots, conductance only occurs by tunneling because the contacts are pinched off. This thesis focuses on closed dots only. In these nearly isolated dots, the low-lying energy levels are discrete because the mean free path for electrons is larger than the typical diameter of a dot. Their discrete excitation spectra motivated Kastner [120] and Ashoori [9] to introduce the term 'artificial atom'. This term must be used with caution. It is correct in the sense that a dot contains a fixed number of electrons. For example, 'quantum-dot helium' is widely used to describe dots containing two electrons [103]. But in contrast to real atoms, individual semiconductor structures never show identical physical properties. Due to irregularities in fabrication, the confining potential is slightly different for each device. Additionally, in atoms, the Coulomb interaction between nucleus and electrons is much more dominant than the electron-electron interaction, which is, of course, the only correlation in quantum dots. Due to the very shallow confining potential compared to atoms, long range electron interactions and correlations are important effects in quantum dots.

As described in previous sections, quantum dots are created mainly through lateral confinement restricting the motion of the electrons inside a very narrow quantum well. Usually, they have the shape of flat disks, with diameters much larger than the thickness of the quantum well. Since the energy of single-particle excitations across the dot is significantly larger than other characteristic system energies, the confining potential can be considered two-dimensional. The potential strongly depends on the production technique of the dot. While large etched dots can be thought of as rectangular wells with rounded edges, small ones might be modeled by simpler smooth potentials. For nanoscopic self-assembled dots as studied later in this thesis, a parabolic well seems to be a fairly good approximation. In this case, the Hamiltonian for N electrons is given by

$$H = \sum_{i=1}^{N} \left(\frac{\mathbf{p}_i^2}{2m^*} + \frac{m^* \omega_0^2 \mathbf{r}_i^2}{2} \right) + \sum_{i<j=1}^{N} \frac{e^2}{\kappa |\mathbf{r}_i - \mathbf{r}_j|}, \tag{1.1}$$

where m^* is the effective mass, ω_0 the strength of the potential, and κ the dielectric constant of the material. S. Tarucha's experimentally achieved parameters [206] are commonly found in theoretical papers to describe GaAs dots (κ = 12.9, $\hbar\omega_0$ = 3 meV, m^* = 0.067 m_e).

The classical Coulomb repulsion of the electrons already inside the dot usually blocks the tunneling of electrons into it. Thus, the conductance is small, but changing the gate voltage can compensate the Coulomb blockade and, at an appropriate voltage, the number of electrons inside the dot fluctuates between N and $N + 1$. This results in a maximum of conductance. A plot of the current passing through the dot over the gate voltage at sufficiently low temperatures shows sharp and uniformly spaced conductance peaks. The difference of the gate voltage of these peaks is proportional to the charging energy E_C and allows the calculation of the so-called addition energies [206]

$$\Delta E_N = E_{N+1} - 2E_N + E_{N-1}. \tag{1.2}$$

In summary, the addition energy is the energy needed to place an additional electron in the dot.

Shell effects are one of the most interesting topics in quantum dot behavior. The three-dimensional spherical symmetric potential around atoms results in completely filled shells at atomic numbers 2,10,18,..., which are known as 'magic numbers'. Within a shell, Hund's rule explains the value of the spin of an additionally added electron. The quantum dots studied here are described by a two dimensional potential with the magic numbers 2,6,12,..., which are lower because of the lower degree of symmetry [159]. In the style of the periodic table of the elements, some experimentalists from the university of Delft / Netherlands and NTT in Kanagawa / Japan introduced a periodic table for quantum dots [133].

4 Theoretical concepts to describe quantum dots

Different techniques have been applied to describe theoretically the behavior of electrons in quantum dots. These include among others exact diagonalization, Hartree-Fock approximations, density functional theory, random-matrix theory and quantum-chaotic approaches. Since a detailed description of these techniques would go beyond the scope of this thesis, only some concepts of the most common techniques can be covered. For further reading, the existing review articles and books are recommended (for example [4, 5, 94, 104, 112, 114, 133, 134, 198]).

Exact numerical diagonalization has been performed by different groups [3, 99, 154, 160, 175, 181], but is usually limited to less than five electrons. Quantum dot helium, i.e., a dot including two electrons, is probably the best studied system. It is already a difficult task to solve the problem for the ground state. Nevertheless, exact diagonalization approaches have been successful in describing the dependence of electron-electron correlations on strong magnetic fields. Even before the first quantum dots were fabricated, exact diagonalization has been applied to electrons in harmonic systems. For example, Laughlin, Girvin and Jach assumed spin polarized electrons occupying a single Landau level [81, 145].

Mean field approaches such as, for example, the **Hartree-Fock approximation (HF)** [73, 97, 98] are well known from nuclear, atomic, and molecular physics. Different groups have shown that these techniques are also applicable to two dimensional quantum dots [77, 167, 181, 189, 225].

In the Hartree-Fock framework, all electrons and interactions are taken into consideration using the exact many particle Hamiltonian. A Hartree potential is introduced describing the interaction between electrons as an effective external potential.

From the quantum mechanical variational principle it is known that the expectation value of the Hamiltonian for an arbitrary wave function is at least as high as its lowest eigenstate [208]. The simplest possible approach to approximate the many-particle wave function is a single Slater determinant. The wave functions can usually be expanded using Gaussian basis sets. One solves the corresponding eigenvalue problem using the approximated wave function. The obtained energy eigenvalue is minimized by adapting the coefficients of the Gaussian basis sets. In this way, the problem is solved self-consistently. The lowest energy that can be found using the optimal tuned basis set corresponds to the best approximation of the many-particle wave-function.

A distinction is normally made between restricted and unrestricted calculations, corresponding to fixed angular momenta or included spin interactions.

It has been shown that the Hartree-Fock approach is able to handle quantum dots with 40 electrons and to reproduce shell effects, addition energies and the behavior in magnetic fields qualitatively well, but due to the approximations of the wave function, Hartree-Fock results have to be handled with caution: For example, Hartree-Fock calculations predict Wigner crystallization for higher densities than exact Monte Carlo studies [58, 189, 225]. In addition, restricted Hartree-Fock simulations produce energies which strongly deviate from exact studies [181].

Configuration interaction (CI) expansions include electron correlations beyond the single Slater determinant approach. In a systematic way, the many-particle wave function is expanded to a sum of determinants representing different electronic configurations. This approach has also been applied to quantum dots [154] and quantum rings [131].

Density functional theory (DFT) was introduced in 1964 and 1965 by P. Hohenberg, W. Kohn and L.J. Sham [110, 128]. For his pioneering work on density functional theory, W. Kohn won the Nobel prize in 1998 [126, 127].

In DFT, the electron density distribution, and not the many particle wave function is the variable of interest. This is displayed in particular in the basic lemma of Hohenberg and Kohn, who pointed out that the ground state density $\rho(\mathbf{r})$ of a system determines its Hamiltonian uniquely [110]. The Hohenberg-Kohn variational principle states that the energy functional

$$E_v[\rho'(\mathbf{r})] = \int V(\mathbf{r})\rho'(\mathbf{r})\mathrm{d}\mathbf{r} \, + T[\rho'(\mathbf{r})] + \frac{1}{2}\int \frac{\rho'(\mathbf{r})\rho'(\mathbf{r}')}{|\mathbf{r}-\mathbf{r}'|}\mathrm{d}\mathbf{r}\,\mathrm{d}\mathbf{r}\,' + E_{\mathrm{xc}}[\rho'(\mathbf{r})] \quad (1.3)$$

is minimized by $\rho(\mathbf{r})$ at the true ground state energy.

Here, $T[\rho'(\mathbf{r})]$ corresponds to the kinetic energy of the ground state of noninteracting electrons in a potential $V(\mathbf{r})$ with density distribution $\rho'(\mathbf{r})$. $E_{\mathrm{xc}}[\rho'(\mathbf{r})]$ is the exchange correlation energy functional.

This problem is self-consistently solved by the single particle Kohn-Sham equations

$$\left(-\frac{\hbar^2}{2m}\nabla^2 + V_{\mathrm{eff}}\right)\varphi_j(\mathbf{r}) = \epsilon_j\varphi_j(\mathbf{r}), \quad (1.4)$$

with

$$\rho(\mathbf{r}) = \sum_{j=1}^{N_e} |\varphi_j(\mathbf{r})|^2, \quad (1.5)$$

where the sum is calculated for the N_e lowest eigenvalues, to take into account the Pauli exclusion principle.

The effective potential V_{eff} is the sum of the confining external potential, the Hartree potential of the electrons and the derivative of the exchange correlation energy functional.

In principle, this theory is exact for the exact E_{xc}. Since E_{xc} is not known, the usefulness of this algorithm strongly depends on its approximation. A popular approach is the local density approximation (LDA), where the exchange-correlation energy is obtained from precise simulations of the many-electron interactions in a uniform, interacting electron gas [42, 45].

Several authors applied the density functional theory to quantum dots [106, 132, 151, 202]. They have studied the spin ordering behavior as well as the formation of Wigner crystals for systems including more than 50 electrons [106]. The results have to be handled with caution. For example, while Koskinen et al. predicted spin density waves

[132], Hirose and Wingreen questioned their findings, suggesting they may be a computational artefact [106].

The main weakness of density functional theory is in the approximation of the functional for the exchange correlation energy. Slightly different forms of the functional may yield different results. In chemistry, this led to the development of empirical functionals with parameters adjusted to produce the best possible results for a given problem [176].

In the next chapter, a technique is presented which overcomes the difficulties due to the approximations used by other methods. The path integral Monte Carlo technique (PIMC) allows us to study quantum systems without approximations. The complete many-body wave function is sampled by Feynman's approach and the method is limited only by the numerical effort and the exactness of the external potential and material constants. It makes it possible to study temperature dependent effects, and the potential and kinetic energies are naturally included.

2 Path integrals and Monte Carlo simulations

In a visionary talk at the annual meeting of the American Physical Society in 1959, Richard P. Feynman amazed the audience with his vision of extreme miniaturization [70]. He argued that it is possible to write all 25000 pages of the Encyclopedia Britannica in an area of the size of a pin head, just using an 'atomic pen'. He dreamed of small machines building even smaller and smaller ones on an atomic scale. Today's research is quite close to his predictions: Single atoms can be manipulated or motivated to self-assemble in nearly any desired structure. In systems of atomic sizes, quantum mechanical effects arise and the systems can no longer be described by classical theories. In this thesis it will be demonstrated that Feynman's path integral formalism, which he developed more than ten years before his famous talk [69], is well suited to study these tiny systems. The huge computational effort path integral calculations require, favors the utilization of modern computers in studying the physical properties of nanoscopic systems in great detail.

This chapter provides an introduction to the method, its advantages, possibilities, and limitations.

1 The Feynman path integral

Richard P. Feynman developed the fundamental concepts of the path integral formalism while teaching a graduate course at Princeton. A few years later, he looked for previous work on a connection between quantum mechanics and the classical Hamilton's principle function S. One of his colleagues pointed out that P.A.M. Dirac [55, 56, 57] had published that a connection exists between the exponent of the time integral of the classical Lagrangian,

$$\exp\left(\int_{t_1}^{t_2} \mathrm{d}t\, L(x,\dot{x},t)\right) = \exp S, \tag{2.1}$$

and the transition amplitude of a quantum mechanical wave function at two points in space and time $\langle x_2, t_2 \mid x_1, t_1\rangle$. While Dirac did not know exactly what this connection looks like, after a brief analysis Feynman found that it is given by an integral over all possible paths between the space-time positions (x_1, t_1) and (x_N, t_N) [69, 71]

$$\langle x_2, t_2 \mid x_1, t_1\rangle = \int_{x_1}^{x_N} \mathcal{D}[x(t)] \exp\left(\frac{i}{\hbar}\int_{t_1}^{t_2} \mathrm{d}t\, L(x,\dot{x},t)\right). \tag{2.2}$$

Feynman wrote down the first path integral in 1942 in his PhD thesis and published the concepts in 1948 [69].

The paths in Eq. (2.2) are discretized by introducing $(\Delta t = (t_N - t_1)/N)$ and writing the integral as

$$\int_{x_1}^{x_N} \mathcal{D}[x(t)] = \lim_{N\to\infty} \left(\frac{m}{2\pi i\hbar\,\Delta t}\right)^{(N-1)/2} \int \mathrm{dx}_{\,N-1} \int \mathrm{dx}_{\,N-2} ... \int \mathrm{dx}_{\,2}. \tag{2.3}$$

Schrödinger's equation, Heisenberg's matrix formalism and Feynman's path integral are equivalent formulations of quantum mechanics. While Schrödinger's differential equation determines the state of a system at a given time from the state at an infinitesimal time before, the path integral formalism utilizes a different approach: The trajectory of a quantum mechanical particle in space-time is not described by a single classical path, but by the sum of all possible paths between two points. It can be inferred from Eq. (2.2) that the probability of each possible path is given by the exponential of the classical action in units of $\hbar$. If the action of a path increases, the weight becomes smaller. For macroscopic systems, the action of paths far away from the classical trajectory becomes huge and the corresponding probability vanishes. In this case, only one path contributes, which is equivalent to Hamilton's least action principle

$$\delta \int_{t_1}^{t_2} \mathrm{dt}\, L(x, \dot{x}, t) = 0. \tag{2.4}$$

Figure 2.1 shows a comparison of the paths of a classical, quasi-classical and a quantum mechanical system. For classical systems, Eq. (2.2) determines the classical path. In a semi-classical system, mainly those paths close to the classical one are important. Since the contributions of more distant paths are very small, they can usually be ignored. In quantum mechanical systems, the entire range of paths has to be taken into account.

2 The thermodynamic path integral

A physical system in a heat bath of temperature T can be described by the quantum statistical canonical ensemble. The expectation value of an arbitrary observable $X(\mathbf{r})$ is given by

$$\langle X \rangle = Z^{-1} \mathrm{Tr}\left(X(\mathbf{r})\rho(\mathbf{r}, \mathbf{r}')\right), \tag{2.5}$$

where

$$\rho(\mathbf{r}, \mathbf{r}') = \langle \mathbf{r} | \exp(-\beta H) | \mathbf{r}' \rangle, \tag{2.6}$$

is the density matrix and

$$Z = \mathrm{Tr}\rho(\mathbf{r}, \mathbf{r}') = \mathrm{Tr}\left(\exp(-\beta H)\right) \tag{2.7}$$

is the canonical partition function. H is the Hamiltonian and the inverse temperature β is given by $1/T$.

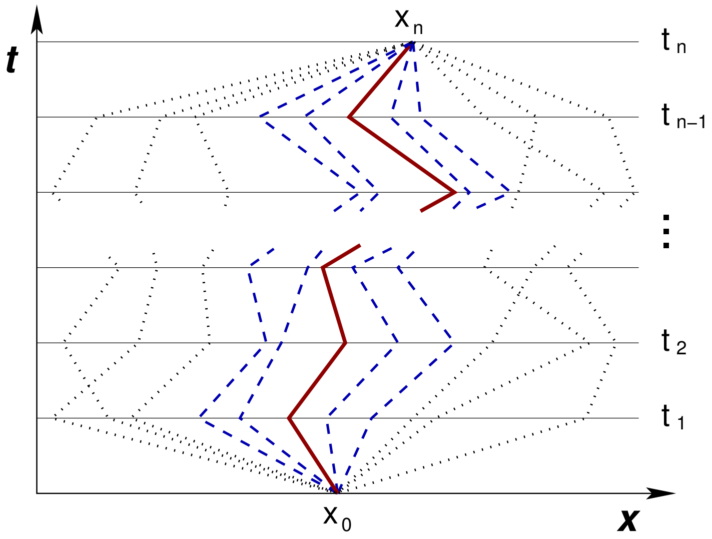

Figure 2.1: Possible paths of a system: The solid line represents the classical trajectory and the dashed lines represent some semi-classically important paths. Paths that are far away from the classical trajectory contribute in quantum mechanics (dotted).

The fact that H usually contains two possibly non-commutating parts H_0 and H_1, representing the kinetic and the potential energy operators, presents a serious problem for the calculation of the density matrix. A very common approach to solve this problem is to separate the two parts of the Hamiltonian. Using the exact operator identity one gets

$$\exp\left(-\beta(H_0+H_1)\right) = \exp\left(-\beta H_0\right)\exp\left(-\beta H_1\right)\exp\left(-\frac{\beta^2}{2}[H_0,H_1]\right). \tag{2.8}$$

This equation can be rewritten

$$\exp\left(-\beta(H_0+H_1)\right) = \left(\exp\left(-\frac{\beta}{M}H_0\right)\exp\left(-\frac{\beta}{M}H_1\right)\exp\left(-\frac{\beta^2}{2M^2}[H_0,H_1]\right)\right)^M \tag{2.9}$$

and it has been shown by E. Trotter [210] that the commutator term becomes much smaller than the others for $M \to \infty$ and can thus be ignored

$$\exp\left(-\beta(H_0+H_1)\right) = \lim_{M\to\infty}\left(\exp\left(-\frac{\beta}{M}H_0\right)\exp\left(-\frac{\beta}{M}H_1\right)\right)^M + \mathcal{O}\left(\frac{\beta^3}{M^2}\right). \tag{2.10}$$

This equation is correct to the order $(\beta^3 M^{-2})$. A mathematical proof of Trotter's product formula is given in [191] and a more detailed description can be found in [44, 53, 123]. In the style of the previous section, the parameter M is usually called the number of 'timeslices'.

Using Trotter's approach, the partition function can be written as

$$Z = \mathrm{Tr}\left[\lim_{M\to\infty}\left(\exp\left(-\frac{\beta}{M}H_0\right)\exp\left(-\frac{\beta}{M}H_1\right)\right)^M + \mathcal{O}\left(\frac{\beta^3}{M^2}\right)\right], \tag{2.11}$$

with

$$H_0 = -\frac{\hbar^2}{2m}\frac{\partial^2}{\partial \mathbf{r}^2} \qquad \text{and} \qquad H_1 = V(\mathbf{r}). \tag{2.12}$$

For slowly varying potentials, Takahashi and Imada have shown that replacing the potential energy term by an effective potential reduces the computing time significantly [53, 130, 205]. They introduced

$$H_1' = H_1 + \frac{1}{24}\left(\frac{\beta}{M}\right)^2 [H_1,[H_0,H_1]], \tag{2.13}$$

which in the case presented here is identical to

$$H_1' = V(\mathbf{r}) + \frac{\hbar^2}{24m}\left(\frac{\beta}{M}\right)^2\left(\frac{\partial V(\mathbf{r})}{\partial \mathbf{r}}\right)^2. \tag{2.14}$$

Utilizing this approach, the error is of the order $(\beta^5 M^{-4})$.

Defining periodic boundary conditions $\mathbf{r}(M+1) = \mathbf{r}(1)$, an equation equivalent to Feynman's approach [69] for the partition function of a one particle system in position space can be found [27, 204]

$$\begin{aligned} Z = &\int \left[\prod_{\gamma=1}^{M} \mathrm{d}\mathbf{r}\,(\gamma)\right] \prod_{\alpha=1}^{M} \Bigg(\langle \mathbf{r}(\alpha+1)|\exp\left(-\frac{\beta}{M}H_0\right)|\mathbf{r}(\alpha)\rangle \\ &\times \langle \mathbf{r}(\alpha)|\exp\left(-\frac{\beta}{M}H_1\right)|\mathbf{r}(\alpha)\rangle\Bigg) + \mathcal{O}\left(\frac{\beta^3}{M^2}\right) && (2.15)\\ = &\left(\frac{Mm}{2\pi\beta\hbar^2}\right)^{3M/2} \int \left[\prod_{\gamma=1}^{M} \mathrm{d}\mathbf{r}\,(\gamma)\right] \Bigg(\exp\Bigg(-\sum_{\alpha=1}^{M}\frac{Mm}{2\beta\hbar^2}(\mathbf{r}(\alpha+1)-\mathbf{r}(\alpha))^2 \\ &-\frac{\beta}{M}\sum_{\alpha=1}^{M} V(\mathbf{r}(\alpha))\Bigg)\Bigg) + \mathcal{O}\left(\frac{\beta^3}{M^2}\right). && (2.16) \end{aligned}$$

For $M \to \infty$ this equation becomes exact and coincides with the famous formula of Kac and Feynman [115, 116]. The number of timeslices M is the source of the relative error of the simulation. While the kinetic energy term in Eq. (2.16) is proportional to M/β, the potential energy term is proportional to β/M. To achieve a uniform convergence of both parts of Eq. (2.16), the quotient β/M is kept constant. This results in a higher number of timeslices for low temperatures and in an increasing computational effort.

The corresponding energy expectation values of the system can easily be calculated by appropriate differentiation of the partition function:

$$\begin{aligned} E =& -\frac{1}{Z}\frac{\partial Z}{\partial \beta} && (2.17)\\ E_{\mathrm{kin}} =& -\frac{m}{\beta Z}\frac{\partial Z}{\partial m} && (2.18)\\ E_{\mathrm{pot}} =& E - E_{\mathrm{kin}} && (2.19) \end{aligned}$$

For a system of N electrons in an external potential, the Feynman path integral can be written as [204]

$$\begin{aligned} Z = \left(\frac{1}{N!}\right)^{M} \int \left[\prod_{\gamma=1}^{M}\prod_{i=1}^{N} \mathrm{d}\mathbf{r}_{\,i}(\gamma)\right] \prod_{\delta=1}^{M} \det(A(\delta,\delta+1)) \\ \times \exp\left(-\frac{\beta}{M}\sum_{\alpha=1}^{M} V(\mathbf{r}_1(\alpha),\ldots,\mathbf{r}_N(\alpha))\right) + \mathcal{O}\left(\frac{\beta^3}{M^2}\right), \qquad (2.20) \end{aligned}$$

with the $N \times N$-dimensional matrix

$$(A(\alpha,\alpha+1))_{k,l} = \begin{cases} \langle \mathbf{r}_k(\alpha) \mid \exp\left(-\frac{\beta}{M}\frac{\mathbf{p}^2}{2m}\right) \mid \mathbf{r}_l(\alpha+1)\rangle & : \quad s_k = s_l \\ 0 & : \quad s_k \neq s_l \end{cases} .$$

$s_{k/l} = \pm 1/2$ denotes the spin of the electron and is usually referred to as '↑' for $s = 1/2$ and '↓' for $s = -1/2$.

2.1 The Metropolis Monte Carlo algorithm

In 1953, Metropolis et al. presented a new method for the numerical calculation of integrals [161]. Today, the Metropolis Monte Carlo algorithm is commonly used to solve multidimensional integrals [19, 20, 21, 117, 135].

A substantial amount of numerical effort is required to solve integrals with dimension d greater than one, and most standard methods fail at this point. This is due to the number of function evaluations needed to sample a d-dimensional space. The number of function evaluations increases as the dth power of the number needed for a one-dimensional integral [184].

The Metropolis Monte Carlo approach uses the evaluation of the integrand at a limited number of representative points, and estimates its integral based on this sample.

To calculate the integral in Eq. (2.20), a random start configuration Ξ_0 is assumed. The ith step of a random walk is realized by generating a new random particle configuration Ξ'. This configuration is accepted if the condition

$$\left|\frac{W(\Xi')}{W(\Xi_i)}\right| > \zeta \tag{2.22}$$

is fulfilled. If it is accepted, Ξ' becomes the new Ξ_i for the next step. Here, ζ is a random number between 0 and 1 and W is the weight function which corresponds to the integrand in Eq. (2.20). It is important to use the absolute values of the weight function because the determinant in W can be negative in the fermionic case.

To improve the convergence, three different kinds of random moves are introduced in our path integral Monte Carlo implementation:

In microscopic moves, all timeslices of all particle coordinates are moved separately by a random vector $\Delta\mathbf{a}$

$$\mathbf{r}_i(\alpha) \longrightarrow \mathbf{r}_i(\alpha) + \Delta\mathbf{a}. \tag{2.23}$$

In a macroscopic move, the whole path for one particle is moved at once by a constant vector $\Delta\mathbf{b}$

$$\mathbf{r}_i(\alpha) \longrightarrow \mathbf{r}_i(\alpha) + \Delta\mathbf{b}, \quad \alpha = 1...M. \tag{2.24}$$

The macroscopic moves are used to provide a fast scan of the configuration space.

For the simulations presented in Chapters II-2 to II-4, we also introduced the movement of the whole path of all particles at once to achieve even better convergence

$$\mathbf{r}_i(\alpha) \longrightarrow \mathbf{r}_i(\alpha) + \Delta\mathbf{c}, \quad \alpha = 1...M, i = 1...N. \tag{2.25}$$

The step lengths for microscopic and macroscopic moves are adjusted in a way that the quotient of accepted and rejected moves stays within an acceptable limit. In our case the rate of acceptance is between 0.5 and 0.6.

The method of moving paths or parts of a path can be changed to nearly any desired procedure. Many different types of moves make the algorithm more robust because before starting a simulation, one does not necessarily know which kinds of moves will lead to a rapid movement through configuration space.

Expectation values of any physical observable $X(\mathbf{r})$ can be evaluated with

$$\langle X \rangle = \frac{\sum_{g=1}^{G} X_g \mathrm{sgn}(W_g)}{\sum_{g=1}^{G} \mathrm{sgn}(W_g)}, \tag{2.26}$$

where X_g is the value of the observable X in the gth Monte Carlo step [33].

Figure 2.2 displays a typical single path for one electron in a quantum ring as described in Chapter II-2.

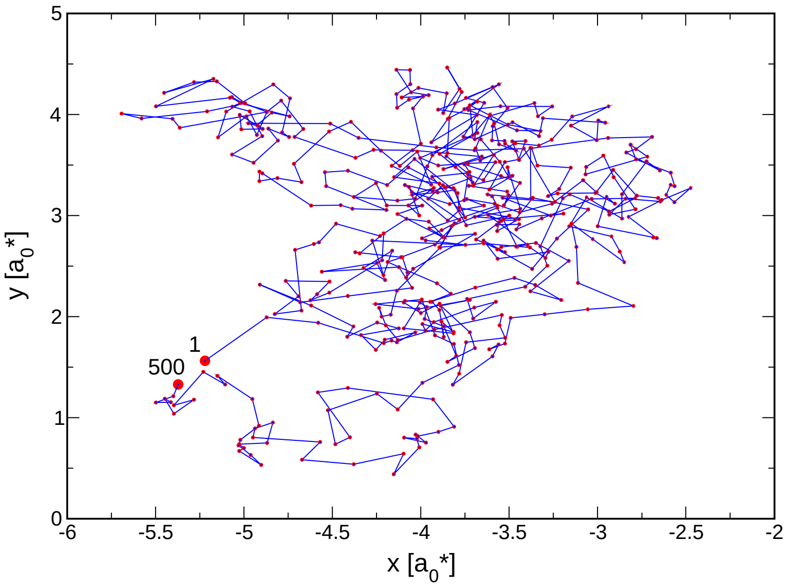

Figure 2.2: A single path of one electron in a quantum ring as described in [30]. The first (1) and the last (500) time step are marked and during this snapshot, the electron stays in the upper left area of the ring which has its center at the origin (Note the tick labels).

2.2 Computational problems

The calculation of Eq. (2.26) is connected to a serious problem of the path integral Monte Carlo formalism. For bosonic systems, $\mathrm{sgn}(W_g)$ is always positive and the expectation value is given by

$$\langle X \rangle = \frac{1}{G} \sum_{g=1}^{G} W_g X_g. \tag{2.27}$$

For fermionic systems, the sign can be negative and for lower temperatures, the ratio of negative signs approaches fifty percent. In this case, Eq. (2.26) does not converge. This so-called ’fermion-sign problem’ is the most serious problem not only in path integral Monte Carlo simulations, but also in other different quantum Monte Carlo approaches [43, 71, 75, 107, 150]. It is the reason for the enormous amount of Monte Carlo steps needed for the systems presented in Part II.

It can be shown that the ratio of integrands in the path integral with positive sign (W^+) and negative sign (W^-) is approximately given by [163, 172]

$$\frac{W^+ - W^-}{W^+ + W^-} \sim \exp[-\beta(E_F - E_B)]. \tag{2.28}$$

E_F and E_B are the ground state energies of the Fermi system and the corresponding Bose system where the bosonic ground state energy is below the fermionic ground state. As explained by I. Morgenstern [163], at low temperatures the simulation spends most of the time below E_F and these obviously unphysical states have to be canceled out. Therefore, the number of positive and negative signs becomes almost equal causing the statistical error in Eq. (2.28) to grow rapidly at low temperatures. This error is amplified by the fact that by increasing the system size, the energy difference $(E_F - E_B)$ also grows. To reduce the influence of the fermion sign problem, Morgenstern suggests avoiding low-lying states by introducing a low lying energy barrier. Indeed, this approach must be handled with care. Using a wrong barrier might allow low-lying bosonic states to be included without being canceled out and thus might falsify the results.

To achieve convergence of Eq. (2.26) even at low temperatures, a completely uncorrelated generation of the Monte Carlo steps is essential. The results of a simulation will be inaccurate if the particle coordinates are moved using a repeating sequence. It has been found that the 24 or 32 bit pseudo random number generators from standard system libraries are not sufficient for the simulations presented in this thesis. Therefore, a new 53 bit pseudo random number generator of Marsaglia-Zaman type developed by P. Borrmann has been applied.

While the determinant in Eq. (2.20) is the most expensive computational task in path integral Monte Carlo simulations, the permanent is also problematic. To our knowledge, there is no effective way to calculate it analytically for larger systems without approximations [44, 101]. Nevertheless, it has been demonstrated that it is possible to circumvent the direct calculation of the permanent using Monte Carlo approaches (for example by using the 'importance sampling of permutations' [204]).

For fermionic systems, the determinant has to be calculated $N \times M$ times for every complete microscopic motion. The linear algebra package LAPACK[1] provides routines for computing the determinant of a matrix, after the matrix has been decomposed into LU factors. These routines utilize pivoting as an attempt to improve accuracy by choosing the most suitable column or row for use during a single step of the algorithm. Due to the pivoting, it is more costly to calculate the determinant than by direct calculation. However, at low temperatures the ratio of signs is around 0.99 and convergence can only be achieved if the determinants are calculated very accurately [96].

The effort of algorithms calculating the determinants of a complete microscopic motion usually grows with the cube of the particle number. In our case, each change of a microscopic particle coordinate affects only one row of the matrix $A(\alpha+1,\alpha)$ and the corresponding column of $A(\alpha,\alpha-1)$. The numerical effort to update the LU factorization of a matrix after a row or column exchange is proportional to the square of the particle number and thus the numerical effort can be reduced by a factor of N [33]. In the algorithm used in this thesis, this method of minimizing the numerical effort is not implemented. This is justified by two reasons: (i) the routines provided by LAPACK are very accurate and efficient and (ii) the difference in computational effort becomes significant for large matrices only.

---

[1] http://www.netlib.org/lapack/

2.3 Electron densities, pair correlation functions, and energy expectation values

Due to the fact that the Monte Carlo simulation is usually done in position space, the calculation of momentum dependent expectation values is a critical task. This can be explained in the picture of the discretized paths which allow different possibilities of differentiation.

Different algorithms are used to estimate the energy. Two common ones are the Barker estimator [13]

$$E_M^B = \frac{Md}{2\beta} - \frac{Mm}{2\hbar^2\beta^2}\sum_{i=1}^{M}(\mathbf{r}_i - \mathbf{r}_{i+1})^2 + \frac{1}{M}\sum_{i=1}^{M} V(\mathbf{r}_i), \tag{2.29}$$

where d is the dimensionality of the system, and the virial estimator proposed by Herman et al. [105]

$$E_M^V = \frac{1}{M}\sum_{i=1}^{M}\left(\frac{1}{2}\mathbf{r}_i\frac{\partial V(\mathbf{r}_i)}{\partial \mathbf{r}_i} + V(\mathbf{r}_i)\right). \tag{2.30}$$

Both estimators depend on the number of timeslices M. It has been found that the accuracy of these estimators is strongly affected by the algorithm used [41, 80]. In both cases, the error grows linearly with $\sqrt{M}$ if only microscopic moves are allowed. As M is increased to ensure the convergence of the path integral to the exact result, the error of both estimators grows boundlessly [41].

Improving the kind of Monte Carlo steps that are allowed in order to assure a freer movement of the paths reduces the error of the virial estimator significantly. It has been shown by J. Cao and B. Berne that in this case it does not depend on M anymore [41]. Nevertheless, the fluctuation of the energy which has to be calculated after each Monte Carlo step is very dependent on the kind of move used.

In our simulations, a different approach is applied which overcomes the problems of the other energy estimators. It has been shown by H. Heinze et al. [101, 102] that in the canonical ensemble, it is possible to utilize the hypervirial theorem of Hirschfelder [108] and rewrite the kinetic and potential energies as expectation values of functions depending on two-particle distances only. For a system of identical particles with $|k\rangle$ denoting the N-particle eigenfunction and E_k the corresponding energy eigenvalue, they achieve

$$E_{\text{kin}} = \frac{1}{Z}\sum_k e^{-\beta E_k}\langle k|\,\frac{1}{2}\sum_{i<j} r_{ij}\frac{\partial V_2(r_{ij})}{\partial r}\,|k\rangle \tag{2.31}$$

and

$$E_{\text{pot}} = \frac{1}{Z}\sum_k e^{-\beta E_k}\langle k|\sum_{i<j} V_2(r_{ij})\,|k\rangle\,, \tag{2.32}$$

where $r_{ij} = |\mathbf{r}_i - \mathbf{r}_j|$ denotes the distance between particles i and j. Only two-particle interactions $V_2(r)$ are taken into account here. The pair correlation function for two particles is

$$\Gamma_{i,j}(r) = \langle \delta(r - r_{ij}) \rangle \tag{2.33}$$

and for identical particles, one can take all particle combinations into account to get the probability distribution of all possible two-particle distances r

$$\Gamma(r) = \frac{2}{N(N-1)} \left\langle \sum_{1 \le i < j \le N} \delta(r - r_{ij}) \right\rangle . \tag{2.34}$$

In this case, the energies can be rewritten as

$$E_{\text{kin}} = \frac{N(N-1)}{4} \int_0^\infty \mathrm{d}r\, \Gamma(r) r \frac{\partial V_2(r)}{\partial r} \tag{2.35}$$

and

$$E_{\text{pot}} = \frac{N(N-1)}{2} \int_0^\infty \mathrm{d}r\, \Gamma(r) V_2(r). \tag{2.36}$$

The one-particle parts of the energy are calculated using the radial electron densities per electron

$$\rho_i(r) = \frac{1}{2\pi r} \langle \delta(r - |\mathbf{r}_i|) \rangle = \frac{1}{2\pi r} \varrho(r). \tag{2.37}$$

Here we have

$$E_{\text{kin}} = \frac{N}{2} \int_0^\infty \mathrm{d}r\, \varrho(r) r \frac{\partial V_{\text{ext}}(r)}{\partial r} \tag{2.38}$$

and

$$E_{\text{pot}} = \frac{N}{2} \int_0^\infty \mathrm{d}r\, \varrho(r) V_{\text{ext}}(r). \tag{2.39}$$

for a system of identical particles in an external potential $V_{\text{ext}}(r)$.

In order to visualize the spatial structure of the electron configuration in the quantum rings as described in Chapter II-2, we introduce angular pair correlation functions

$$\Gamma_{i,j}(\varphi) = \langle \delta(\varphi - \varphi_{ij}) \rangle , \tag{2.40}$$

where φ_{ij} is $|\varphi_i - \varphi_j|$.

In the simulations described in this thesis, interacting electrons in an external potential V_{ext} are studied. Therefore, spin ↑ ($s_i = 1/2$) and spin ↓ ($s_i = -1/2$) electrons have to be handled separately and the corresponding pair correlation functions and radial densities are $\Gamma^{\uparrow\uparrow}$, $\Gamma^{\downarrow\downarrow}$, $\Gamma^{\uparrow\downarrow}$, $\rho^{\uparrow}$, and $\rho^{\downarrow}$. The numbers of electrons with positive and negative spin are given by $N^{\uparrow}$ and $N^{\downarrow}$.

The pair correlation functions and radial densities are stored in histograms and updated after each Monte Carlo step.

It is now possible to calculate the kinetic and potential energies as functions of the radial densities and pair correlation functions:

$$\begin{aligned}
E_{\mathrm{kin}} =& E^{\uparrow}_{\mathrm{kin}} + E^{\downarrow}_{\mathrm{kin}} + E^{\uparrow\uparrow}_{\mathrm{kin}} + E^{\downarrow\downarrow}_{\mathrm{kin}} + E^{\uparrow\downarrow}_{\mathrm{kin}} \\
=& \frac{N^{\uparrow}}{2} \int_0^{\infty} \mathrm{d}r\, \varrho^{\uparrow}(r) r \frac{\partial V_{\mathrm{ext}}(r)}{\partial r} + \frac{N^{\downarrow}}{2} \int_0^{\infty} \mathrm{d}r\, \varrho^{\downarrow}(r) r \frac{\partial V_{\mathrm{ext}}(r)}{\partial r} \\
&+ \frac{N^{\uparrow}(N^{\uparrow}-1)}{4} \int_0^{\infty} \mathrm{d}r\, \Gamma^{\uparrow\uparrow}(r)\, r\, \frac{\partial V_2(r)}{\partial r} \\
&+ \frac{N^{\downarrow}(N^{\downarrow}-1)}{4} \int_0^{\infty} \mathrm{d}r\, \Gamma^{\downarrow\downarrow}(r)\, r\, \frac{\partial V_2(r)}{\partial r} \\
&+ \frac{N^{\downarrow}N^{\uparrow}}{2} \int_0^{\infty} \mathrm{d}r\, \Gamma^{\uparrow\downarrow}(r)\, r\, \frac{\partial V_2(r)}{\partial r}
\end{aligned} \tag{2.41}$$

and

$$\begin{aligned}
E_{\mathrm{pot}} =& E^{\uparrow}_{\mathrm{pot}} + E^{\downarrow}_{\mathrm{pot}} + E^{\uparrow\uparrow}_{\mathrm{pot}} + E^{\downarrow\downarrow}_{\mathrm{pot}} + E^{\uparrow\downarrow}_{\mathrm{pot}} \\
=& \frac{N^{\uparrow}}{2} \int_0^{\infty} \mathrm{d}r\, \varrho^{\uparrow}(r) V_{\mathrm{ext}}(r) + \frac{N^{\downarrow}}{2} \int_0^{\infty} \mathrm{d}r\, \varrho^{\downarrow}(r) V_{\mathrm{ext}}(r) \\
&+ \frac{N^{\uparrow}(N^{\uparrow}-1)}{2} \int_0^{\infty} \mathrm{d}r\, \Gamma^{\uparrow\uparrow}(r) V_2(r) \\
&+ \frac{N^{\downarrow}(N^{\downarrow}-1)}{2} \int_0^{\infty} \mathrm{d}r\, \Gamma^{\downarrow\downarrow}(r) V_2(r) \\
&+ N^{\uparrow}N^{\downarrow} \int_0^{\infty} \mathrm{d}r\, \Gamma^{\uparrow\downarrow}(r) V_2(r).
\end{aligned} \tag{2.42}$$

This straightforward method of calculating the kinetic and exchange correlation energies is one of the advantages of the path integral Monte Carlo method as applied in this thesis. In contrast to the energy estimators of Barker and Herman, the energies depend only on the radial densities and pair correlation functions and not directly on M or the kind of Monte Carlo move used. The number of timeslices only influences the error due to the application of Trotter's formula. If M is chosen sufficiently large, the error of the radial densities and pair correlation functions is determined by the statistical error of the Monte Carlo simulation only. In this way, the error of the calculated energies can be pushed to small values if the number of Monte Carlo steps is large.

3 Convergence and computational effort

3.1 Optimizing simulation parameters

It is now detailed how the systematic and statistical errors of path integral Monte Carlo simulations can be minimized with an acceptable computational effort.

First of all, it is essential to exclude numerical problems such as correlations of the random numbers, or incorrect computation of the determinant. The steplengths of the different kinds of Monte Carlo moves must also be adjusted to sizes corresponding to a satisfactory acceptance rate of the Monte Carlo steps. If these conditions are fulfilled, the number of timeslices M and the number of Monte Carlo steps must be tuned.

As described in Section 2 of the last chapter, the thermodynamic path integral Eq. (2.16) is formally exact for an infinite number of timeslices M, i.e., the systematic error of a simulation is determined by the choice of M. The statistical error of the Monte Carlo simulation is proportional to the reciprocal value of the square root of the number of Monte Carlo steps. For an exact solution of the integral, the number of steps also must be infinite.

It can be demonstrated that comparably small numbers of timeslices limit the systematic error considerably. A few billion Monte Carlo moves are usually enough to push the statistical error of the simulation into an acceptable range [30].

In principle, using more timeslices is expected to yield results closer to exact results, but the necessary computer time increases since the motion of the paths slows as the value of M increases. This is because the number of microscopic Monte Carlo steps needed to move a full path is $\geq M$ and the corresponding steplength has to be decreased for larger M in order to achieve a satisfactory acceptance rate. If the number of timeslices chosen is too large, the problem might be unsolvable with today's computers because the statistical error of the Monte Carlo simulation scales down too slowly. On the other hand, decreasing M below a required minimum results in an unacceptable systematic error.

There is no known reliable algorithm to automate the investigation of the best feasible combination of timeslices and computer time to minimize the total error.

Therefore, convergence studies as presented in the following have to be carried out before long simulation runs to guarantee reliable results and the most effective use of computational power. Convergence studies are also important for verifying that the code is correct [44].

To demonstrate the reliability of our algorithm, comparisons between path integral Monte Carlo studies and exact recursive calculations of *non-interacting* electrons in a harmonic potential are presented. The confining potential is modeled by the quantum dot parameters (see Chapter II-1 for details), i.e. $\hbar\omega_0$ = 3 meV. The exact results were obtained by utilizing the recursion formula for the occupation number η_i of a state i as described in Chapter III-1,

$$\eta_i(N+1,\beta) = \frac{Z_N(\beta)}{Z_{N+1}(\beta)} \exp(-\beta\epsilon_i)(1-\eta_i(N,\beta)) \;, \tag{2.43}$$

with

$$\frac{Z_N(\beta)}{Z_{N+1}(\beta)} = \frac{N+1}{\sum_{i=0}^{\infty} \exp(-\beta\epsilon_i)(1-\eta_i(N,\beta))} \;. \tag{2.44}$$

The energy expectation value is given by

$$E_{\mathrm{EXACT}}(N,\beta) = \sum_{i=0}^{\infty} \epsilon_i \eta_i(N,\beta) \; . \tag{2.45}$$

For the path integral Monte Carlo simulations, it can be obtained as described in Section 2.3.

Convergence studies were carried out for N = 1, 2 and T = 10 K and the number of timeslices was varied from M = 10 to M = 100. Figure 2.3 shows the relative error of the energies versus the number of Monte Carlo steps for different values of M calculated using the path integral Monte Carlo algorithm. The relative error is given by

$$\Delta E = \frac{E_{\mathrm{PIMC}} - E_{\mathrm{EXACT}}}{E_{\mathrm{EXACT}}}. \tag{2.46}$$

For comparison, the exact energies are 3.189 meV for N = 1 and 9.197 meV for N = 2.

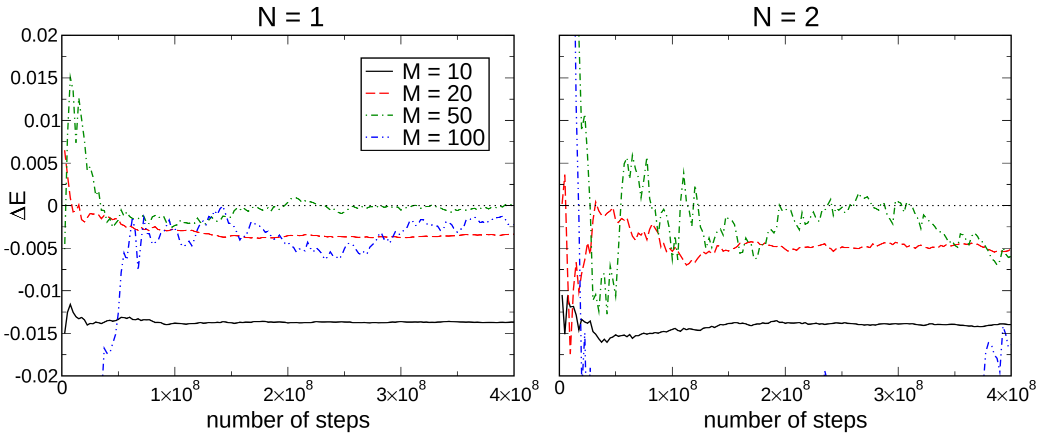

Figure 2.3: Relative errors of the energy for N = 1, 2, T = 10 K, M = 10, 20, 50, and 100 and up to $4{\cdot}10^8$ Monte Carlo steps.

As expected, the simulations for one electron converge faster than the simulations for two electrons. The relative errors of the simulations for M = 10 converge to about -0.014 after only a very limited number of Monte Carlo steps ($1{\cdot}10^8$ and $2{\cdot}10^8$). Increasing the number of timeslices results in a higher statistical error: The larger M is, the larger the variation of the relative error dependent upon the number of Monte Carlo steps becomes. For N = 1, the relative error converges to constant values for M = 20 and M = 50. In the M = 50 case, ΔE even approaches zero. The error obtained using M = 100 is still much smaller than for M = 10. In the N = 2 case, convergence is not achieved for M = 50 and M = 100. Increasing the particle number prohibits the convergence without increasing the number of Monte Carlo steps.

In summary, M = 10 is not sufficient to achieve accurate results and for larger particle numbers, it is impossible to achieve convergence for M = 100 with an affordable amount of computational power. The results for M = 20 converge fast, but are still limited by a significant systematic error.

Studies such as the ones presented in Fig. 2.3 give a rough estimate of the number of Monte Carlo steps and timeslices necessary for a given problem using the path integral Monte Carlo technique. Even if the exact value is not known, comparing single simulations with different parameters makes it possible to approximate the appropriate parameter range.

Next, more detailed simulations were performed to optimize the settings. For N = 2 and T = 10 K, Fig. 2.4a displays the results of path integral Monte Carlo simulations for a fixed number of $4{\cdot}10^8$ Monte Carlo steps. The number of timeslices was set to M = 10, 20, 30, 50, 70, and 100 and for each value of M, ten independent simulation runs were used to calculate the average energy E'_{PIMC}. Its standard deviation, σ, is visualized by the error bars, and the dotted line represents the exact value.

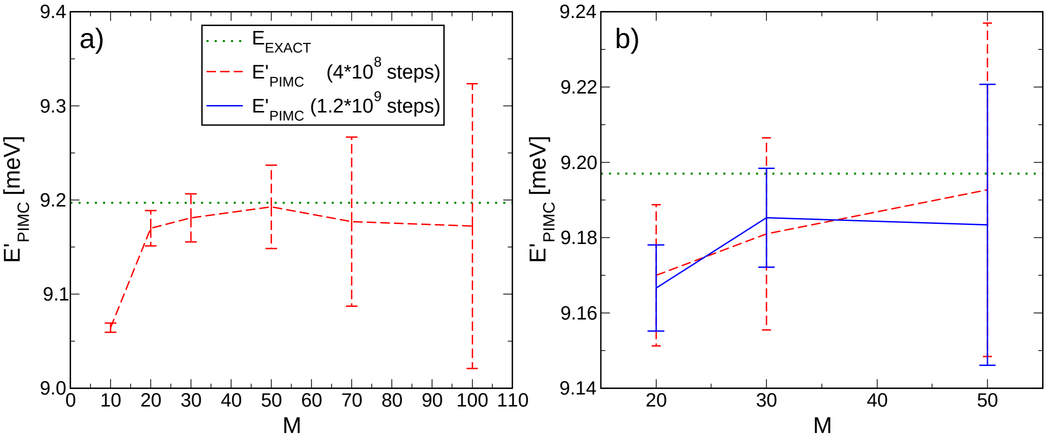

Figure 2.4: Exact and PIMC energy expectation values for N = 2, T = 10 K, M = 10, 20, 30, 50, 70, and 100 and $4{\cdot}10^8$ Monte Carlo steps (a). Figure b) is for comparison of the data presented in a) with values obtained from longer simulation runs ($1.2{\cdot}10^9$ steps) for M = 20, 30, and 50. Ten independent simulations were performed for each M to obtain the PIMC energies. The error bars are given by the standard deviation σ.

For M = 10, the statistical error is very small, but the average energy deviates by 0.13 meV from the exact result. Doubling the number of timeslices quadruples the size of the error bar, but the obtained energy only deviates by about 0.03 meV from the exact value. M = 30 produces the first value with the exact energy inside its error bars. The average energy for M = 50 deviates only by 0.005 meV or 0.05% from the exact result. From this point on, the difference between the average energies and the exact value increases with an increasing number of timeslices. The statistical error becomes large, i.e., $\sigma = \pm 1\%$ for M = 70 and $\sigma = \pm 1.6\%$ for M = 100.

Two empirical arguments support restricting the parameter range that has to be taken into account for a given number of Monte Carlo steps: (i) If there is no overlap between two error bars belonging to two neighboring values of M, the smaller M is not sufficient. (ii) If σ is larger than a given percentage of the average value, M is too large for the problem to be solved within the available computer time. Here, it is stipulated that σ must be smaller than ±1%. These arguments make it possible to restrict M to values between 20 and 50.

In order to find the best suitable number of timeslices, the statistical error of the simulations is reduced by increasing the number of Monte Carlo steps to $1.2{\cdot}10^9$. The resulting energies E'_{PIMC} are visualized in Fig. 2.4b for M = 20, 30, and 50. For comparison, the data obtained for $4{\cdot}10^8$ Monte Carlo steps is also presented in Fig. 2.4b (dashed line).

The standard deviation for M = 20 is very close to the one for M = 30 (±0.16% and ±0.14%, respectively). For M = 50, σ is significantly larger, at ±0.41%. Figure 2.4b illustrates that the overlap between the error bars for M = 20 and M = 30 is significantly smaller than in Fig. 2.4a, indicating that M = 20 might be not sufficient. The large σ of the M = 50 simulation is an argument for M = 30 being the best suitable number of timeslices.

In the special case presented here, where the exact energy expectation value is known, this result can be strengthened by introducing the value

$$\Delta E_{\mathrm{tot}} = \frac{|E'_{\mathrm{PIMC}} - E_{\mathrm{EXACT}}| + \sigma}{E_{\mathrm{EXACT}}} \tag{2.47}$$

to describe the total relative error of the simulation. Here, ΔE_{tot} is minimized for M = 30 (ΔE_{tot} = $2.7{\cdot}10^{-3}$) and the corresponding values for M = 20 and M = 50 are significantly larger ($4.6{\cdot}10^{-3}$ and $5.5{\cdot}10^{-3}$).

If the best suitable parameter combination still results in an unacceptable error, the number of Monte Carlo steps must be increased in order to minimize the statistical error. If this exceeds the available computing resources, the only possibility is to increase the simulation temperature in order to reduce the influence of the fermion-sign problem.

3.2 Organization of large scale simulations

The overall error of the energy expectation values was pushed far below one percent for simulations of quantum dots and quantum rings as presented in the next part of this thesis. For example, in the quantum ring case, as much as 10^{11} steps per simulation run were required. Without the complete parallelization of the code, these simulations would not have been possible. Even on a Cray T3E with 62 processors, the most CPU-intensive simulations needed up to two days of computation time.

The program was parallelized using the MPI library[2], which allows parallel computation on multi-processor machines as well as on clustered single-processor systems over the network.

Most of the simulations were performed on a Cray T3E at the 'Konrad Zuse Institut Berlin' using 62 processors and another Cray T3E with 16 processors at the 'Regionales Rechenzentrum Niedersachsen'. For the simulations of quantum dot molecules, a Linux cluster with 32 processors was employed for most of the work. Up to 20 machines with different Unix based operating systems have been used simultaneously. These were mostly single processor systems of our group and the university computer center.

---

[2] http://www-unix.mcs.anl.gov/mpi/

No algorithms were applied to improve the performance of the calculation of the path integral or to avoid the fermion sign problem. The only optimizations are a good random number generator and the consistent use of optimized subroutines. In this way, the ’brute force’ algorithm is able to produce very precise results. Different algorithms have been published to improve the performance of path integral calculations. For example, the ’multilevel blocking’ method by Mak et al. [153] partially avoids the fermion sign problem and is expected to converge better. However, it is shown in Chapter II-1 that the results of Egger et al. [58] do not confirm this expectation. The advantages of their new approach are probably more than compensated by other numerical problems.

The usually limited time per job and the amount of data motivated the use of the NetCDF library known from meteorological data analysis[3]. This library makes it possible to develop a platform-independent method of storing the data of a simulation in just one file. Additionally, a restart function has been included, making it possible to finish jobs that have been started on one machine on any other one, thus utilizing the available processor time as efficiently as possible.

To optimize the use of the available computing power, a job queuing and status inquiry system was developed. This system povides the possibility to generate initial data files, to transfer these files to the computing machines, to submit the jobs, and have the results returned to the local server automatically. It consists of a set of shell scripts and Fortran programs and utilizes a locally installed NQS[4] server to enable an efficient queuing for machines in the network that do not have their own queuing mechanisms installed.

---

[3] http://www.unidata.ucar.edu/packages/netcdf/

[4] http://www.gnqs.org/

II

Application of the path integral Monte Carlo technique on selected systems

1

Interplay between shell effects and electron correlations in quantum dots

J. Harting, O. Mülken, and P. Borrmann

Physical Review B 62, 10207 (2000)

PHYSICAL REVIEW B VOLUME 62, NUMBER 15 15 OCTOBER 2000-I

Interplay between shell effects and electron correlations in quantum dots

Jens Harting, Oliver Mülken, and Peter Borrmann
Department of Physics, Carl von Ossietzky University Oldenburg, D-26111 Oldenburg, Germany

(Received 18 February 2000)

We use the path integral Monte Carlo method to investigate the interplay between shell effects and electron correlations in single quantum dots with up to 12 electrons. By use of an energy estimator based on the hypervirial theorem of Hirschfelder we study the energy contributions of different interaction terms in detail. We discuss under which conditions the total spin of the electrons is given by Hund's rule, and the temperature dependence of the crystallization effects.

I. INTRODUCTION

The advances in nanofabrication of the last years opened the goal to build two-dimensional (2D) quantum dots (QD's) and quantum dot molecules (QDM's)— artificial mesoscopic semiconductor structures of selectable shape and size—as *containers* for a controllable fixed number of electrons.[1,2] Recently, depending on the strength and shape of the effective confining potential, the formation of spin density waves (SDW's) (Refs. 3 and 4) and Wigner crystals[3,5] in QD's and QDM's has been predicted by different groups with different theoretical approaches. Hirose and Wingreen[6] argue that SDW's are reproducible artifacts of spin density functional calculations. For a 2D parabolic confining potential the accordance of the spin configuration with Hund's rule has been predicted by Koskinen, Manninen, and Reimann[4] and questioned by Yannouleas and Landman.[3] All these effects are governed by the intriguing interplay between shell effects, the pure Coulomb repulsion, and the fermionic repulsion due to the Pauli exclusion principle and depend strongly on the values of the interaction parameters in the commonly assumed Hamiltonian for single QD's

$$H=\sum_{i=1}^{N}\left(\frac{\mathbf{p}_i^2}{2m^*}+\frac{m^*\omega_0^2}{2}\mathbf{x}_i^2\right)+\sum_{i<j=1}^{N}\frac{e^2}{\kappa|\mathbf{x}_i-\mathbf{x}_j|}, \qquad (1)$$

where κ is the dielectric constant, m^* is the effective mass, and ω_0 defines the strength of the confining potential.

Apart from the interesting physical questions that arise for quantum dots the reliable prediction of their properties is an ultimate test of modern methods in quantum chemistry. Due to the compared to atoms very shallow confining potential, long range electron interactions and correlations play an important role in QD's and QDM's. Therefore it is misleading to name them artificial atoms and molecules. Well established and very elaborate methods of quantum chemistry might fail in describing them properly. Hartree-Fock and spin density functional methods use single Slater determinants or sums of them to approximate the many-body wave function. In spin-density functional methods the approximation of the functional for the exchange correlation energy[4,7,8] adds another source of uncertainty and systematic errors to this approach. The path integral Monte Carlo method (PIMC) used in this paper samples the full many-body wave function instead.

In contrast to density functional methods (DFT) with PIMC it is possible to study the temperature dependent properties of QD's. The reason why PIMC is not yet a standard method of quantum chemistry is its numerical limitation due to the fermion sign problem. The rapidly increasing power of modern computers resizes this limitation. In Sec. II we briefly summarize our implementation of PIMC and comment on how to limit the numerical deficiencies due to the fermion sign problem.

We apply PIMC to calculate the electron density and two-particle correlation functions for quantum dots with up to 12 electrons. To compare with various experimental studies as well as with other theoretical studies we use different dielectric constants κ and strengths of the confining parabolic potentials. The calculated addition energies are in very good agreement with the experimental findings of Tarucha *et al.*[2]

For $N=6$ we investigate the temperature dependence of the Wigner crystallization (WC).

II. NUMERICAL METHOD

For a system of N electrons with position eigenket $|\vec{x}_i, s_i\rangle$ ($s_i=\pm\frac{1}{2}$ for spin-up and spin-down electrons) in an external potential the Feynman path integral can be written as[9–11]

$$Z=\int\left[\prod_{\gamma=1}^{M}\prod_{i=1}^{N}d\vec{x}_i(\gamma)\right]\prod_{\delta=1}^{M}\det[A(\delta,\delta+1)]\times\exp\left(-\frac{\beta}{M}\sum_{\alpha=1}^{M}V[\vec{x}_1(\alpha),\ldots,\vec{x}_N(\alpha)]\right)+O\left(\frac{\beta^3}{M^2}\right), \qquad (2)$$

with

$$[A(\alpha,\alpha+1)]_{i,j}=\begin{cases}\left\langle\vec{x}_i(\alpha)\left|\exp\left(-\frac{\beta}{M}\frac{\mathbf{p}^2}{2m}\right)\right|\vec{x}_j(\alpha+1)\right\rangle, & s_i=s_j\\ 0, & s_j\neq s_j\end{cases} \qquad (3)$$

and the boundary condition $\vec{x}_j(M+1)=\vec{x}_j(1)$. M is the number of so-called *timeslices* of the Feynman paths. In the limit $M\to\infty$ Eq. (2) becomes exact. For quantum dots the space dimension is $d=2$ and the $(2NM)$-dimensional integral given in Eq. (2) can be evaluated by standard Metropolis

0163-1829/2000/62(15)/10207(5)/$15.00 ©2000 The American Physical Society

Monte Carlo techniques. Due to the determinant the integrand is not always positive and the expectation value of an observable $X(\mathbf{x})$ depending only on position operators has to be calculated using

$$\langle X\rangle=\frac{\sum_{g=1}^{G} X_g\,\mathrm{sgn}(W_g)}{\sum_{g=1}^{G}\mathrm{sgn}(W_g)},\tag{4}$$

where X_g is the value of the observable X and W_g is the value of the integrand in Eq. (2) in the gth Monte Carlo step. Equation (4) reveals a severe problem connected with the path integral for fermions which is commonly denoted as the *fermion sign problem* (see, e.g., Refs. 12–14). It can be shown that the ratio between integrands with positive sign (W^{+}) and negative sign (W^{-}) is approximately given by[14,15]

$$\frac{W^{+}-W^{-}}{W^{+}+W^{-}}\sim\exp[-\beta(E_F-E_B)],\tag{5}$$

where E_F and E_B are the ground state energies of the Fermi system and the corresponding Bose system. It is now obvious that the statistical error in Eq. (4) grows rapidly for small temperatures T. Moreover the energy difference (E_F-E_B) will grow with increasing system size causing an increase of the statistical error.

Within PIMC the calculation of the kinetic energy expectation value is another critical task. This is merely due to the fact that the Monte Carlo calculation is usually done in position space and that the discretization of the paths allows a number of different approaches to calculate the expectation value of a momentum dependent operator. A number of various different energy estimators has been discussed in the past.[16–18]

To avoid these difficulties we developed a procedure which allows the calculation of all energy expectation values from the knowledge of the pair correlation functions

$$\Gamma_{i,j}(r)=\langle\delta(r-|\vec{x}_i-\vec{x}_j|)\rangle\tag{6}$$

and the radial density functions per electron

$$\rho_i(r)=\frac{1}{2\pi r}\langle\delta(r-|\vec{x}_i|)\rangle=\frac{1}{2\pi r}\varrho(r),\tag{7}$$

where ϱ is the probability of finding electron i in distance r from the center.

Due to the particle symmetry we have

$$\Gamma_{i,j}(r)=\begin{cases}\Gamma^{\uparrow\uparrow}(r), & s_i=s_j=+\dfrac{1}{2}\\[2ex] \Gamma^{\downarrow\downarrow}(r), & s_i=s_j=-\dfrac{1}{2}\\[2ex] \Gamma^{\uparrow\downarrow}(r), & s_i\neq s_j\end{cases}\tag{8}$$

and

$$\rho_i(r)=\begin{cases}\rho^{\uparrow}(r), & s_i=+\dfrac{1}{2}\\[2ex] \rho^{\downarrow}(r), & s_i=-\dfrac{1}{2}.\end{cases}\tag{9}$$

Utilizing the hypervirial theorem of Hirschfelder[19] the energy can be written as a sum of ten parts[20]

$$\begin{aligned}E={}&E_{\mathrm{kin}}^{\uparrow}+E_{\mathrm{kin}}^{\downarrow}+E_{\mathrm{kin}}^{\uparrow\uparrow}+E_{\mathrm{kin}}^{\downarrow\downarrow}+E_{\mathrm{kin}}^{\uparrow\downarrow}+E_{\mathrm{pot}}^{\uparrow}+E_{\mathrm{pot}}^{\downarrow}+E_{\mathrm{pot}}^{\uparrow\uparrow}+E_{\mathrm{pot}}^{\downarrow\downarrow}+E_{\mathrm{pot}}^{\uparrow\downarrow}=\frac{N^{\uparrow}}{2}\int_0^{\infty}dr\,\varrho^{\uparrow}(r)r\partial_r V_1(r)+\frac{N^{\downarrow}}{2}\int_0^{\infty}dr\,\varrho^{\downarrow}(r)r\partial_r V_1(r)\\&+\frac{N^{\uparrow}(N^{\uparrow}-1)}{4}\int_0^{\infty}dr\,\Gamma^{\uparrow\uparrow}(r)\,r\frac{\partial V_2(r)}{\partial r}+\frac{N^{\downarrow}(N^{\downarrow}-1)}{4}\int_0^{\infty}dr\,\Gamma^{\downarrow\downarrow}(r)\,r\frac{\partial V_2(r)}{\partial r}+\frac{N^{\downarrow}N^{\uparrow}}{2}\int_0^{\infty}dr\,\Gamma^{\uparrow\downarrow}(r)\,r\frac{\partial V_2(r)}{\partial r}\\&+\frac{N^{\uparrow}}{2}\int_0^{\infty}dr\,\varrho^{\uparrow}(r)V_1(r)+\frac{N^{\downarrow}}{2}\int_0^{\infty}dr\,\varrho^{\downarrow}(r)V_1(r)+\frac{N^{\uparrow}(N^{\uparrow}-1)}{2}\int dr\,\Gamma^{\uparrow\uparrow}(r)V_2(r)\\&+\frac{N^{\downarrow}(N^{\downarrow}-1)}{2}\int dr\,\Gamma^{\downarrow\downarrow}(r)V_2(r)+N^{\uparrow}N^{\downarrow}\int dr\,\Gamma^{\uparrow\downarrow}(r)V_2(r).\end{aligned}\tag{10}$$

While in density functional approaches the calculation of the kinetic energy and the exchange correlation energy is a major topic and subject to permanent discussion, within the path integral approach these energies are included in a natural way.

However, the systematic error arising from the limited number of timeslices M and the statistical error of the Monte Carlo calculation have to be controlled carefully. We checked our algorithm extensively using eight noninteracting fermions in a parabolic trap as a test system. We found that at low temperatures where the ratio of signs is around 0.99, convergence can only be achieved obeying the following rules: (1) The determinants have to be calculated very accurately using a more costly algorithm with pivoting. (2) The completely uncorrelated generation of the Monte Carlo steps is essential, i.e., the coordinate to be moved should be chosen randomly. Moving the particle coordinates using always the same sequence produces inaccurate results. (3) A good random number generator with a *completely* uncorrelated sequence in all significant bits of a 64 bit real number should be applied. We therefore developed a 53 bit random number of Marsaglia-Zaman type[21] instead of using one of the standard 24 or 32 bit random number generators coming with standard system libraries. (4) Further, to improve the conver-

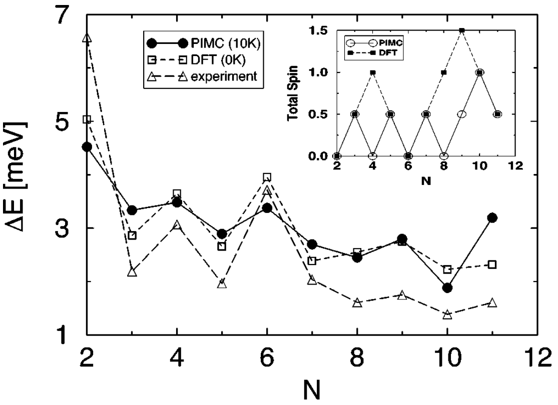

FIG. 1. Addition energies for quantum dots with up to 11 electrons. The circles indicate the results from our path integral calculations at 10 K, the squares are results of spin density functional calculations of Hirose and Wingreen, and the triangles are the experimental results of Tarucha *et al.* The error bars for PIMC would be of the size of the solid circles and are therefore omitted.

gence a number of different Monte Carlo steps can be applied, i.e., moving single time slices, moving complete particle paths and parts of a path. Our Fortran code is completely parallelized using MPI and Lapack.

III. RESULTS

To compare our PIMC calculations to experimental data we calculated the addition energies

$$\Delta E = E_{N+1} - 2E_N + E_{N-1} \tag{11}$$

of a QD with up to 11 electrons using the material constants $m^* = 0.067m$ and $\kappa = 12.9$ for GaAs as given by Hirose and Wingreen.[6] It is assumed that these parameters mimic the experimental setup of Tarucha *et al.*[2] reasonably well. The strength of the harmonic potential is fixed at $\hbar\omega_0 = 3.0$ meV. The resulting effective atomic units are $E_H^* = 10.955$ meV for the Hartree energy and $a_0^* = 10.1886$ nm for the Bohr radius. The Boltzmann constant is $k_B = 7.8661 \times 10^{-3}\, E_H^*/\mathrm{K}$.

We performed PIMC simulations for quantum dots with different spin configurations at a fixed temperature of 10 K. Due to the fermion sign problem the number of Monte Carlo steps necessary to push the statistical error of the total energy, which has been calculated properly from 25 uncorrelated subsequences of MC steps, into the range of 0.1% is extremely high. The number of Monte Carlo steps ranged between 2.5 billion steps per particle coordinate for $N \leqslant 6$ and about 10 billion steps for $N = 12$. Figure 1 displays the addition energies for quantum dots with up to 11 electrons. The circles indicate the results from our path integral calculations at 10 K, the squares are results of spin density functional calculations of Hirose and Wingreen,[6] and the triangles are the experimental results of Tarucha *et al.*[2] Both theoretical calculations reproduce the general N dependence of the addition energies in great detail. Tarucha *et al.* give an estimate of the electron temperature in their experiments of $T = 0.2$ K. For computational reasons our PIMC calculations are performed at 10 K and it cannot be expected that the absolute energy values agree as well as the 0 K DFT calculations with the experimental results. However, it should be noted that PIMC correctly predicts the drop in the addition energy from $N = 7$ to $N = 8$ while the DFT calculations fail at this point.

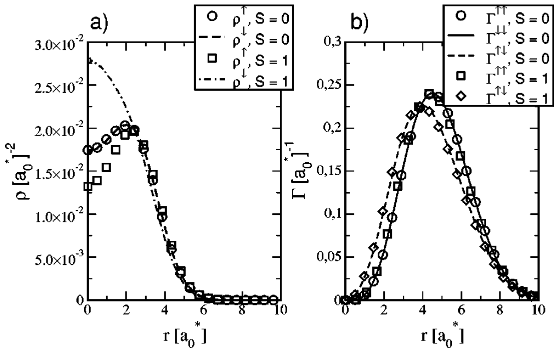

FIG. 2. (a) Radial density per electron and (b) pair correlation functions for four electrons and total spins $S = 0$ and $S = 1$. The material constants are $\kappa = 12.9$ and $\hbar\omega = 3.0$ meV.

The inset in Fig. 1 displays the total spins of the spin configurations with lowest energy as found in DFT and PIMC at 10 K. In DFT calculations (0 K) the spin configuration of the ground state is determined by Hund's rule for up to 22 electrons. In contrast, in our PIMC calculation at 10 K the total spin is not always in accordance with Hund's rule. For $N = 4$ we checked the temperature dependence of the spin configuration. At 5 K the energy of the spin 0 configuration is 0.01 E_H^* higher than the spin 1 energy indicating a temperature dependence of the favored spin configuration.

As an important fact we note that the N dependence of the addition energies is not affected by the actual spin configuration. The situation is quite similar to that in transition metal clusters with extreme small energy differences between states with significantly different magnetic moments.[22]

As can be inferred from Fig. 2(a) the radial spin densities are significantly different for both spin configurations. The total potential energy for the spin 1 configuration is about 0.07 meV lower than that of the spin 0 configuration. At 10 K this is overcompensated by an 0.27 meV higher kinetic energy (see Table I). Although the kinetic and potential energies for different total spins significantly differ, the total energies are almost equal. Similar situations are found for larger N.

For convenience and easy comparison we determined the value of the dimensionless density parameter r_s, which is sometimes used to characterize quantum dots (see, e.g., Ref. 5) to be $r_s = 4.19$ for $N = 4$.

The energies given in Table I correspond to the integrals in Eq. (10). The total kinetic energy which is the sum of all E_{kin}^x terms is always positive while some of the addends might be negative. Table I reveals that larger total spins result in larger kinetic energies. The total potential energy is almost unchanged, the larger contribution from the trap potential is compensated by a smaller contribution from the Coulomb repulsion. We note that the ratio E_{W} between the kinetic energy and the total energy is considerably larger for $N = 4$ than for $N = 9$ reflecting the looser binding of the smaller system.

TABLE I. Kinetic and potential energies as well as $E_W = E_{kin}/E_{tot}$ in meV for different electron configurations at 10 K (the numbers in parentheses are the single particle energies).

	$N^{\uparrow}=2,\ N^{\downarrow}=2$	$N^{\uparrow}=3,\ N^{\downarrow}=1$	$N^{\uparrow}=5,\ N^{\downarrow}=4$	$N^{\uparrow}=6,\ N^{\downarrow}=3$
E_{tot}	40.83	41.03	169.25	169.82
E_{kin}	7.33	7.60	18.97	19.57
E_{pot}	33.50	33.43	150.28	150.26
E_W	0.18	0.19	0.11	0.12
$E_{kin}^{\uparrow}$	8.03 (8.03)	12.66 (8.44)	35.44 (14.18)	43.74 (14.58)
$E_{kin}^{\downarrow}$	8.03 (8.03)	3.55 (7.10)	27.30 (13.65)	19.39 (12.93)
$E_{kin}^{\uparrow\uparrow}$	-1.31 (-2.62)	-3.97 (-2.65)	-11.20 (-2.24)	-16.87 (-2.25)
$E_{kin}^{\uparrow\downarrow}$	-6.11 (-3.05)	-4.64 (-3.09)	-25.84 (-2.58)	-23.31 (-2.59)
$E_{kin}^{\downarrow\downarrow}$	-1.31 (-2.62)	0.00 (0.00)	-6.72 (-2.24)	-3.39 (-2.26)
E_{pot}	33.50	33.43	150.28	150.26
$E_{pot}^{\uparrow}$	8.03 (4.01)	12.66 (4.22)	35.44 (7.09)	43.74 (7.30)
$E_{pot}^{\downarrow}$	8.03 (4.01)	3.55 (3.55)	27.30 (6.82)	19.39 (6.46)
$E_{pot}^{\uparrow\uparrow}$	2.62 (2.62)	7.94 (2.65)	22.40 (2.24)	33.73 (2.25)
$E_{pot}^{\uparrow\downarrow}$	12.21 (3.05)	9.28 (3.09)	51.69 (2.58)	46.62 (2.59)
$E_{pot}^{\downarrow\downarrow}$	2.62 (2.62)	0.00 (0.00)	13.44 (2.24)	6.78 (2.26)

Next we consider the dependence of the Wigner crystallization on the temperature and the choice of the material constants. The localization of the electrons in space is commonly referred to as Wigner crystallization. For quantum dots the occurrence of well separated humps in the radial electron density and the pair correlation functions has been interpreted as WC. However, it is a nontrivial task to find a general parameter identifying if an electron system is crystallized or not. From a solid state physics point of view the electrons should have a low mobility, i.e., a small kinetic energy, and should not interchange their lattice positions. For fermions the localization of single electrons does not make any sense, and, as stated above, even the decomposition of the many-body wave function in sums of determinants of single particle wave functions is probably a too rough approximation for QD's. These facts limit the analogies between crystallization in solids and electron systems and make the term *crystallization* itself somehow misleading. We therefore view Wigner crystals as states of the many-body wave function with a relatively low kinetic energy.

First we consider the strength of the Wigner crystallization depending on the choice of the interaction parameters. Figure 3 displays the radial densities and pair correlation functions for six electrons with $S=0$, $\hbar\omega=5$ meV, and $\kappa=3.0$, 6.0, and 12.9. Of course, for stronger electron repulsions (small κ) the electron distributions are broadened. The qualitative picture of the distributions is merely the same. For all κ shell effects indicated by off-center maximums of the radial density occur. However, only for $\kappa=3$ and 6 we observe a maximum at $r=0$. From our point of view it cannot definitely be decided from this figure if a system is Wigner crystallized or not. As a parameter reflecting the strength of the WC we employ the ratios between the kinetic and the total energies $E_W = E_{kin}/E_{tot}$ which are 0.07, 0.10, and 0.14 for $\kappa=3.0$, 6.0, and 12.9. Although the radial distribution function for $\kappa=12.9$ is quite narrow, the relative mobility for the electrons indicated by E_W is twice as large as for $\kappa=3$. The underlying physical process can be understood intuitively. Due to the stronger electron-electron repulsions the electrons are fixed in an energetical favorable geometric configuration and as a consequence thereof the relative kinetic energy is reduced and the difference between the pair correlation functions of equal and opposite spin almost vanishes (see Fig. 3). It is an interesting and to our knowledge open question, if the crystallization of electrons can be viewed as a phase transition. We therefore consider next the temperature dependent properties of a quantum dot with $N=6$, $S=0$, $\kappa=3$, and $\hbar\omega=5$ meV. The results for temperatures between 10 and 150 K are presented in Table II. Most notably E_W increases relatively smoothly from 0.07 at 10 K to 0.22 at 150 K. Within our numerical accuracy the caloric curve does not show any evidence of a phase transition. The transition from a crystallized state to an electron *fluid* seems to be squashy. Of course, from our calculations we cannot exclude that a phase transition exists for larger N

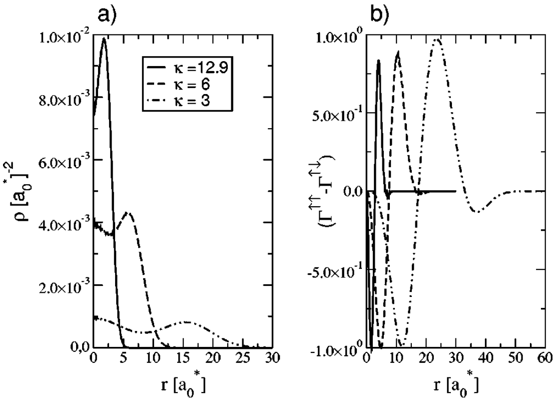

FIG. 3. Radial density per electron (left) and pair correlation functions (right) for $N=6$, $S=0$, $\hbar\omega_0=5$ meV and dielectric constants $\kappa=3.0$, 6.0, and 12.9 at 10 K. The radial density for $\kappa=12.9$ is scaled by a factor of 3 and the pair correlation functions are scaled to have a maximum value of ±1.

TABLE II. Kinetic and potential energies for different temperatures and spin configuration $N^{\uparrow}=3$, $N^{\downarrow}=3$. The Hartree energy is $E_H^*=202.558$ meV, $\kappa=3$, and $\hbar\omega_0=5.0$ meV. E_W is the ratio between the kinetic and the total energy.

$N^{\uparrow}=3$, $N^{\downarrow}=3$	E_W	E_kin (meV)	E_pot (meV)	E_tot (meV)
$T=10$ K	0.07	17.70	246.53	264.32
$T=30$ K	0.08	22.93	249.53	272.46
$T=60$ K	0.12	35.39	257.67	293.06
$T=90$ K	0.16	49.44	267.01	316.46
$T=120$ K	0.19	64.10	276.84	340.93
$T=150$ K	0.22	78.49	286.88	365.35

or different interaction parameters. Figure 4 displays the radial electron densities and the total electron pair correlation function for different temperatures. Up to 60 K the radial density shows clear geometric structure effects with two maximums while at 150 K only a smooth curve resembling a simple Gaussian remains.

IV. CONCLUSION

In conclusion, we have found that despite of the notorious fermion sign problem PIMC is capable of answering interesting questions for strongly correlated electron systems like QD's and QDM's. For QD's PIMC reproduces correctly the experimental addition energies. Our temperature dependent calculations give new insights into the process of WC. For the two-dimensional QD's a ratio $E_\mathrm{W}=E_\mathrm{kin}/E_\mathrm{tot}$ below 0.1 seems to indicate WC both for κ and temperature dependent calculations. However, regarding this aspect a more firm classification parameter, e.g., similar to the Lindemann criterion is desirable.

A comparision to other QMC methods seems to be in order here. Even our most complicated simulations took less than 2 h on a Cray T3E with 62 processors. Taking the advantages of modern computer power and optimized software, the *brute force* PIMC applied here is able to produce very precise results. Different algorithms have been published to improve the performance of path integral methods. A recent one is the *multilevel blocking* method published by Mak *et al.*[23] Simulations using this algorithm are expected to converge better than our direct treatment since the fermion sign problem is avoided partially. The published results of the treatment of quantum dots by Egger *et al.*[5] do not confirm this expectation. Obviously the advantages of the new method are more than compensated by other numerical problems, maybe due to the energy estimator used.[24] Nevertheless, a combination of the multilevel-blocking method and our technique might result in a very powerful tool.

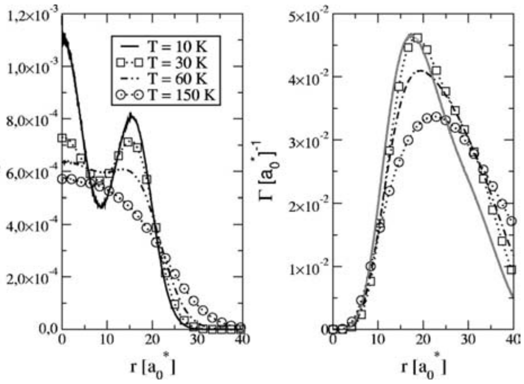

FIG. 4. Radial density (left) and pair correlation functions (right) for $N=6$, $S=0$, $\hbar\omega_0=5$ meV, $\kappa=3.0$, and temperatures $T=10$, 30, 60, and 150 K.

ACKNOWLEDGMENTS

We wish to thank the *Regionales Rechenzentrum Niedersachsen* and the *Konrad Zuse Institut Berlin* for their excellent computer support and E. R. Hilf for stimulating discussions.

---

[1] N. Zhitenev, R. Ashoori, L. Pfeiffer, and K. West, Phys. Rev. Lett. **79**, 2308 (1997).

[2] S. Tarucha, D. Austing, and T. Honda, Phys. Rev. Lett. **77**, 3613 (1996).

[3] C. Yannouleas and U. Landman, Phys. Rev. Lett. **82**, 5325 (1999).

[4] M. Koskinen, M. Manninen, and S. Reimann, Phys. Rev. Lett. **79**, 1389 (1997).

[5] R. Egger, W. Häusler, C. Mak, and H. Grabert, Phys. Rev. Lett. **82**, 3320 (1999).

[6] K. Hirose and N. Wingreen, Phys. Rev. B **59**, 4604 (1999).

[7] D. Pfannkuche, V. Gudmundsson, and P. Maksym, Phys. Rev. B **47**, 2244 (1993).

[8] R. Pino, Phys. Rev. B **58**, 4644 (1998).

[9] M. Takahashi and M. Imada, J. Phys. Soc. Jpn. **53**, 936 (1984).

[10] M. Takahashi and M. Imada, J. Phys. Soc. Jpn. **53**, 3765 (1984).

[11] P. Borrmann and E. Hilf, Z. Phys. D: At., Mol. Clusters **26**, S350 (1993).

[12] D. Ceperley, Phys. Rev. Lett. **69**, 331 (1992).

[13] A. Lyubartsev and P. Vorontsov-Velayaminov, Phys. Rev. A **48**, 4075 (1993).

[14] I. Morgenstern, Z. Phys. B: Condens. Matter **77**, 267 (1989).

[15] W.H. Newman and A. Kuki, J. Chem. Phys. **96**, 356 (1992).

[16] J. Cao and B. Berne, J. Chem. Phys. **91**, 6359 (1989).

[17] A. Giansanti and G. Jacucci, J. Chem. Phys. **89**, 7454 (1988).

[18] H. Kono, A. Takasaka, and S. Lin, J. Chem. Phys. **88**, 6390 (1988).

[19] J.O. Hirschfelder, J. Chem. Phys. **33**, 1462 (1960).

[20] H. Heinze, P. Borrmann, H. Stamerjohanns, and E. Hilf, Z. Phys. D: At., Mol. Clusters **40**, 190 (1997).

[21] P. Borrmann (unpublished).

[22] K. Lee and J. Callaway, Phys. Rev. B **48**, 15 358 (1993).

[23] C. Mak, R. Egger, and H. Weber-Gottschick, Phys. Rev. Lett. **81**, 4533 (1998).

[24] D. Ceperley, Phys. Rev. Lett. **69**, 331 (1992).

2

Order-disorder transition in nanoscopic semiconductor quantum rings

P. Borrmann and J. Harting

Physical Review Letters 86, 3120 (2001)

Order-Disorder Transition in Nanoscopic Semiconductor Quantum Rings

Peter Borrmann and Jens Harting
Department of Physics, Carl von Ossietzky University, D-26111 Oldenburg, Germany

(Received 31 August 2000)

Using the path integral Monte Carlo technique we show that semiconductor quantum rings with up to six electrons exhibit a temperature, ring diameter, and particle number dependent transition between spin ordered and disordered Wigner crystals. Because of the small number of particles the transition extends over a broad temperature range and is clearly identifiable from the electron pair correlation functions.

DOI: 10.1103/PhysRevLett.86.3120 PACS numbers: 73.23.–b, 31.15.Kb, 71.45.Lr, 73.21.–b

Nanoscopic semiconductor quantum rings (QRs), which recently have been experimentally realized by Lorke *et al.* [1], are next to quantum wires probably the best prototypes of quasi-one-dimensional quantum systems. QRs can be viewed as rotating Wigner crystals with promising features for application in microelectronics. They can be modeled using a simple Hamiltonian of the form

$$H = \sum_{i=1}^{n}\left(\frac{\mathbf{p}_i^2}{2m^*} + \frac{1}{2}m^*\omega_0^2(r_0 - r_i)^2\right) + \sum_{i<j}\frac{e^2}{\kappa r_{ij}}, \qquad (1)$$

where $\kappa = 12.9$ and $m^* = 0.067m_e$ are the material constants of GaAs [2,3]. The parameter r_0 is the radius of the quantum ring and ω_0 defines the strength of the two-dimensional potential [1,4]. Figure 1(a) displays the shape of the ring potential. QRs can be tuned from quasi-one-dimensional to two-dimensional systems by variation of the ring diameter and the potential strength.

While mesoscopic QRs have been investigated theoretically and experimentally in depth [5], nanoscopic rings with strong quantum effects are of increasing interest. Koskinen *et al.* [6] reported configuration-interaction calculations of rotational and vibrational excitations of nanoscopic QRs with up to $N = 7$ electrons. They claim that QRs behave like rather rigid molecules or Wigner crystals with antiferromagnetic order in the ground state. Ahn *et al.* [7] considered stacked nanoscopic rings and found an N-dependent Stark effect. Experimentally it has been found that the emission energies of QRs change abruptly whenever adding an electron [8].

In this Letter we present the results of path integral Monte Carlo (PIMC) simulations of single nanoscopic QRs with up to eight electrons and different radii r_0. We show that they undergo a temperature, radius, and particle number dependent spin order-disorder transition. Furthermore, the influence of quantum effects on the spatial electron distribution as well as the addition energies ΔE are given. Our results for the addition energies, i.e., the energy that is needed to place an additional electron in a ring, is compared to the experimental results of Warburton *et al.* [8].

In contrast to Hartree-Fock and spin density functional theory PIMC samples without any approximation the full many body wave function instead of single or sums of Slater determinants. Especially for highly correlated electron systems this is a major advantage of PIMC. Another benefit of PIMC is the possibility to study temperature dependent phenomena. For quantum dots the problems of different density functional approaches have intensively been discussed in the past [2,9–11]. The so-called fermion sign problem is still a topic of actual research and restricts the application of PIMC to a limited number of fermions and for QRs to a temperature of at least 10 K.

The Feynman path integral for an N-electron system with position eigenket $|\mathbf{r}_i, s_i\rangle$ ($s_i = \pm\frac{1}{2}$ for spin-up and spin-down electrons) in an external potential can be rewritten as [12]

$$Z = \int\left[\prod_{\gamma=1}^{M}\prod_{i=1}^{N} d\mathbf{r}_i(\gamma)\right]\prod_{\delta=1}^{M}\det\left(A(\delta,\delta+1)\right)\exp\left(-\frac{\beta}{M}\sum_{\alpha=1}^{M}V(\mathbf{r}_1(\alpha),\ldots,\mathbf{r}_N(\alpha))\right) + \mathcal{O}\left(\frac{\beta^3}{M^2}\right) \qquad (2)$$

with

$$(A(\alpha,\alpha+1))_{i,j} = \begin{cases}\langle\mathbf{r}_i(\alpha)|\exp(-\frac{\beta}{M}\frac{\mathbf{p}^2}{2m})|\mathbf{r}_j(\alpha+1)\rangle & : \quad s_i = s_j\,, \\ 0 & : \quad s_j \neq s_j\,, \end{cases} \qquad (3)$$

and the boundary condition $\mathbf{r}_j(M+1) = \mathbf{r}_j(1)$. For $M \to \infty$ Eq. (2) becomes exact. Standard Metropolis Monte Carlo (MC) techniques can be utilized to evaluate the integral in (2).

The basic quantities reflecting the spatial structure of the electron configuration are the electron-electron (distance) pair correlation functions $\Gamma_{i,j}(r) = \langle\delta(r - |\mathbf{r}_{ij}|)\rangle$, the angular pair correlation functions $\Gamma_{i,j}(\varphi) = \langle\delta(\varphi - |\varphi_i - \varphi_j|)\rangle$, and the radial electron density $\rho_i(r) = \frac{1}{2\pi r}\langle\delta(r - |\mathbf{r}_i|)\rangle$, from which all energies can be calculated using the hypervirial

0031-9007/01/86(14)/3120(4)$15.00 © 2001 The American Physical Society

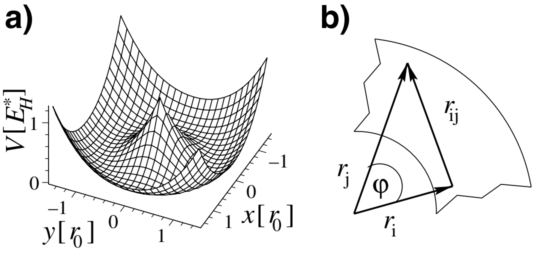

FIG. 1. Potential energy surface of a semiconductor quantum ring (a) and schematic illustration of the definition of φ (b).

theorem (for details of our method see [10]). The definitions of φ and $\mathbf{r}_{ij}$ are illustrated in Fig. 1(b). To take the particle symmetry into account we introduce $\Gamma_{ij} = \Gamma^{\uparrow\downarrow}$ for $s_i \neq s_j$, $\Gamma_{ij} = \Gamma^{\uparrow\uparrow}$ for $s_i = s_j = \frac{1}{2}$, and $\Gamma_{ij} = \Gamma^{\downarrow\downarrow}$ for $s_i = s_j = -\frac{1}{2}$, respectively. Obviously for $S = 0$ we have $\Gamma^{\downarrow\downarrow} = \Gamma^{\uparrow\uparrow}$.

In our simulations we controlled the systematic error arising from the limited number of time slices M and the statistical MC error carefully. By choosing $M \times T \simeq 600$ and using up to 10×10^{10} MC steps per run we pushed the overall error of all energy expectation values below 0.3%. Our FORTRAN code is completely parallelized using MPI and Lapack, and most calculations have been performed on a Cray T3E with 64 processors.

We fixed the strength of the harmonic potential $\hbar\omega_0 = 12$ meV, resulting in effective atomic units for the Hartree energy $E_H^* = 10.995$ meV and the Bohr radius $a_0^* = 10.1886$ nm. A ring diameter $r_0 = 14$ nm $= 1.37 a_0^*$ then corresponds to the experimental setup of Lorke *et al.* [1]. To investigate the ring size dependence we performed additional calculations for $r_0 = 50.94$ nm $= 5a_0^*$.

Figures 2(b) and 2(c) display the pair correlation functions of QRs with $N = 6$, $S = 0$, and ring diameters $r_0 = 1.37a_0^*$ and $5.0a_0^*$ at $T = 15$ K. As expected for both diameters peaks at $\varphi \approx \pi/3$ and $\varphi \approx 2\pi/3$ occur in $\Gamma(\varphi)$. For $r_0 = 5a_0^*$ the angular pair correlation functions for electrons with equal and unequal spin are almost identical; i.e., the Pauli principle does not play an important role in this case. In contrast, for $r_0 = 1.37a_0^*$ the pair correlation functions show a strong spin dependence. The electrons arrange on the ring with antiferromagnetic order. Such spin density waves have been predicted by Koskinen *et al.* [6,11]. The role of quantum effects is reflected as well in Fig. 2(a). For the smaller ring size the radial electron density is much broader and nonvanishing at the ring center, implying that the system does not behave like a quasi-1D system. In a perfect hexagonal Wigner crystal the equilibrium distances of the electrons would be $r = 1$, 1.73, and $2.0r_0$. For $r_0 = 5.0a_0^*$ the distance pair correlation function is approximately a properly weighted superposition of Gaussians centered at these distances. For $r_0 = 1.37a_0^*$ the pair correlation function depends on the total spin of a pair and is broadened up to $4r_0$. From Figs. 2(b) and 2(c) we infer that the most probable configuration is one where the electrons are ordered on a zigzag line around the circle; i.e., the electrons arrange alternately in the inner and the outer parts of the ring.

Figure 3 displays the angular spin density pair correlation functions for both ring diameters, temperatures $T = 15$, 30, and 90 K, and particle numbers $N = 4$ and 6. In all cases the large angle correlations disappear with increasing temperature and at $T = 90$ K only at small angles a spin correlation is still visible. For $r_0 = 5.0a_0^*$ the negative correlation at small angles increases with increasing temperature. However, this is simply due to the fact that the values of both correlation functions at small angles become larger with increasing temperature. The spin correlations for the small ring are about 1 order of magnitude larger than those in the ring with radius $r_0 = 5.0a_0^*$ (note the different scalings of the abscissas). A comparison between $N = 4$ and $N = 6$ shows that the spin correlation is smaller for the larger system. A probable reason for this is that for $N = 6$ the contribution of the Coulomb repulsion is much larger (see Table I) freezing the electron in the Wigner crystal and—thinking in the picture of one-particle wave functions—making the overlap between one-particle wave functions smaller.

In summary, from Fig. 3 it can be inferred that a spin order-disorder transition appears with increasing temperature, increasing electron number, and increasing ring size.

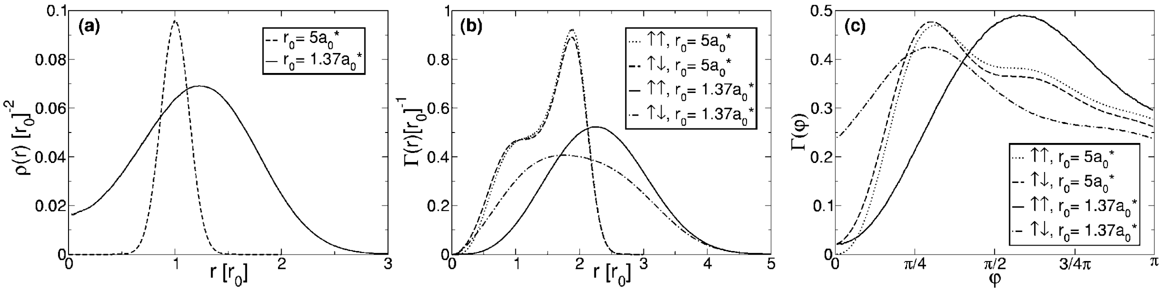

FIG. 2. Radial electron density (a), radial (b), and angular (c) pair correlation functions for $N = 6$, $S = 0$, and $r_0 = 1.37a_0^*$ and $5a_0^*$ at $T = 15$ K.

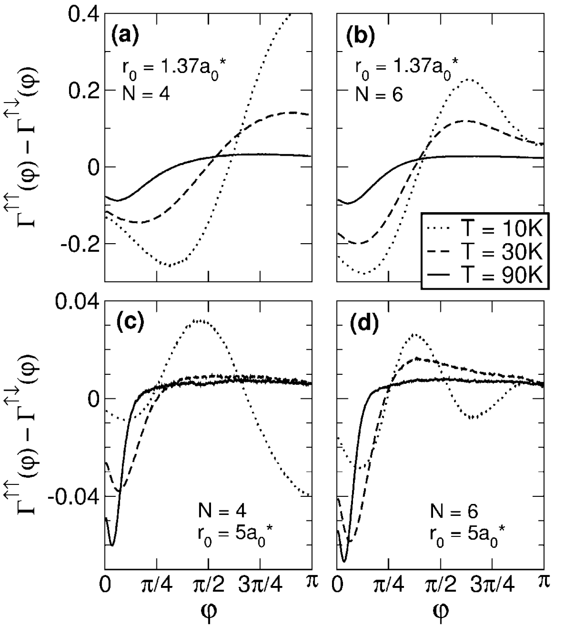

FIG. 3. Angular spin density correlation function $[\Gamma^{\uparrow\uparrow}(\varphi) - \Gamma^{\uparrow\downarrow}(\varphi)]$ for $T = 10$, 30, and 90 K and (a) $N = 4$, $S = 0$, and $r_0 = 1.37a_0^*$, (b) $N = 6$, $S = 0$, and $r_0 = 1.37a_0^*$, (c) $N = 4$, $S = 0$, and $r_0 = 5a_0^*$, and (d) $N = 6$, $S = 0$, and $r_0 = 5a_0^*$.

Next we consider the temperature dependence of the spin order-disorder transition in some more detail. Figure 4 displays the mean values of the angular separation of the electrons with equal and unequal spin for $N = 4$ and 6, $S = 0$, and $r_0 = 1.37a_0^*$ as a function of temperature. As expected from the results presented above, the overall differences between the expectation values for equal and unequal spins approach zero with increasing temperature; i.e., the Pauli principle becomes less important. In addition, the values for $N = 6$ are smaller than those for $N = 4$. Obviously, this is because the available portion per particle of the ring volume is smaller for a larger number of electrons and the Coulomb repulsion is unable to disperse the particles. At $T = 10$ K and $N = 4$ the contribution of the Coulomb term to the total potential energy is 53% for $r_0 = 1.37a_0^*$ and only 36% for $r_0 = 5a_0^*$, while for $N = 6$ the difference between the different diameters is with 60% and 51% substantially smaller (see Table I).

TABLE I. Total, kinetic, potential, ring, and Coulomb energies for $N = 4$ and 6, $S = 0$, $r_0 = 1.37a_0^*$ and $5a_0^*$ for different temperatures. All energies are given in meV.

N	$r_0(a_0^*)$	T (K)	$E_{\rm tot}$	$E_{\rm kin}$	$E_{\rm pot}$	$E_{\rm ring}$	$E_{\rm c}$
4	1.37	10	57.2	23.0	34.2	16.1	18.1
		25	59.3	24.4	35.0	16.8	18.2
		90	85.1	40.6	44.4	26.5	17.9
	5	10	32.7	15.0	17.7	11.4	6.3
		25	36.1	17.7	18.4	11.6	6.8
		90	62.0	35.4	26.6	18.5	8.1
6	1.37	10	117.8	39.4	78.4	31.1	47.3
		25	122.5	42.6	79.9	32.9	46.9
		90	160.9	66.7	94.2	48.4	45.8
	5	10	61.0	25.3	35.7	17.3	18.3
		25	65.7	28.8	36.9	17.8	19.1
		90	105.8	55.3	50.6	29.1	21.5

The slope of $\langle\varphi^{\uparrow\downarrow}\rangle$ for $N = 4$ can be understood as follows. Up to 40 K $\langle\varphi^{\uparrow\downarrow}\rangle$ increases due to spin disordering. At higher temperatures $\langle\varphi^{\uparrow\downarrow}\rangle$ decreases due to increasing thermal fluctuations.

Finally, we calculated the second energy differences $\Delta E = E_{N+1} - 2E_N + E_{N-1}$, also called addition energies, which are an indicator of the stability of a quantum ring with a given number of electrons. For quantum dots it was claimed that the electron configurations are given by Hunds rule [11] and consequently magic numbers occur at $N = 2$, 6, 12, and 20. Here we calculated only the addition energy up to $N = 7$ for 25 K and $N = 5$ for 10 K. As expected due to the Pauli principle and the Wigner crystal structure, a strong odd even effect occurs. The general behavior of this effect does not change for 25 K. However, for higher temperatures significant differences can be expected (see above). Warburton *et al.* [8] argued that the general features of shell effects occurring in QRs are the same as in quantum dots. As can be inferred from Fig. 5, our calculations confirm this for $N = 6$. Furthermore, the addition energies are in the same range as those from photoluminescence measurements at 4 K [8]. Because of the strong Coulomb repulsion in QRs, which grows with increasing electron number, it can be expected that shell effects become less important with increasing particle number.

The effects described above are reflected quantitatively in Table I presenting the total energy ($E_{\rm tot}$), kinetic energy ($E_{\rm kin}$), total potential energy ($E_{\rm pot}$), the energy due to the ring potential ($E_{\rm ring}$), and the Coulomb energy (E_c).

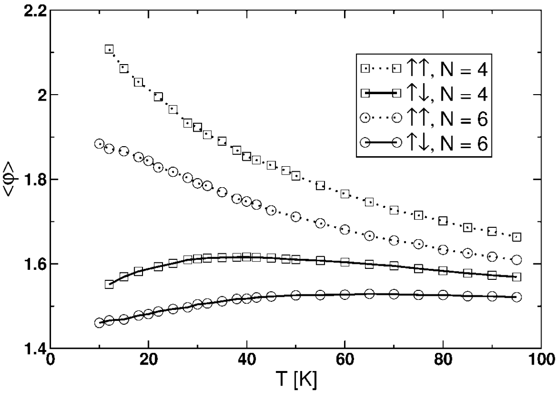

FIG. 4. Temperature dependence of the mean angles $\langle\phi^{\uparrow\uparrow}\rangle$ and $\langle\phi^{\uparrow\downarrow}\rangle$ for $N = 4$ and 6, $S = 0$, and $r_0 = 1.37a_0^*$.

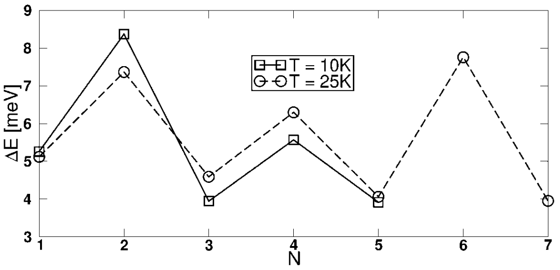

FIG. 5. Addition energies ΔE at temperatures $T = 10$ and 25 K for $r_0 = 1.37 a_0^*$.

In conclusion, we presented the results of full many body wave function calculations for QRs with up to eight electrons. We found that the properties of the rings depend in an intriguing manner on the ring diameter, the particle number, and the temperature, which in turn is due to spin correlation, Coulomb ordering, and the general strength of quantum effects. QRs exhibit a parameter dependent spin order-disorder transition. By variation of the ring diameter the system can be tuned from a quasi-1D Wigner crystal to a 2D structure. The accessible parameter ranges can be used to tune the properties of quantum rings to desired values. Because of the ring diameter as an additional parameter, this qualifies them as even better candidates than quantum dots for possible applications in microelectronics. The addition energies calculated using PIMC are in good agreement with the experimental results of Warburton *et al.* [8] and reflect the predicted shell effects.

We thank the *Konrad Zuse Institut Berlin* and the *Regionales Rechenzentrum Niedersachsen* for their excellent computer support and Oliver Mülken, Heinrich Stamerjohanns, and E. R. Hilf for fruitful discussions.

[1] A. Lorke, R. Luyken, A. Govorov, J. Kotthaus, J. Garcia, and P. Petroff, Phys. Rev. Lett. **84**, 2223 (2000).
[2] K. Hirose and N. Wingreen, Phys. Rev. B **59**, 4604 (1999).
[3] The value of $\kappa = 12.9$ for GaAs is slightly different from the experiments of Lorke *et al.,* which has the more appropriate value of $\kappa = 14.5$ for InAs. We have chosen this value for easier comparison to previous quantum dot calculations.
[4] T. Chakraborty and P. Pietiläinen, Phys. Rev. B **50**, 8460 (1994).
[5] L. Wendler and V. Fomin, Phys. Status Solidi B **191**, 409 (1995); L. Wendler, V. Fomin, A. Chaplik, and A. Govorov, Phys. Rev. B **54**, 4794 (1996); D. Mailly, C. Chapelier, and A. Benoit, Phys. Rev. Lett. **70**, 2020 (1993).
[6] M. Koskinen, M. Manninen, B. Mottelson, and S. Reimann, cond-mat/0004095, 2000.
[7] K. Ahn and P. Fulde, Phys. Rev. B **62**, 4813 (2000).
[8] R. Warburton, C. Schäflein, D. Haft, F. Bickel, A. Lorke, K. Karrai, J. Garcia, W. Schoenfeld, and P. Petroff, Nature (London) **405**, 926 (2000).
[9] C. Yannouleas and U. Landman, Phys. Rev. Lett. **82**, 5325 (1999).
[10] J. Harting, O. Mülken, and P. Borrmann, Phys. Rev. B **62**, 10 207 (2000).
[11] M. Koskinen, M. Manninen, and S. Reimann, Phys. Rev. Lett. **79**, 1389 (1997).
[12] M. Takahashi and M. Imada, J. Phys. Soc. Jpn. **53**, 936 (1984); M. Takahashi and M. Imada, J. Phys. Soc. Jpn. **53**, 3765 (1984); P. Borrmann and E. Hilf, Z. Phys. D **26**, S350 (1993).

3 Multi-functional nano-sized electronic components

1 Introduction

The advances in the fabrication of small semiconductor structures in recent years making the fabrication of quantum dots and quantum dot molecules of nanoscopic size possible have already been described in previous chapters. As a result, the application of these very precisely tunable devices in microelectronics becomes most interesting.

In order to develop high-performance electronic devices for applications in computers and modern information technology, the number of transistors per chip has to be increased and the power consumption reduced. The limits of conventional techniques using silicon and lithographic processes are well known and the application of new techniques and materials becomes essential. One possible approach is to reduce the number of electrons needed in single transistors or complex integrated circuits. Transistors using only a single electron were already developed more than ten years ago [109, 119]. Recently, different AFM-based methods including AFM lithography [149], mechanical scratching [197], or current-controlled local oxidation [122] have become popular for fabricating semiconductor single electron transistors.

Quantum dot molecules were studied in detail shortly after the fabrication of the first quantum dots and have been a topic of interest ever since [14, 99, 129, 173, 174, 196, 212]. In this chapter, new methods of implementing nanoscopic electronic switching devices or logical functions using coupled quantum dots are presented.

Many groups working on quantum computation are trying to implement ’qubits’ using quantum dots [111, 148]. The quantum computational ’qubits’ correspond to the transistors in conventional computers [63, 200]. In contrast to the classical implementations, they cannot only be in the states ’ON’ and ’OFF’, or ’1’ and ’0’, but also in a coherent superposition of the two states. The approach presented here is more classical: A distinction is made between two states only. A system is stated as ’ON’ if the probability of finding an electron at a given position is higher than a minimum probability p_{on} and ’OFF’ if the probability of finding an electron is lower than the corresponding probability p_{off}.

2 The double quantum dot

The first approach described in this chapter utilizes a quantum dot molecule consisting of two GaAs quantum dots with different physical properties.

The effective potential is modeled as illustrated in Fig. 3.1 using two-dimensional harmonic oscillators of strength ω_i, i = 1, 2. Their minima are equally shifted from the origin by a distance x_0 and one oscillator has a potential energy offset of V_0. Experimentally, different oscillator strengths correspond to differently sized dots. A change of V_0 can be achieved with an additional electrode producing a well-localized electrical field.

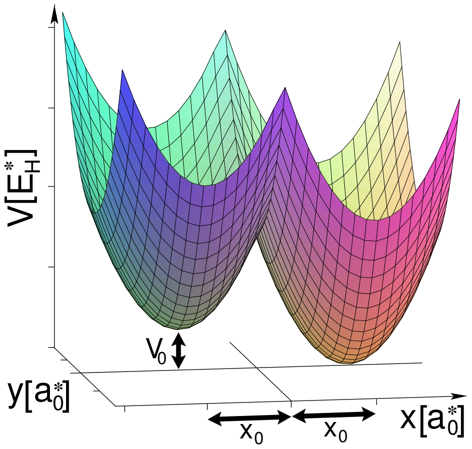

Figure 3.1: Potential energy surface of a semiconductor quantum dot molecule consisting of two quantum dots.

The effective potential is modeled by

$$V(\mathbf{r}) = \begin{cases} \frac{m^*}{2}\omega_1^2\left((x+x_0)^2+y^2\right)+V_0 & : \quad x \leq x_{\text{cut}} \\ \frac{m^*}{2}\omega_2^2\left((x-x_0)^2+y^2\right) & : \quad x > x_{\text{cut}} \end{cases},$$

where $\mathbf{r} = (x, y)$ is the coordinate of the given electron. In order to minimize the discontinuity at the intersection of both oscillators, both parts are not merged at the origin but instead a value x_{cut} is introduced. This point represents the x value at which both potential parts are equal and y = 0. For ω_1 = ω_2, it is given by

$$x_{\text{cut}} = -\frac{V_0}{2m^*\omega_1^2 x_0} \tag{3.1}$$

and for different potential strengths by

$$x_{\text{cut}} = \frac{x_0}{\omega_2^2-\omega_1^2}\left(\omega_1^2+\omega_2^2-\sqrt{4\omega_1^2\omega_2^2-2V_0\frac{\omega_1^2-\omega_2^2}{m^*x_0^2}}\right). \tag{3.2}$$

With the material constants κ = 12.9 and m^* = 0.067 m_e for GaAs [106], the resulting Hamiltonian is

$$H = \sum_{i=1}^{n}\left(\frac{\mathbf{p}_i^2}{2m^*}+V(\mathbf{r}_i)\right)+\sum_{i<j}\frac{e^2}{\kappa|\mathbf{r}_i-\mathbf{r}_j|}. \tag{3.3}$$

The strength of the harmonic potentials is fixed at $\hbar\omega_i$ = 12 meV, resulting in effective atomic units for the Hartree energy E^*_H = 10.995 meV and the Bohr radius a^*_0 = 10.1886 nm.

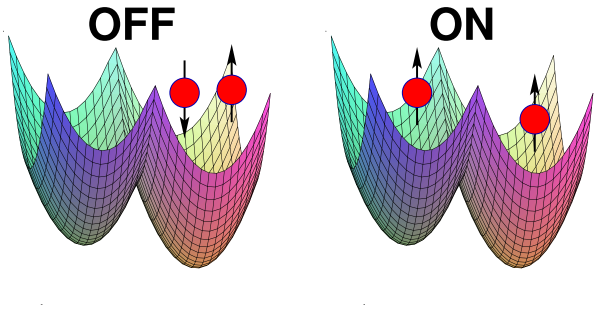

Figure 3.2: Schematic view of a double quantum dot including two electrons. If the electrons have unequal spins, the Pauli principle does allow both of them to stay in the same dot. If one parallelizes the spins, one electron has to move to the dot with the higher ground state. This state is denoted as 'ON'.

Only two electrons are needed to achieve precisely distinguishable states of the system. The 'switching' is based on Pauli's principle as shown in Fig. 3.2. The electrons are permitted to stay in the same dot only if they do not have the same spin. The corresponding harmonic potential of this dot has a lower ground state than the potential of the other dot. If the spins are parallelized, for example, by an external magnetic field, one electron has to move into the second dot. The parameters of the potentials of the dots, i.e., ω_i, x_0 and V_0, have to be chosen carefully in order to provide clearly distinguishable ground states. It is important that the ground state of the dot to which one electron is to be moved to is higher than the other dot's ground state. Additionally, it is necessary to ensure that it is lower than the first excited state of the first dot.

In this way, this device could be used as a transistor if the spins are flipped by external fields. A single photon detector can be obtained if a single photon can flip one electron's spin to push the electron into the dot with the higher ground state energy. Since the relaxation time is short, the readout has to be done very quickly.

Using the path integral Monte Carlo technique, studies of the double dot system depending on the temperature and potential parameters were performed. In the previous chapters, it has been sufficient to use one-dimensional histograms in our simulations. Due to the rotational symmetry of the single quantum dots and quantum rings, all relevant properties have been obtained from the radial density $\rho(r)$ and the pair correlation functions $\Gamma(r)$, $\Gamma(\varphi)$. The broken symmetry of quantum dot molecules suggests two-dimensional histograms to mimic the electron density. In this way, the structure of the electron distribution can be visualized easily. It is also possible to calculate the electron density in a given area by summing up the corresponding histogram entries. The sum of all histogram cells, i.e., the total electron density, is normalized to the number of electrons N.

Figure 3.3 illustrates the electron distribution in the device in two ways: The upper half shows the electron density in the x-y-plane. Below, the density is plotted for $y = 0$, i.e., only the histogram cells at $y = 0$ are taken into account. The left side corresponds to two electrons with different spins, i.e., total spin $S = 0$, and the right side corresponds to two electrons with equal spins ($S = \pm 1$). Since in our case, $S = 1$ and $S = -1$ can be treated similarly, the simulations presented here are restricted to $S = 1$. The temperature of the system is 20 K, x_0 is 2 a_0^*, and the left dot potential has an offset of V_0 = 1.1 E_H^*.

With this parameter set, the new device works well because the total electron density in the left dot varies by a factor of about four between both spin scenarios. For S = 0 it is 0.22 and for S = 1 it is 0.84. The 'OFF' and 'ON' states are clearly distinguishable.

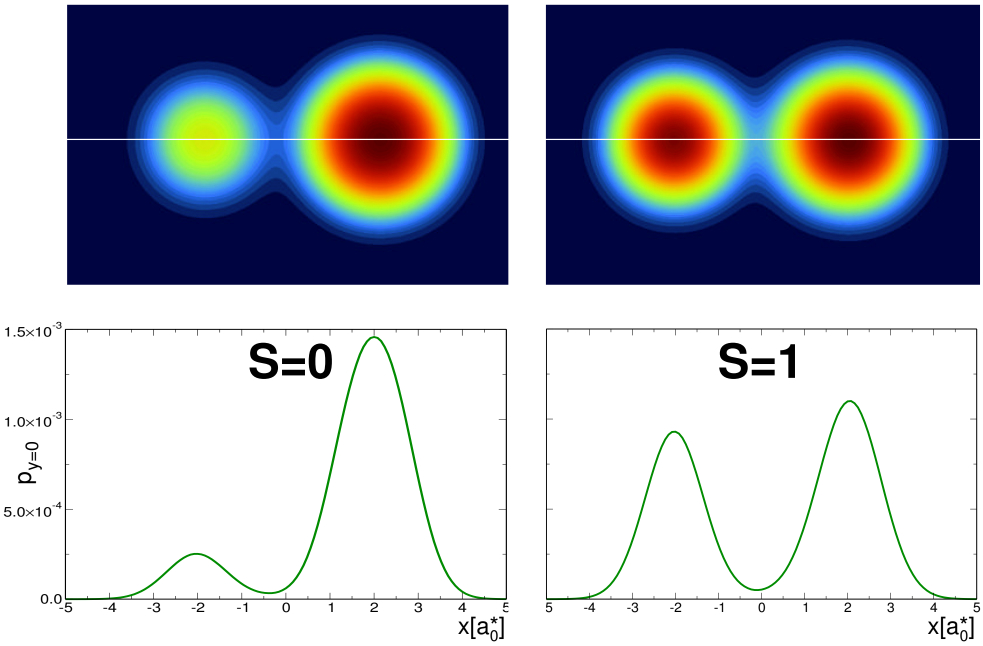

Figure 3.3: A double quantum dot with two electrons and total spin S = 0 (left) and S = 1 (right). S = 0 corresponds to the state 'OFF' and S = 1 to the state 'ON'. The upper half shows a density plot of the two-dimensional histograms and below them, the histograms for y = 0 are plotted. The total electron density in the left dot is 0.22 for S = 0 and 0.84 for S = 1.

If the temperature is increased, the probability of finding one of the electrons in an excited state increases as well. Therefore, the difference of the electron distributions for the two spin states becomes smaller. This effect is presented in Fig. 3.4 and Fig. 3.5. Figure 3.4 shows the electron density at y = 0 for both spin states and T = 20, 50, 100, and 150 K. For T = 20 K, the peaks corresponding to both dots are sharp and clearly distinguishable in both spin cases. Increasing the temperature results in broader distributions in the S = 1 case. In the S = 0 case, the device behaves similarly in the lower energetic dot. For the left dot, the height of the peak does not always increase with increasing temperature. While it is small and sharp for 20 K, for 50 K it is even higher than for all other temperatures and decreases for T = 100 K and 150 K again. This demonstrates the mobility of the electrons: At 50 K, the energy is high enough to occupy the left dot, but since only the ground state or low excited states are occupied, the electron stays in the center of the dot. At higher temperatures, excited states of both dots can be occupied, resulting in a broadened electron distribution.

To study the possibility of using a quantum dot molecule as an implementation of a nanoscopic switching device, it is more useful to plot the total electron density of a complete dot. Figure 3.5 shows the total electron density in the left dot p_l for the

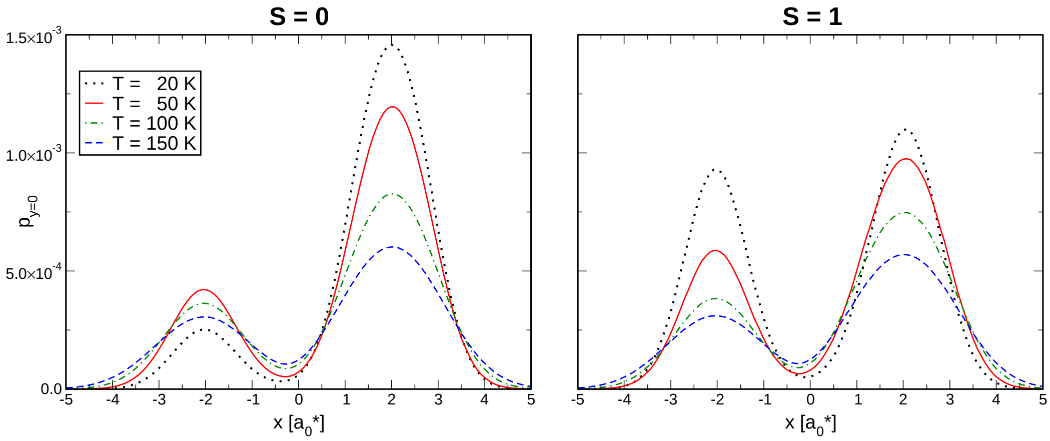

Figure 3.4: Electron densities at y = 0 for two electrons in a double quantum dot at different temperatures and different total spins.

same parameters as above. The difference between the two graphs becomes smaller for higher temperatures and nearly vanishes at T = 150 K. This is in accordance with the corresponding graphs in Fig. 3.4, where the electron distributions of both spin states at T = 150 K are no longer distinguishable.

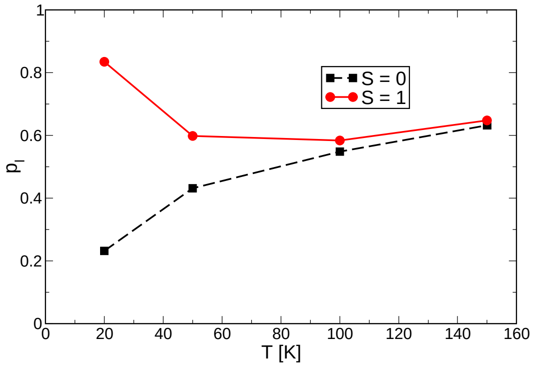

Figure 3.5: Total electron density in the left dot for S = 0 and S = 1.

Simulations with different sets of parameters V_0, x_0 and ω_i were performed. It was found that a double quantum dot can also be used as a switch if the harmonic oscillator strengths or the inter-dot distances are varied instead of V_0. Nevertheless, the interplay of the different parameters has a strong influence on the difference between the electron distributions in the S = 0 and the S = 1 states. If, for example, the harmonic oscillator strengths are increased, i.e., smaller dots are used, the displacement of the center of the dots from the origin x_0 has to be decreased. Otherwise, the barrier between both dots at x_{cut} can be too high to allow an electron to move from one dot to another.

Although it has been demonstrated that the double quantum dot device works well, it has two major disadvantages for applications in microelectronics: The temperature of the system has to be very low, which rules out any implementation in consumer products because the needed cooling mechanisms are usually only available in the laboratory. The second disadvantage is that the spins of the electrons have to be in a well-defined state for measurable lengths of time.

3 Logical functions at high temperatures

In the following, a system is presented that overcomes the problems of the double quantum dot. Furthermore, it is not only applicable as a nanoscopic transistor, but can also be used to implement logical functions. ’AND’ and ’OR’ operations can be performed using the same device.

The device consists of three aligned quantum dots, where the outer ones are equally sized and the inner one is smaller. Additionally, the properties of the inner dot can be adjusted by an energy offset V_0. Figure 3.6 presents the potential energy surface which is modeled in the style of the double dot and given by

$$V(\mathbf{r}) = \begin{cases} \frac{m^*}{2}\omega_1^2\left((x+x_0)^2+y^2\right) & : \quad x \leq -x_{\text{cut}} \\ \frac{m^*}{2}\omega_2^2\left(x^2+y^2\right)+V_0 & : \quad -x_{\text{cut}} < x < +x_{\text{cut}} \\ \frac{m^*}{2}\omega_1^2\left((x-x_0)^2+y^2\right) & : \quad x \geq +x_{\text{cut}} \end{cases} .$$

The device works as follows: The outer dots are filled with a given number of electrons to define the state of the system. These electrons can enter the left or the right dot through external gate electrodes. In this way, a system with two input channels or two ’bits’ is obtained. For the readout, only the inner dot is utilized. If the electron density inside the inner dot exceeds a given value, the system is defined as being in state ’1’. Otherwise, it is in state ’0’.

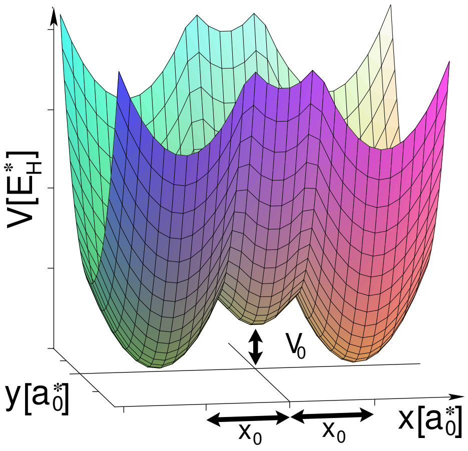

Figure 3.6: Potential energy surface of a semiconductor quantum dot molecule consisting of three quantum dots.

An ’AND’ function can be implemented by filling the outer dots with up to one electron each. For the readout, an additional electron is inserted. If initially only one outer dot is filled, the readout-electron will be located in the other one as a result of the

Coulomb repulsion. The resulting signal in the centered dot is small. If none of the dots is initially filled, the signal is, of course, even smaller. Only if both dots are filled will the readout electron cause the electron density in the centered dot to exceed the minimum value, which means the system is now in state ’1’.

This device is easily transformed into an ’OR’ function by pre-filling an arbitrary outer dot with one electron. In this case, one additional electron is sufficient to achieve an electron density high enough to be stated as ’1’ in the inner dot.

In summary, it is sufficient for the system to be in the state ’1’ if at least three electrons are inside. Figure 3.7 visualizes the principle of both implementations.

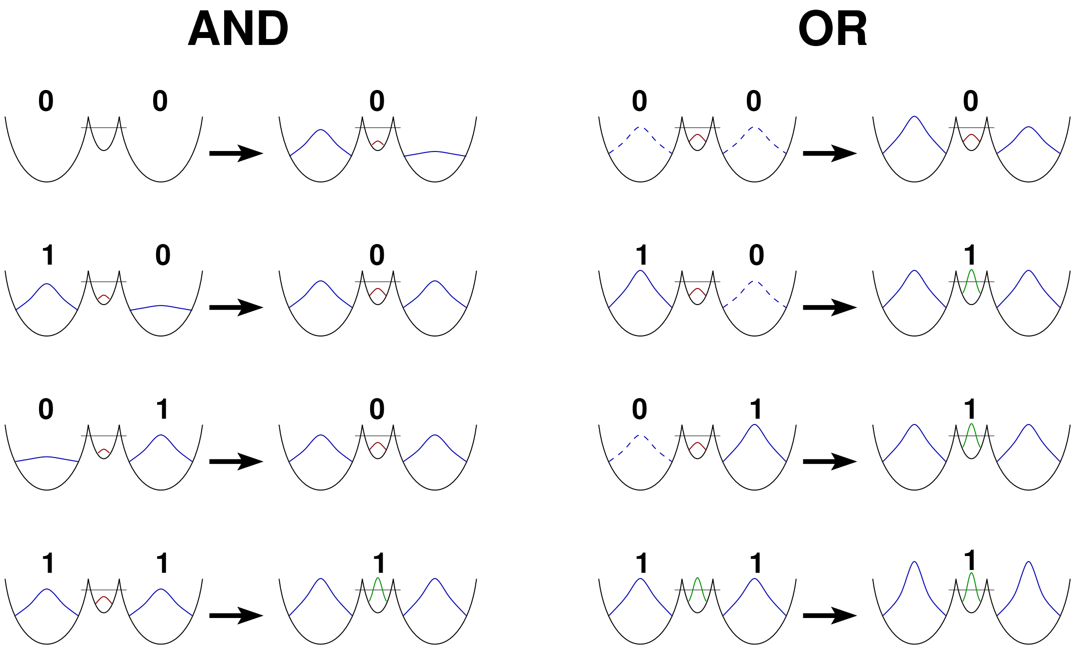

Figure 3.7: Schematic demonstration of the implementation of the logical functions ’AND’ and ’OR’ using three coupled quantum dots. The outer dots are filled with up to one electron each (input). An additional electron is utilized for the readout causing the electron density in the centered dot to exceed a minimum value if the system is in state ’1’ (output). For the implementation of the ’OR’ function, the system has to be pre-filled with one electron. This is visualized by the dashed lines.

The parameters describing the confining potential have to be chosen carefully. If the combination of the distance between the outer dots x_0, the energy offset of the inner dot V_0, and the harmonic oscillator strengths ω_i results in an effective potential that causes the electrons to be highly localized in one of the outer dots, the electron density in the centered dot is small. An additional electron does not provoke a relevant change of the electron density in the inner dot in this case. If the potential is very shallow and the difference between the ground states of the inner and outer dots is small, the electrons are evenly distributed in the device. Once again, the effect of an additionally inserted electron is small.

Path integral Monte Carlo simulations were performed for temperatures T = 100 K and 300 K. Due to the high mobility of the electrons at these temperatures, the size of the dots had to be decreased, i.e., the harmonic oscillator strengths had to be increased. $\hbar\omega_1$ was set to 20 meV for T = 100 K and to 30 meV for T = 300 K. x_0 was varied from 2 to 10 a_0^*, V_0 from 0 to 10 E_H^*, and $\hbar\omega_2$ from 10 to 60 meV.

For the determination of the state of the system, the outer dots do not have to be taken into account. It is sufficient to focus on the central one.

For T = 100 K, the device works well over a broad range of parameter settings. As an example, Fig. 3.8 shows the electron density in the centered dot at y = 0 for x_0 = 2 a_0^*, V_0 = 1.2 E_H^* and $\hbar\omega_1$ = $\hbar\omega_2$ = 20 meV. To take spin flips into account, the average values of all possible spin configurations are plotted. The total electron density in the centered dot is 0.147 for N = 1, 0.308 for N = 2, and 0.550 for N = 3. The total electron density can be clearly distinguished for the different particle numbers indicating that the system depicted here can be used to implement logical functions.

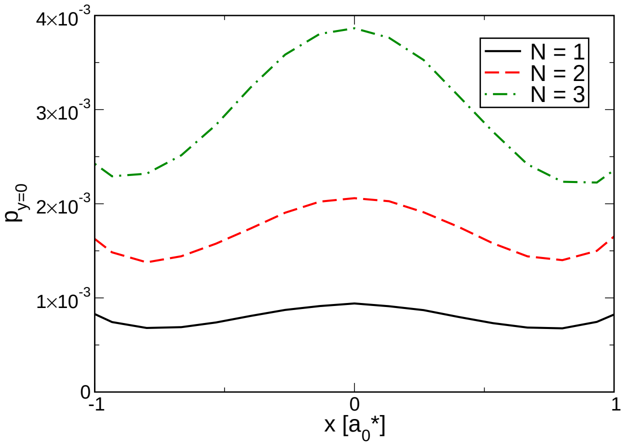

Figure 3.8: Electron density of the centered dot at y = 0 and for up to three electrons. The system's parameters are T = 100 K, x_0 = 2 a_0^*, V_0 = 1.2 E_H^* and $\hbar\omega_1$ = $\hbar\omega_2$ = 20 meV.

At T = 300 K, it is more problematic to find an optimal confining potential because a new effect arises, which can be explained as follows: While one electron might be highly localized in one of the dots with a non-vanishing wavefunction in the central dot, the Coulomb interaction is responsible for a smaller electron density in the central dot if the number of electrons is increased. The electrons are dispersed, resulting in higher probabilities of finding the electrons in the outer dots. This effect is demonstrated in Fig. 3.9a, where the potential is given by x_0 = 6 a_0^*, V_0 = 2 E_H^* and $\hbar\omega_1$ = $\hbar\omega_2$ = 30 meV. The total electron density in the central dot is 0.205 for N = 1, 0.218 for N = 2 and 0.171 for N = 3.

Decreasing the distance between the single dots and the potential energy offset allows us to obtain a device with desirable properties at room temperature. Figure 3.9b demonstrates that x_0 = 4 a_0^*, and V_0 = 1 E_H^* are optimal settings. Here, the densities are 0.245 for N = 1, 0.530 for N = 2, and 0.752 for N = 3.

By tuning the device as illustrated in Fig. 3.9a, it can be used to perform logical 'NAND' or 'NOR' functions, i.e., the inverse counterparts of 'AND' and 'OR'. While the 'AND' and 'OR' systems are 'ON' if at least three electrons are inside, their inverse counterparts are 'ON' if less than three electrons are in the system.

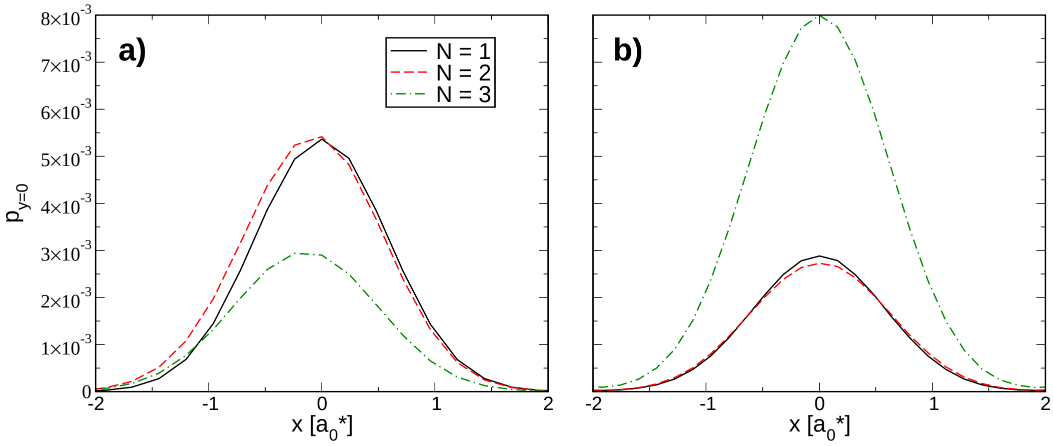

Figure 3.9: Electron density of the centered dot at y = 0 and for up to three electrons. Both plots are for T = 300 K, and $\hbar\omega_1$ = $\hbar\omega_2$ = 30 meV. The potential of a) is described by x_0 = 6 a_0^*, and V_0 = 2 E_H^*, while in b) x_0 = 4 a_0^*, and V_0 = 1 E_H^* are used.

4 Conclusion

In conclusion, the studies presented in this chapter demonstrate that quantum dot molecules consisting of two or three dots with different physical properties can be used to implement functional nanoscopic structures for microelectronics. Whether the structures introduced here can be used in more complex devices has to be determined through further studies. If it is possible to couple a large number of quantum dots to multi-dot structures, these devices are ideal candidates for fabricating highly integrated semiconductor circuits and reducing their size significantly. More studies need to be performed to investigate long-range correlations between electrons in different devices or additional temperature dependent effects such as phonon couplings. These effects have to be taken into account when designing complex circuits. These effects may, of course, produce unwanted artefacts, but if the physical properties are well known, it might be possible to utilize them in order to miniaturize the integrated circuit even further.

4 The geometric structure of small sodium clusters

1 Introduction

Clusters are compounds consisting of a countable number of atoms. They contain between two and several thousand atoms. For small systems, the field of cluster physics overlaps with atomic and molecular physics. On the other end of the scale, cluster physics connects to solid state physics.

In the beginning of cluster research, the experimentally available systems were quite small, containing only a few dozen atoms. It was thought that these systems could be treated as small molecules and that every cluster could be considered to be essentially unique. It was not expected to find patterns relating the properties of clusters with their size or the used material. Larger systems were thought of as bulk material [100].

In 1983, W. Knight's pioneering experiments changed this way of thinking. His group managed to produce and detect clusters of alkali metals with up to 100 atoms and found the electronic structure to be determined by a spherical potential well [125]. This was deduced from the more frequent occurrence of clusters in which the number of valence electrons matched the spherical shell closing numbers. Independently, Ekardt published theoretical results obtained using the self-consistent jellium model, which predicted the same behavior [61, 62]. The jellium model is based on the experimental finding that the detailed ionic core structure does not affect the properties of the clusters. The electrons are treated as moving freely in a uniformly positively charged background [37].

Due to the fact that the jellium model completely neglects the ionic structure, it only works for a limited number of systems with highly delocalized electrons. For small systems, quantum chemical methods or molecular dynamics calculations are superior to explain the details of experimental data [37]. *Ab initio* calculations have only been applied to small clusters since the computational effort is enormous [24, 25, 89, 162].

This effort can be remarkably reduced by treating the nucleus and core electrons as one unit and only studying the valence electrons separately. The ionic core is described by an effective potential - the so-called 'pseudopotential' or 'effective core potential.' Generally speaking, the pseudopotentials combine the attraction caused by the nucleus, the repulsion provoked by the core electrons, and the Pauli principle [138]. With this simple approach, cluster sizes of about 20 particles have been studied in detail [158, 164], and by compromising the accuracy and introducing approximations, particle numbers of some tens or even hundreds can be achieved [183, 221].

Sodium clusters are probably the best studied metal clusters. They are not only experimentally [65, 100, 142, 186, 194], but also theoretically [25, 37, 40, 90, 92, 157, 192] still a topic of great interest. This is due to the fact that only one valence electron per atom must be considered using the techniques described above.

S. Kümmel et al. have developed a model potential, i.e., a pseudopotential which consists of analytic functions. The parameters of these functions are adjusted to match properties known from experiments. They have shown that their pseudopotential does well at describing the ionic and electronic structure of sodium clusters for up to N = 59 using the 'cylindrically averaged pseudopotential scheme' (CAPS) [138, 139]. The main idea of CAPS is to reduce the dimensionality of the numerical problem by including symmetry considerations and thus to minimize the numerical effort of density functional calculations.

The potential of Kümmel et al. is defined by (see Fig. 4.1)

$$V_p(r) = -\frac{Ze^2}{r}\left[c_1\,\mathrm{erf}\left(\frac{r}{\sqrt{2}\sigma_1}\right) + c_2\,\mathrm{erf}\left(\frac{r}{\sqrt{2}\sigma_2}\right)\right], \tag{4.1}$$

where the error function is

$$\mathrm{erf}(x) = \frac{2}{\sqrt{\pi}}\int_0^x \mathrm{d}y\ \exp(-y^2). \tag{4.2}$$

The parameters c_1, c_2, σ_1, σ_2 are chosen to reproduce the experimental data given in [1, 7, 8]:

$$\sigma_1 = 0.681\,a_0, \qquad c_1 = -2.292, \tag{4.3}$$

$$\sigma_2 = 1.163\,a_0, \qquad c_2 = 3.292. \tag{4.4}$$

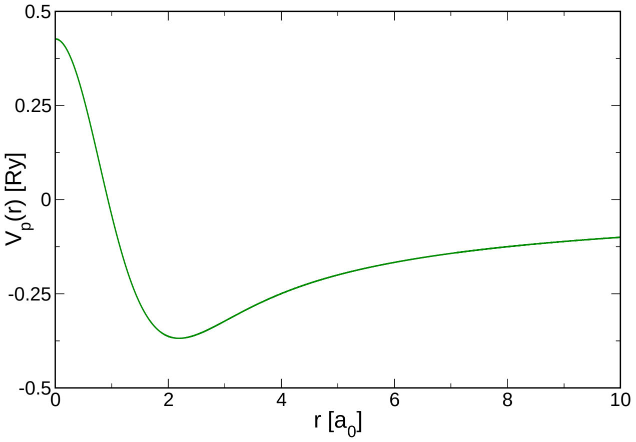

Figure 4.1: The pseudopotential as defined by Kümmel et al. [139].

2 The path integral Monte Carlo technique

Path integral Monte Carlo calculations for sodium clusters with up to four ionic sodium cores are presented here. Since solving the exact many body problem in three dimensions would by far exceed the available computing resources, some simplifications are introduced. The ionic cores including the nucleus and the closed electron shells are treated as classical particles underlying Boltzmann statistics. In contrast to the cores, the valence electrons are handled quantum mechanically and the interaction between the cores and the valence electrons is modeled by the pseudopotential of Kümmel et al. (Eq. (4.1)). Particles of the same type interact through Coulomb repulsion.

The electronic temperature t and the ionic temperature T are varied separately. For comparison with results of other authors, the electronic temperature should be set to zero. Obviously, this is not possible using the path integral Monte Carlo approach since convergence can not be achieved in this case. Therefore, t is kept as small as possible, i.e., 500 K to 4000 K. Since atomic level spacings are generally on the order of up to some eV, these temperatures can still be considered small (1 eV corresponds to 11605 K).

To mimic the positions of the sodium atoms, the following types of pair correlation functions and radial densities are introduced. $\Gamma_{\mathrm{Na}^+-\mathrm{Na}^+}(r)$ describes the probability of finding two ionic sodium cores (Na^+) with distance r. $\rho_{\mathrm{Na}^+}(r)$ is the radial density of sodium cores. $\Gamma_{\mathrm{Na}^+-\mathrm{e}\uparrow}(r)$ and $\Gamma_{\mathrm{Na}^+-\mathrm{e}\downarrow}(r)$ are the Na^+ - electron pair correlation functions.

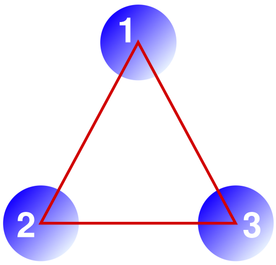

Figure 4.2: Geometry of Na_3^+ [138].

Two small sodium clusters, namely Na_3^+ and Na_4^+, are studied here. In both cases, the spins of the electrons are fixed. While the Na_3^+ simulations were performed for a total electron spin S = 0, the Na_4^+ cluster has a total electron spin S = 1/2.

Figure 4.2 shows the stable configuration of Na_3^+, where the three atoms are arranged on a triangle with equal bond lengths. The bond lengths can easily be obtained from the maxima of the ionic radial densities and pair correlation functions as illustrated in Fig. 4.3. The origin of the coordinate system is in the center of the triangle.

PIMC (5 K)	CAPS	DFT/LSD	HF	CI
6.32 a_0	6.62 a_0	6.00 a_0	6.96 a_0	6.41 a_0

Table 4.1: Comparison of bond lengths for Na_3^+ obtained by the path integral Monte Carlo technique (PIMC), the cylindrically averaged pseudopotential scheme (CAPS) [139], density functional theory with the local spin density approximation (DFT/LSD) [157, 158, 164], Hartree-Fock calculations (HF) [23, 24], and full configuration interaction calculations (CI) [25].

For comparison with the PIMC results, Tab. 4.1 shows bond lengths of other authors using different techniques, i.e., the cylindrically averaged pseudopotential scheme

(CAPS) [137, 139], density functional theory with the local spin density approximation (DFT/LSD) [157, 158, 164], *ab initio* Hartree-Fock calculations (HF) [23, 24], and full configuration interaction calculations (CI) [25]. It is known that *ab initio* Hartree-Fock calculations overestimate the bond lengths due to the missing correlation effects and that the full CI calculations have been performed to achieve more accurate results. The results obtained using the local spin density approximation are an underestimation [24, 139]. The pseudopotential used for the CAPS calculations has been adjusted to compensate this underestimation and to accurately reproduce experimental results. Although our calculations utilize the same potential for the electron-ion interaction, the results differ by about 0.3 a_0. This is not surprising because the parameters describing the pseudopotential are optimized for CAPS calculations only. The PIMC result is in good agreement with the bond length obtained by the CI calculations and deviates by 0.09 a_0.

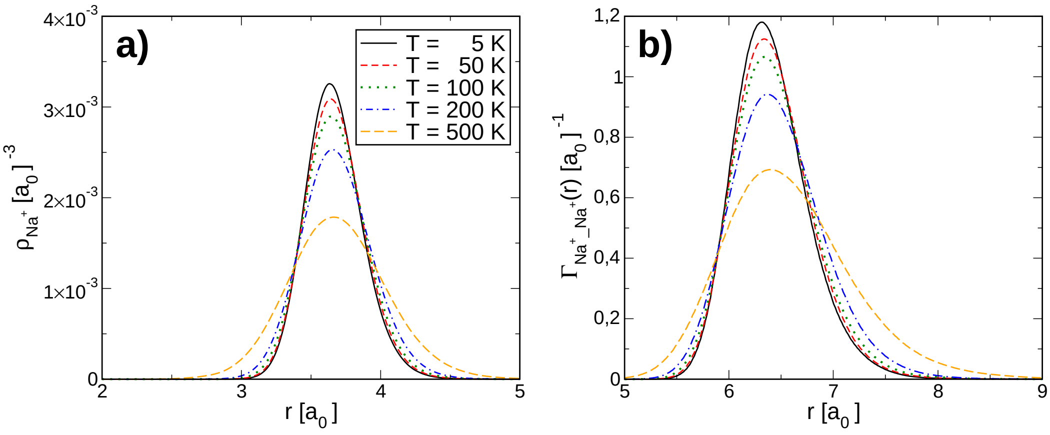

Figure 4.3: Radial ionic density (a) and pair correlation functions (b) for Na_3^+ at different temperatures.

Results of temperature dependent calculations for T = 5, 50, 100, 200, and 500 K are presented in Fig. 4.3. The positions of the maxima of the radial density of Na^+ ions (a), as well as of the corresponding pair correlation functions (b) vary only slightly with increasing temperature. This indicates a stable triangular cluster structure. Martins et al. calculated the dissociation energies of small sodium clusters, which confirm a very stable cluster geometry [158]. For Na_3^+, they obtained 1.55 eV, which is significantly larger than the bulk value (1.11 eV). The broadening of the graphs for higher temperatures is caused by the higher mobility of the ions. The small variation of the positions of the maxima leads to the conclusion that the bond lengths of our path integral Monte Carlo simulations at 5 K are comparable with the results of other authors obtained at 0 K.

Next, simulations of Na_4^+ are presented. The three stable isomers are shown in Fig. 4.4.

The Na_4^+ cluster requires the electronic temperature t to be increased in order to achieve convergence of the Monte Carlo simulation. Simulations were performed for t = 2000 to 4000 K. At these temperatures, evaporation of the cluster occurs for a broad range of simulation parameters. If the temperature is chosen too high and the number

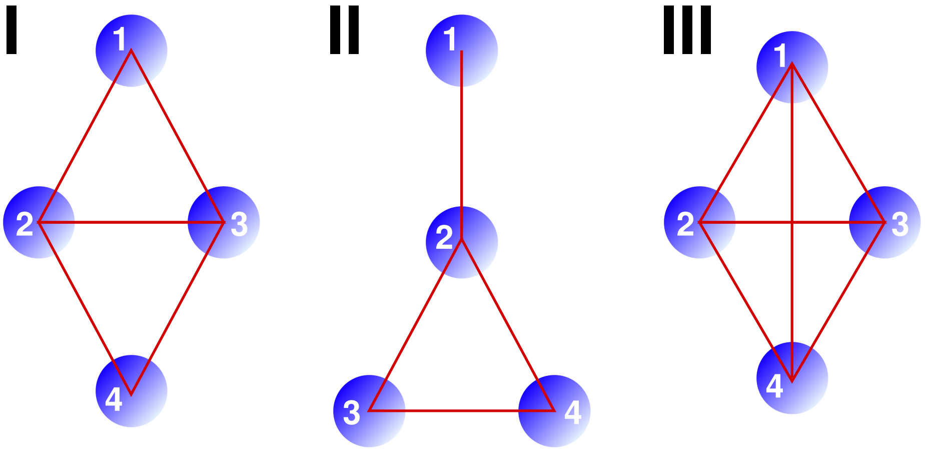

Figure 4.4: The three stable isomers of Na_4^+ [162]: (I) has the shape of a flat rhombus, (II) is usually referred to as the T-form and (III) has a tetraeder-like structure.

of timeslices too small, the system behaves as if it consisted of single uncorrelated ions and electrons and no clusters are formed. On the other hand, if the number of timeslices is too high or the system temperatures are too low, convergence cannot be achieved.

Figure 4.5 shows pair correlation functions of evaporated and non-evaporated Na_4^+ clusters. If a cluster evaporates, the internuclear binding is lost and the ionic cores no longer need to be thoroughly localized. This causes the peaks of the pair correlation function to flatten out.

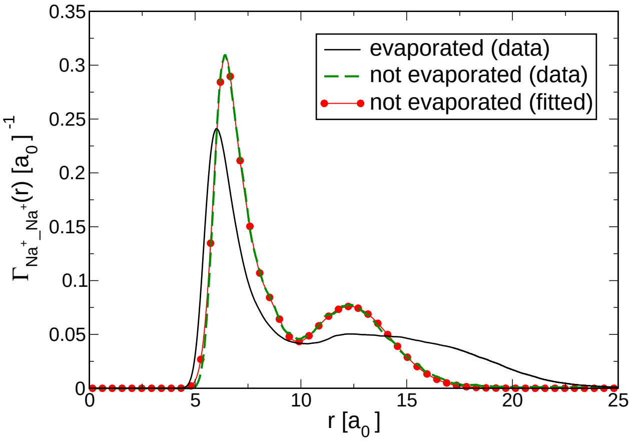

Figure 4.5: Pair correlation functions of evaporated and non-evaporated Na_4^+ clusters at t = 4000 K, T = 100 K, M = 250 (straight line), and t = 2000 K, T = 30 K, M = 500 (dashed line). The non-evaporated data is fitted by Eq. (4.5) with the parameters from Tab. 4.2 (straight-dotted line).

In contrast to the Na_3^+ cluster, the dissociation energy of the Na_4^+ cluster is significantly smaller than the bulk value, i.e., 0.68 eV [158]. This indicates the lower stability of the cluster.

In the following, an Na_4^+ cluster with t = 2000 K, T = 30 K, and M = 500 corresponding to the non-evaporated case in Fig. 4.5 is discussed exclusively.

In order to extract the bond lengths from the simulation data, the pair correlation function is fitted by a superposition of Gauss functions. Each Gauss function represents the correlation between two ionic cores. In the case of Na_4^+, six Na^+-Na^+ correlations have to be taken into account and since the integral of the total pair correlation function is normalized to one, each bond contributes 1/6. Thus, the height and width of each Gauss function can be expressed by a single parameter a_i. The bond lengths are represented by the most probable particle distances, i.e., the position r_i of the maxima of the single Gauss functions. The total function applied for a non-linear least-square fit using the Marquardt-Levenberg algorithm is [156]

$$\Gamma^{\mathrm{fit}}_{\mathrm{Na}^+-\mathrm{Na}^+}(r) = \sum_{i=1}^{6} \frac{1}{6a_i\sqrt{2\pi}} \exp\left(-\frac{(r-r_i)^2}{2a_i^2}\right) . \tag{4.5}$$

This equation has 12 independent parameters a_i, r_i. It was found that the best fit can be obtained by reducing the number of independent parameters and assuming only four different Gauss functions. This can be verified by the symmetry of the isomers shown in Fig. 4.4, where two bond lengths occur twice in each geometry.

To fit the data presented in Fig. 4.5, the parameters shown in Tab. 4.2 are utilized. For comparison to Fig. 4.4, in the last row of Tab. 4.2 the numbers of the particles with distance r_i are given.

i	a_i	r_i	MRCI	CI	Binding
1	0.39 a_0	6.24 a_0	6.55 a_0	6.16 a_0	3-4
2	0.72 a_0	6.87 a_0	6.65 a_0	6.59 a_0	2-3, 2-4
3	1.07 a_0	8.50 a_0	7.11 a_0	6.71 a_0	1-2
4	1.74 a_0	12.50 a_0	13.30 a_0	12.91 a_0	1-3, 1-4

Table 4.2: Parameters applied to fit the data in Fig. 4.5 using Eq. (4.5) and the bond lengths of Mishima et al. [162] (MRCI) and Bonacic-Koutecky et al. [25] (CI). The last column displays the corresponding particles of isomer II in Fig. 4.4.

At T = 30 K, the ionic core distances calculated using the path integral Monte Carlo simulation predict an Na_4^+ cluster with the shape of isomer II. It is impossible to construct a rhombus- or tetraeder-like structure using the calculated length proportions.

The Gauss functions used to fit the proportion of $\Gamma_{\mathrm{Na}^+-\mathrm{Na}^+}(r)$ belonging to sodium core number 1 (i = 3,4) are broader than the ones corresponding to the triangular structure in the lower part of the cluster (i = 1,2). This shows that, due to its weaker binding, the upper ionic core is not as thoroughly localized as the other ones.

The choice of isomer II is strengthened by the Na^+-electron and electron-electron pair correlation functions as shown in Fig. 4.6a and Fig. 4.6b. $\Gamma_{\mathrm{Na}^+-\mathrm{e}^\uparrow}(r)$ and $\Gamma_{\mathrm{e}^\uparrow-\mathrm{e}^\uparrow}(r)$ indicate that one electron is responsible for the 1-2 binding, and that the remaining spin $\uparrow$ electron is localized in the area of the triangular structure consisting of the Na^+ cores 2,3, and 4. It is responsible for the 3-4 binding and together with the single spin $\downarrow$ electron for the 2-3 and 2-4 bindings. It can be inferred from $\Gamma_{\mathrm{e}^\downarrow-\mathrm{e}^\uparrow}(r)$ that the

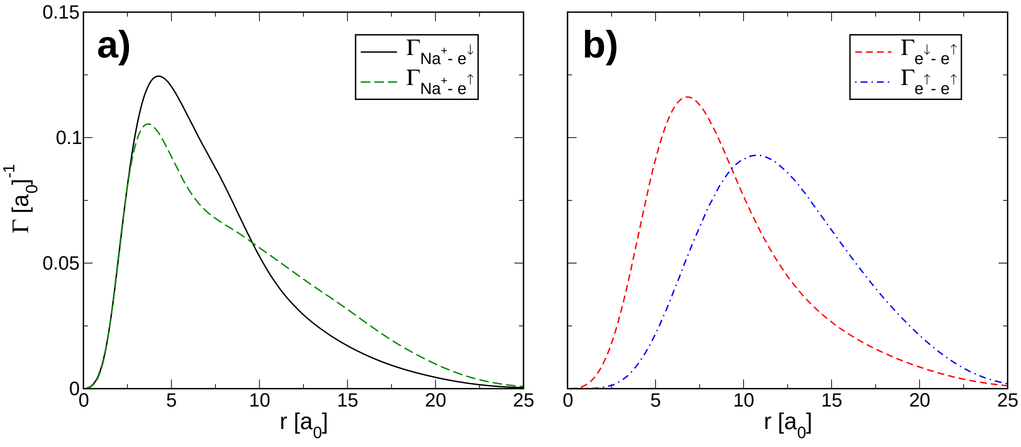

Figure 4.6: Na$^+$-electron (a) and electron-electron (b) pair correlation functions at t = 2000 K, T = 30 K, M = 500.

distance between the spin ↓ electron and both spin ↑ electrons is similar. With this in mind, $\Gamma_{\mathrm{Na}^+-\mathrm{e}^\downarrow}(r)$ clearly shows that the spin ↓ electron is localized in the area around core number 2.

The influence of the Pauli principle is not insignificant at T = 30 K. This is visualized by the difference of $\Gamma_{\mathrm{e}^\uparrow-\mathrm{e}^\uparrow}(r)$ and $\Gamma_{\mathrm{e}^\uparrow-\mathrm{e}^\downarrow}(r)$. Without Pauli repulsion, the pair correlation functions would be equal.

The bond lengths of Na_4^+ are compared to the multi-reference configuration interaction (MRCI) data of Mishima et al. [162], and full configuration interaction (CI) data of Bonacic-Koutecky et al. [25] (See Tab. 4.2).

While the MRCI bond lengths are known to be an overestimation [162], the path integral Monte Carlo approach predicts even larger values for 1-2, and 2-3/2-4. The 3-4 binding is 0.31 a$_0$ smaller than the MRCI result, but only 0.08 a$_0$ larger than the corresponding CI value. The 1-3/1-4 distance is 0.8 a$_0$ smaller than the corresponding MRCI value and 0.41 a$_0$ smaller than the CI result.

Several different facts can explain this effect: As already stated, the parameters of the pseudopotential have not been optimized for path integral Monte Carlo simulations. The more complex a system is, the more significant are the consequences if the pseudopotential is not well optimized. While the PIMC calculations are performed at 30 K, the MRCI and CI calculations are performed at 0 K which is another possible explanation for the deviation of the results. Additionally, the electron spins are fixed in the PIMC calculations. Further simulations are necessary to study the influence of different spin configurations on $\Gamma_{\mathrm{Na}^+-\mathrm{Na}^+}(r)$.

3 Conclusion and outlook

The studies presented in this chapter were performed to demonstrate that combining the path integral Monte Carlo technique with the classical movement of the ionic cores yields an approach well-suited to study small sodium clusters. This was accomplished by successfully reproducing the results obtained by other techniques.

For future simulations, the parameters of the pseudopotential need to be optimized to obtain more accurate results.

With our technique and the available computational power, it is not possible to study clusters including more than four atoms. Even for these small systems, a single simulation run at 30 K takes up to a few days on 62 Alpha processors. Further algorithmic improvements are necessary to reduce the number of Monte Carlo steps needed.

If one succeeds in reducing the numerical problems and optimizing the pseudopotential, the path integral Monte Carlo technique with the classical movement of the ionic cores could be a powerful tool for studying geometries and temperature dependent effects of small clusters. For example, the transition from solid- to liquidlike behavior of small clusters is a topic of interest, but requires clusters with at least seven atoms to be studied [91].

III

Thermodynamic properties of selected finite systems

1

Calculation of thermodynamic properties of finite Bose-Einstein systems

P. Borrmann, J. Harting, O. Mülken, and E.R. Hilf

Physical Review A 60, 1519 (1999)

PHYSICAL REVIEW A VOLUME 60, NUMBER 2 AUGUST 1999

Calculation of thermodynamic properties of finite Bose-Einstein systems

Peter Borrmann,* Jens Harting, Oliver Mülken, and Eberhard R. Hilf
Department of Physics, Carl von Ossietzky University, Oldenburg, D-26111 Oldenburg, Germany

(Received 26 August 1998)

We derive an exact recursion formula for the calculation of thermodynamic functions of finite systems obeying Bose-Einstein statistics. The formula is applicable for canonical systems where the particles can be treated as noninteracting in some approximation, e.g., like Bose-Einstein condensates in magnetic traps. The numerical effort of our computation scheme grows only linearly with the number of particles. As an example, we calculate the relative ground-state fluctuations and specific heats for ideal Bose gases with a finite number of particles enclosed in containers of different shapes. [S1050-2947(99)04203-1]

PACS number(s): 03.75.Fi, 05.30.Jp, 32.80.Pj

With the observation of Bose-Einstein condensation (BEC) of magnetically [1–3] and optically [4] trapped atoms, new insights into the nature of this state of matter have been given. The experimental situation is in all cases quite different from the ideal gas treated within the grand-canonical ensemble, which is the standard textbook example. First, the number of particles within the traps is fixed and finite, which suggests a canonical or microcanonical treatment of the systems. Second, the confining trap potentials greatly influence the condensate properties. Third, although the trapped gases are quite dilute, the validity of the treatment as noninteracting particle gases has to be checked from case to case.

Even within the approximation of noninteracting particles, the calculation of the thermodynamic properties of the Bose-Einstein systems remains a difficult mathematical problem. Recently, some approximate methods to calculate the fluctuation of the ground-state occupation number in a trapped Bose-Einstein condensate have been developed [5–8]. Here we present an exact method to calculate all thermodynamic quantities of finite canonical Bose systems, given the one-particle density of states.

As the starting point, we utilize the recursive formula of the canonical partition function for a system of N noninteracting bosons as given in [9]

$$Z_N(\beta)=\frac{1}{N}\sum_{k=1}^{N} Q_k(\beta)Z_{N-k}(\beta), \tag{1}$$

where $Q_k(\beta)=Z_1(k\beta)=\Sigma_i\exp(-k\beta\epsilon_i)$ is the one-particle partition function at the temperatures $k\beta$ and $Z_0(\beta)=1$. The microcanonical partition $\Gamma_N(E)$ can be calculated by an inverse Laplace-transform of Eq. (1) and is given by

$$\begin{aligned}\Gamma_N(E)&=\frac{1}{N}\sum_{k=1}^{N}\frac{1}{2\pi i}\int_{c-i\infty}^{c+i\infty}d\beta\,\exp(\beta E)Q_k(\beta)Z_{N-k}(\beta)\\&=\frac{1}{N}\sum_{k=1}^{N}\int_0^E dE'\,\Gamma_1^k(E')\Gamma_{N-k}(E-E'),\end{aligned} \tag{2}$$

where $\Gamma_1^k(E)$ is the inverse Laplace transform of $Q_k(\beta)$ and $\Gamma_0(E)=\delta(E)$. A similar, slightly less general, equation has recently been derived by Weiss and Wilkens [10].

Equation (1) can be used to calculate all thermodynamic quantities by appropriate differentiation of $\ln Z_N$. However, in any case Z_N occurs as a normalization factor and has to be calculated explicitly. This turns out to be a major drawback. First, the numerical effort to calculate Z_N grows with the square of the particle number N. Moreover, since $Z_N(\beta)$ grows exponentially with N, multiple precision arithmetic is required for proper calculation. We will present a method avoiding these difficulties.

To ease our derivations we rewrite $Z_N(\beta)$ utilizing the $\mathcal{Z}$ transform and define

$$\mathcal{Z}(Z)=F(x)=\sum_{k=0}^{\infty}\frac{Z_k(\beta)}{x^k}, \tag{3}$$

$$\mathcal{Z}(Q)=G(x)=\sum_{k=0}^{\infty}\frac{Q_k(\beta)}{x^k}, \tag{4}$$

where we define $Q_0(\beta)=0$. Taking advantage of the basic properties of the $\mathcal{Z}$ transform, Eq. (1) can be written in the form

$$-x\frac{d}{dx}F(x)=F(x)G(x), \tag{5}$$

yielding[1]

$$F(x)=\exp\left(\sum_{k=1}^{\infty}\frac{Q_k(\beta)}{k}x^{-k}\right). \tag{6}$$

Applying the inverse $\mathcal{Z}$ transform, we may write $Z_N(\beta)$ as

$$Z_N(\beta)=\frac{1}{2\pi i}\int_C F(x)x^{N-1}dx, \tag{7}$$

---

*Author to whom correspondence should be addressed. Electronic address: borrmann@uni-oldenburg.de

[1] Note that $F(x)$ is closely related to the grand-canonical partition function.

©1999 The American Physical Society

where $C:=\{z\in C:|x|=r\}$ and r has to satisfy the condition $|Z_N(\beta)|\leqslant \exp(rN)$. Alternatively we may write

$$Z_N(\beta)=\frac{1}{N!}\,\frac{d^N}{dx^N}F(1/x)|_{x=0}. \tag{8}$$

Using Eq. (8), the number of particles with energy ϵ_i can be calculated by

$$\begin{aligned}\eta_i(N,\beta)&=\frac{-1}{\beta}\,\frac{\partial}{\partial\epsilon_i}\ln Z_N(\beta)\\&=\frac{1}{Z_N(\beta)}\sum_{k=1}^{N}\exp(-\beta k\epsilon_i)Z_{N-k}(\beta).\end{aligned}\tag{9}$$

Some reordering yields

$$\eta_i(N+1,\beta)=\frac{Z_N(\beta)}{Z_{N+1}(\beta)}\exp(-\beta\epsilon_i)[\eta_i(N,\beta)+1]. \tag{10}$$

Since the particle number is a conserved quantity in the canonical ensemble, the direct calculation of the normalization factor can be omitted by using the relation

$$\frac{Z_N(\beta)}{Z_{N+1}(\beta)}=\frac{N+1}{\sum_{i=0}^{\infty}\exp(-\beta\epsilon_i)[\eta_i(N,\beta)+1]}. \tag{11}$$

For Fermi systems, the recursion formula

$$\eta_i(N+1,\beta)=\frac{Z_N(\beta)}{Z_{N+1}(\beta)}\exp(-\beta\epsilon_i)[1-\eta_i(N,\beta)] \tag{12}$$

with

$$\frac{Z_N(\beta)}{Z_{N+1}(\beta)}=\frac{N+1}{\sum_{i=0}^{\infty}\exp(-\beta\epsilon_i)[1-\eta_i(N,\beta)]} \tag{13}$$

can be derived in a similar manner. In practice, only a limited number of energy levels has to be taken into account, since the occupation probability rapidly decreases with increasing energy eigenvalues. Equations (10) and (11) are extremely useful in practical calculations. The numerical effort to calculate the occupation numbers grows only linear with the number of particles. Moreover, only a moderate arithmetic precision is required. Having the occupation probabilities at hand, the energy expectation value is given by

$$E(N,\beta)=\sum_{i=0}^{\infty}\epsilon_i\eta_i(N,\beta). \tag{14}$$

The calculation of the fluctuation of the occupation probabilities $\delta\eta_i(N,\beta)$ is a little bit more complicated and contains another recursion:

$$\begin{aligned}[\delta\eta_i(N+1,\beta)]^2&=\frac{1}{\beta^2}\,\frac{\partial^2}{\partial\epsilon_i^2}\ln[Z_{N+1}(\beta)]\\&=\frac{-1}{\beta}\,\frac{\partial}{\partial\epsilon_i}\eta_i(N+1,\beta)\\&=\frac{Z_N(\beta)}{Z_{N+1}(\beta)}\exp(-\beta\epsilon_i)\{\delta^2\eta_i(N,\beta)\\&\quad+[\eta_i(N+1,\beta)+1]\\&\quad\times[\eta_i(N,\beta)-\eta_i(N+1,\beta)+1]\}.\end{aligned}\tag{15}$$

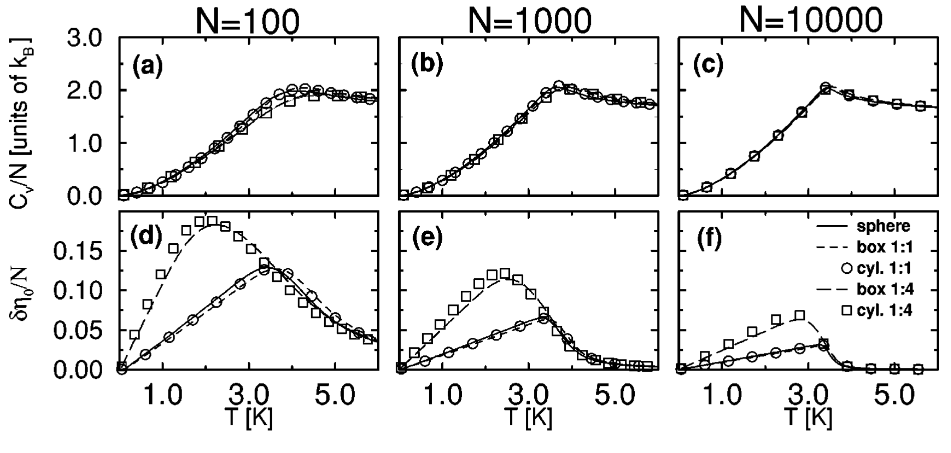

FIG. 1. (a)–(c) Specific heats C_V/N and (d)–(f) ground-state fluctuations as a function of the canonical temperature for systems of $N=100$, $N=1000$, and $N=10\,000$ particles. The solid lines represent the results for a spherical trap, the dashed lines for a cube, the circles for a cylinder with a diameter to height ratio of $d/L=1$, the long dashed lines for a box with side lengths $L_z=4L_y=4L_x$, and the squares for a cylinder with $d/L=1/4$. In all cases the particle density is taken to be $\rho=0.0216$ Å^{-3}.

To illustrate the usefulness of our recursion formulas, we consider the ideal gas with parameters of liquid helium in containers of different shapes: (i) a cube with side length L_x, L_y, L_z and energy levels

$$E_{n_x,n_y,n_z}=\frac{\pi^2\hbar^2}{2m_{\mathrm{He}}}\left(\frac{n_x^2}{L_x^2}+\frac{n_y^2}{L_y^2}+\frac{n_z^2}{L_z^2}\right), \tag{16}$$

(ii) a sphere with radius a and energy levels

$$E_{n,l}=\frac{\hbar^2}{2m_{\mathrm{He}}a^2}u_{n,l} \tag{17}$$

and degeneracy $\sigma_{n,l}=2l+1$, and (iii) a cylinder with diameter $d=2a$, height L, and energy levels

$$E_{n,l,m}=\frac{\hbar^2}{2m_{\mathrm{He}}}\left(\frac{v_{n,l}^2}{a^2}+\frac{m^2\pi^2}{L^2}\right) \tag{18}$$

with $n=1,2,\ldots,$ $l=1,2,3,\ldots,$ and $m=\cdots-1,0,-1\cdots$. We denoted the zeros of the half-integer Bessel functions $J_{n+1/2}(r)$ by $u_{n,l}$ and the zeros of the integer Bessel function $J_n(r)$ by $v_{n,l}$.

Figure 1 displays the specific heats and the fluctuations of the ground-state occupation number $\delta\eta_0/N$ as a function of the canonical temperature for different trap geometries and $N=100{,}1000$, and 10 000 He atoms. In all cases, the particle density is taken to be $\rho=0.0216$ Å^{-3}. With growing system size the differences between the specific heats for the different trap geometries almost vanish and approach the typical shape of the curve for the ideal Bose gas. That is, with respect to the specific heat the boundary conditions become more and more unimportant with increasing volume. In contrast, the ground-state fluctuations exhibit a completely different behavior. The cubic box, the *compact* cylinder with equal diameter and height, and the sphere show almost equal ground-state fluctuations for all system sizes, while the ground-state fluctuations of the stretched box and the stretched cylinder are remarkably larger for temperatures below the critical temperature. This effect is not unexpected because restricting the particle motion in one or two dimensions makes the system act like a lower-dimensional system, which are known to show larger fluctuations. Moreover, the differences between the fluctuations of the *stretched* traps and the *compact* traps do not decrease with increasing system size. The reason for this behavior is found in the energy difference between the ground state and the first excited level, which is much larger for the *stretched* traps than for the *compact* traps. Since $\delta\eta_0/N$ decreases approximately with $N^{-1/3}$, the infinite particle number limit is the same for all trap geometries. Under experimental considerations our results imply that the stability of the condensate fraction in anisotropic traps should be considerably smaller than in isotropic traps. In Fig. 1 we plotted $\delta\eta_0/N$ to allow good comparison with previous published results [8,5]. Since this quantity goes to zero as the system size increases, it is a bad indicator for phase transitions. The relative ground-state fluctuation $\delta\eta_0/\eta_0$ shown in Fig. 2 is much more conclusive in this respect.

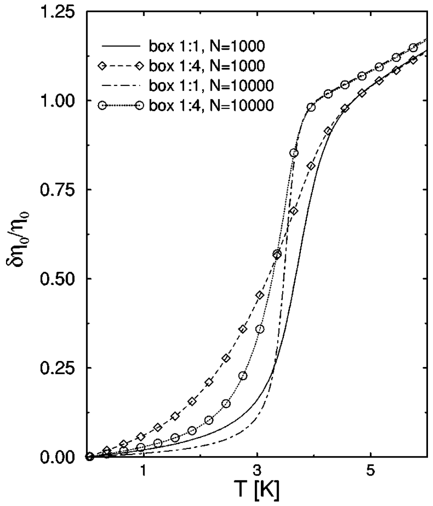

FIG. 2. Relative ground-state fluctuations $\delta\eta_0/\eta_0$ as a function of temperature for the cubic box and the stretched box and $N=1000$ and 10 000 particles.

True phase transition only occurs for infinite systems. However, it is well known from other systems, e.g., finite spin lattices and clusters [11,12], that finite systems already display the onset of phase transitions. Instead of having a well defined critical temperature, the transition occurs in a broader crossover region. As can be extracted from Fig. 2, the crossover region, which is indicated by the sharp increase of $\delta\eta_0/\eta_0$, extends even for the cubic box with 10 000 atoms over a temperature range of 0.5 K. For the *stretched* trap the crossover region is about twice as large.

All calculations have been performed on an IBM-43P (233 MHz) workstation. For 1000 particles a run with 200 temperature points took about six minutes; for 10 000 particles it took one hour. A calculation of the same quantities with the recursion formula given in Eq. (1) takes about six hours for 1000 particles (and would take at least 600 hours for 10 000 particles). Moreover, due to the numerical instabilities connected with Eq. (1), $N=1000$ was the largest particle number we achieved with this formula, even though we utilized a multiple precision package.

We expect the recursion formulas to be quite useful for calculating the properties of dilute atomic Bose gases in magnetic traps with different geometry. For this purpose we provide an easy to use JAVA program,[2] which requires as input only the energy level distribution with appropriate degeneracy and calculates the basic properties of finite Bose systems with particle numbers up to 10 000. A slightly faster FORTRAN code is available upon request.

---

[2] The code is available within the World-Wide-Web: http:\\www.physik.uni-oldenburg.de\~borrmann\BEC

[1] C. Bradley, C. Sackett, J. Tollet, and R. Hulet, Phys. Rev. Lett. **75**, 1687 (1995).
[2] M. Anderson *et al.*, Science **69**, 198 (1995).
[3] K. Davies *et al.*, Phys. Rev. Lett. **75**, 3969 (1995).
[4] D. Stamer-Kurn *et al.*, Phys. Rev. Lett. **80**, 2027 (1998).
[5] S. Grossmann and M. Holthaus, Phys. Rev. Lett. **79**, 3557 (1997).
[6] S. Grossmann and M. Holthaus, Opt. Express **1**, 262 (1997).
[7] P. Navez *et al.*, Phys. Rev. Lett. **79**, 1789 (1997).
[8] M. Gajda and K. Rzazewski, Phys. Rev. Lett. **78**, 2686 (1997).
[9] P. Borrmann and G. Franke, J. Chem. Phys. **98**, 2484 (1993).
[10] C. Weiss and M. Wilkens, Opt. Express **1**, 272 (1997).
[11] R. E. Kunz and R. S. Berry, Phys. Rev. Lett. **71**, 3987 (1993).
[12] D. J. Wales and R. S. Berry, Phys. Rev. Lett. **73**, 2875 (1994).

2

Classification of phase transitions in small systems

P. Borrmann, O. Mülken, and J. Harting

Physical Review Letters 84, 3511 (2000)

VOLUME 84, NUMBER 16 PHYSICAL REVIEW LETTERS 17 APRIL 2000

Classification of Phase Transitions in Small Systems

Peter Borrmann, Oliver Mülken, and Jens Harting
Department of Physics, Carl von Ossietzky University Oldenburg, D-26111 Oldenburg, Germany

(Received 14 October 1999)

We present a classification scheme for phase transitions in finite systems like atomic and molecular clusters based on the Lee-Yang zeros in the complex temperature plane. In the limit of infinite particle numbers the scheme reduces to the Ehrenfest definition of phase transitions and gives the right critical indices. We apply this classification scheme to Bose-Einstein condensates in a harmonic trap as an example of a higher order phase transition in a finite system and to small Ar clusters.

PACS numbers: 05.70.Fh, 64.60.Cn, 64.70.−p

Small systems do not exhibit phase transitions. Following Ehrenfest's definition this statement is true for almost all small systems. Instead of exhibiting a sharp peak or a discontinuity in the specific heat at some well-defined critical temperature the specific heat shows a more or less smooth hump extending over some finite temperature range. For example, for the melting of atomic clusters this is commonly interpreted as a temperature region where solid and liquid clusters coexist [1,2] and as a finite-system analog of a first order phase transition. Proykova and Berry [3] interpret a structural transition in TeF$_6$ clusters as a second order phase transition. A common way to investigate if a transition in a finite system is a precursor of a phase transition in the corresponding infinite system is to study the particle number dependence of the appropriate thermodynamic potential [4]. However, this approach will fail for all system types where the nature of the phase transition changes with increasing particle number which seems to be the case, e.g., for sodium clusters [5] or ferrofluid clusters [6]. For this reason a definition of phase transitions for systems with a fixed and finite particle number seems to be desirable. The only recommended feature is that this definition should reduce to the Ehrenfest definition when applied to infinite systems for systems where such limits exist. An approach in this direction has been made by studying the topological structure of the n-body phase space and *a hypothetical definition* based on the inspection of the shape of the caloric curve [7]. A mathematical more rigid investigation giving the sufficient and necessary conditions for the existence of van der Waals–type loops has been given by Wales and Doye [8].

Our ansatz presented in this Letter is based on earlier works of Lee and Yang [9] and Grossmann *et al.* [10] who gave a description of phase transitions by analyzing the distributions of zeros (DOZ's) of the grand canonical $\Xi(\beta)$ and the canonical partition function $Z(\beta)$ in the complex temperature plane. For macroscopic systems this analysis merely contributes a sophisticated view of the thermodynamic behavior of the investigated system. We will show that for small systems the DOZ's are able to reveal the thermodynamic secrets of small systems in a distinct manner. In the following we restrict our discussion to the canonical ensemble and denote complex temperatures by $\mathcal{B} = \beta + i\tau$ where β is as usual $1/k_BT$ [11].

In the case of finite systems one must not deal with special considerations regarding the thermodynamic limit. We write the canonical partition function $Z(\mathcal{B}) = \int dE \times \Omega(E)\exp(-\mathcal{B}E)$, with the density of states $\Omega(E)$, as a product $Z(\mathcal{B}) = Z_l(\mathcal{B})Z_i(\mathcal{B})$ where $Z_l(\mathcal{B})$ describes the limiting behavior of $Z(\mathcal{B})$ for $T \to \infty$ imposing $\lim_{\mathcal{B}\to 0} Z_i(\mathcal{B}) = 1$. In general, $Z_l(\mathcal{B})$ will not depend on the interaction between the particles or the particle statistics but it will depend on the external potential imposed. For example, for N particles in a d-dimensional harmonic trap we have $Z_l(\mathcal{B}) \approx \mathcal{B}^{-dN}$ and for a d-dimensional gas $Z_l(\mathcal{B}) \approx \mathcal{B}^{-dN/2}$. In the following we will assume that $Z_l(\mathcal{B})$ has no zeros except at $\mathcal{B} = \infty$. Then the zeros of $Z(\mathcal{B})$ are the same as those of $Z_i(\mathcal{B})$. Applying the product theorem of Weierstrass [12] the canonical partition function can be written as a function of the zeros of $Z_i(\mathcal{B})$ in the complex temperature plane. Because $Z(\mathcal{B})$ is an integral function its zeros $\mathcal{B}_k = \mathcal{B}^*_{-k} = \beta_k + i\tau_k$ $(k \in \mathbb{N})$ are complex conjugated

$$Z(\mathcal{B}) = Z_l(\beta)Z_i(0)\exp[\mathcal{B}\,\partial_{\mathcal{B}}\ln Z_i(0)] \times \prod_{k\in\mathbb{N}}\left(1-\frac{\mathcal{B}}{\mathcal{B}_k}\right)\left(1-\frac{\mathcal{B}}{\mathcal{B}_k^*}\right)\exp\left(\frac{\mathcal{B}}{\mathcal{B}_k}+\frac{\mathcal{B}}{\mathcal{B}_k^*}\right). \tag{1}$$

The free energy $F(\mathcal{B}) = -\frac{1}{\mathcal{B}}\ln[Z(\mathcal{B})]$ is analytic, i.e., it has a derivative at every point, everywhere in the complex temperature plane except at the zeros of $Z(\mathcal{B})$. If the zeros are dense on lines in the complex plane, different phases are represented by different regions of holomorphy of $F(\mathcal{B})$ and are separated by these lines in the complex temperature plane. The DOZ contains the complete thermodynamic information about the system and all desired thermodynamic functions are derivable from it. The calculation of the specific heat $C_V(\mathcal{B})$ by standard differentiation yields

$$C_V(\mathcal{B}) = C_l(\mathcal{B}) - \sum_{k\in\mathbb{N}}\left[\frac{k_B\mathcal{B}^2}{(\mathcal{B}_k-\mathcal{B})^2} + \frac{k_B\mathcal{B}^2}{(\mathcal{B}_k^*-\mathcal{B})^2}\right]. \tag{2}$$

0031-9007/00/84(16)/3511(4)$15.00 © 2000 The American Physical Society

Zeros of $Z(\mathcal{B})$ are poles of $F(\mathcal{B})$ and $C_V(\mathcal{B})$. As can be seen from Eq. (2) the major contributions to the specific heat come from zeros close to the real axis, and a zero approaching the real axis infinitely close causes a divergence in the specific heat.

In the following we will give a discretized version of the classification scheme of Grossmann *et al.* [10]. To characterize the DOZ close to the real axis let us assume that the zeros lie approximately on a straight line. The crossing angle of this line with the imaginary axis (see Fig. 1) is then $\nu = \tan\gamma$ with $\gamma = (\beta_2 - \beta_1)/(\tau_2 - \tau_1)$. The crossing point of this line with the real axis is given by $\beta_{\text{cut}} = \beta_1 - \gamma\tau_1$. We define the discrete line density ϕ as a function of τ_k as the average of the inverse distances between $\mathcal{B}_k$ and its neighboring zeros

$$\phi(\tau_k) = \frac{1}{2}\left(\frac{1}{|\mathcal{B}_k - \mathcal{B}_{k-1}|} + \frac{1}{|\mathcal{B}_{k+1} - \mathcal{B}_k|}\right), \tag{3}$$

with $k = 2, 3, 4, \ldots$. Guidelined by the fact that the importance of the contribution of a zero to the specific heat decreases with increasing τ we approximate $\phi(\tau)$ in the region of small τ by a simple power law $\phi(\tau) \sim \tau^{\alpha}$. A rough estimate of α considering only the first two zeros yields

$$\alpha = \frac{\ln\phi(\tau_3) - \ln\phi(\tau_2)}{\ln\tau_3 - \ln\tau_2}. \tag{4}$$

Together with τ_1, the imaginary part of the zero closest to the real axis, the parameters γ and α classify the DOZ. As will be shown below, the parameter τ_1 is the essential parameter to classify phase transitions in small systems. For a *true* phase transition in the Ehrenfest sense we have $\tau_1 \rightarrow 0$. For this case it has been shown [10] that a phase transition is completely classified by α and γ. In the case $\alpha = 0$ and $\gamma = 0$ the specific heat $C_V(\beta)$ exhibits a δ peak corresponding to a phase transition of first order. For $0 < \alpha < 1$ and $\gamma = 0$ (or $\gamma \neq 0$) the transition is of second order. A higher order transition occurs for $1 < \alpha$ and arbitrary γ. This implies that the classification of phase transitions in finite systems by γ, α, and τ_1, which reflects the finite size effects, is a straightforward extension of the Ehrenfest scheme.

The imaginary parts τ_i of the zeros have a simple straightforward interpretation in the quantum mechanical case. By going from real temperatures $\beta = 1/(k_B T)$ to complex temperatures $\beta + i\tau/\hbar$ the quantum mechanical partition function can be written as

$$\begin{aligned} Z(\beta + i\tau/\hbar) &= \text{Tr}[\exp(-i\tau H/\hbar)\exp(-\beta H)], && (5) \\ &= \langle\Psi_{\text{can}}|\exp(-i\tau H/\hbar)|\Psi_{\text{can}}\rangle && (6) \\ &= \langle\Psi_{\text{can}}(t = 0)\,|\,\Psi_{\text{can}}(t = \tau)\rangle, \end{aligned}$$

introducing a *canonical state,* which is the sum of all eigenstates of the system appropriately weighted by the Boltzmann factor, $|\Psi_{\text{can}}\rangle = \sum_i \exp(-\beta\epsilon_i/2)|\phi_i\rangle$. Within this picture a zero of the partition function occurs at times τ_i where the overlap of a time evoluted canonical state and the initial state vanishes. This resembles a correlation time, but some care is in order here. The time τ_i is not connected to a single system, but to an ensemble of infinitely many identical systems in a heat bath, with a Boltzmann distribution of initial states. Thus, the times τ_i are those times after which the whole ensemble loses its memory.

Equation (5) is nothing but the canonical ensemble average of the time evolution operator $\exp(-i\tau H/\hbar)$. Following Boltzmann the ensemble average equals the long time average which was proven quantum mechanically by Tasaki [13]. Therefore τ_i indeed resembles times for which the long time average of the time evolution operator vanishes.

The observation of Bose-Einstein condensation in dilute gases of finite number ($\sim 10^3$–10^7) of alkali atoms in harmonic traps [14] has renewed the interest in this phenomenon which has already been predicted by Einstein [15] in 1925. The number of condensed atoms in these traps is far away from the thermodynamic limit, raising the interesting question how the order of the phase transition changes with an increasing number of atoms in the condensate. For this reason we treat the Bose-Einstein condensation in a three-dimensional isotropic harmonic trap ($\hbar = \omega = k_B = m = 1$) as an example for the application of the classification scheme given above.

For noninteracting bosons the occupation numbers of an eigenstate $|i\rangle$ and $N + 1$ particles can be evaluated by a simple recursion [16]

$$\eta_i(N + 1, \mathcal{B}) = \frac{Z_N(\mathcal{B})}{Z_{N+1}(\mathcal{B})}\exp(-\mathcal{B}\epsilon_i)[\eta_i(N, \mathcal{B}) + 1]. \tag{7}$$

Since the particle number is a conserved quantity in the canonical ensemble the direct calculation of the normalization factor can be omitted by using the relation

$$\frac{Z_N(\mathcal{B})}{Z_{N+1}(\mathcal{B})} = \frac{N + 1}{\sum_{i=0}^{\infty}\exp(-\mathcal{B}\epsilon_i)[\eta_i(N, \mathcal{B}) + 1]}. \tag{8}$$

Since $Z_N(\mathcal{B})$ is an exponentially decreasing function in β it is a difficult numerical task to calculate its zeros directly. Zeros of the partition function are reflected by poles of the ground state occupation number

$$\eta_0(N, \mathcal{B}) = -\frac{1}{\mathcal{B}}\frac{\partial_{\epsilon_0}Z_N(\mathcal{B})}{Z_N(\mathcal{B})} \tag{9}$$

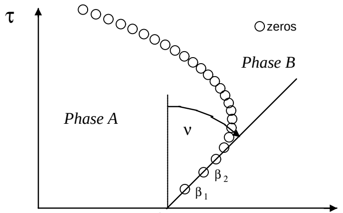

FIG. 1. Schematic plot of the DOZ illustrating the definition of the classification parameters given in the text.

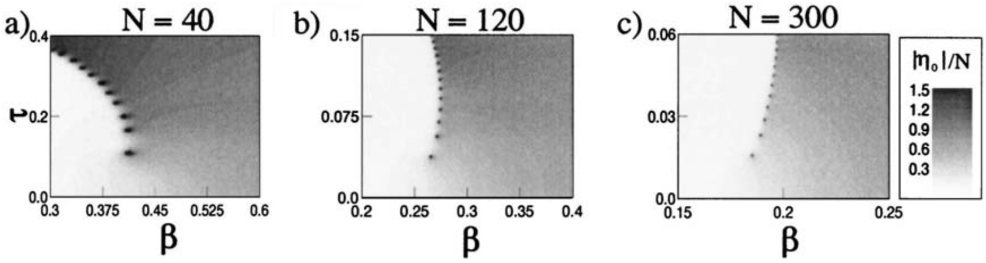

FIG. 2. Contour plots of the ground state occupation number $|\eta_0|/N$ in the complex temperature plane for 40, 120, and 300 particles in a three-dimensional isotropic trap. The black spots indicate the locations of zeros of the partition function.

evaluated at complex temperatures. Figure 2 displays contour plots of $|\eta_0(N, \mathcal{B})|/N$ for 40, 120, and 300 particles. The locations of the zeros of $Z(\mathcal{B})$ [poles of $\eta_0(N, \mathcal{B})$] are indicated by the white spots. The separation of the condensed (dark) and the normal (bright) phase is conspicuous. The zeros act like *boundary posts* between both phases. The boundary line between both phases gets more and more pronounced as the number of particles increases and the distance between neighboring zeros decreases. Figure 2 virtually displays how the phase transition approaches its thermodynamic limit. We have determined the classification parameters for the phase transition by a numerical analysis of the DOZ for up to 400 particles. The results are given in Fig. 3. The parameter α is constant at about 1.25. The small fluctuations are due to numerical errors in the determination of the location of the zeros. This value of α indicates a third order phase transition in the three-dimensional harmonic trap. Results for the two-dimensional systems and other trap geometries, which will be published elsewhere in detail, indicate that the order of the phase transition depends strongly on the trap geometry. The parameter γ and the noninteger fraction of α are related to the critical indices of the phase transition, e.g., $\gamma = 0$ indicates equal critical indices for approaching the critical temperature from the left and from the right. Regarding the finite size effects τ_1 is of major importance. As can be seen in Fig. 3(b) τ_1 is approximately proportional to $1/N$ so that the systems of bosons in a three-dimensional harmonic trap approach a true higher order phase transition linearly with increasing particle number N.

It appears that the DOZ for Bose-Einstein condensates is rather smooth. As an example for a little more complicated situation we calculated the DOZ for small Ar clusters, which have been extensively studied in the past [17]. Their thermodynamic behavior is governed by a *hopping process* between different isomers and *melting* [18]. Many indicators of *phase transitions* in Ar clusters have been investigated, e.g., the specific heat [19], the rms bond length fluctuation [20], and the onset of a $1/f$-noise behavior of the potential energy in time dependent molecular dynamics simulations [21]. However, for a good reason, all these attempts lack a definite classification of the transitions taking place in these clusters. Without going into the details of our numerical method which is based on a determination of the interaction density of states by extensive Monte Carlo simulations along with an optimized data analysis [22] we give here the results for Ar_6 and Ar_{30}. Figure 4 displays contour plots of the absolute value of the specific heat $c_V(\mathcal{B})$ in the complex temperature plane. For Ar_6 the poles lie on a straight line at $T \simeq 15$ K and are equally spaced with resulting classification parameters $\alpha = 0$, $\gamma = 0$, and $\tau_1 \hbar = 0.05$ ps. From earlier works [23] it is well known that at this temperature a hopping transition between the octahedral and the bicapped tetrahedral isomer occurs. Our classification scheme now indicates that this isomer hopping can be identified as a first order phase transition. Ar_{30} already has a tremendous number of different isomers, and a much more complicated form of the DOZ arises [see Fig. 4(b)]. The DOZ cuts the complex temperature plane into three regions with two transition lines approaching the real axis. Comparing with the literature the region below 31 K can be identified as the

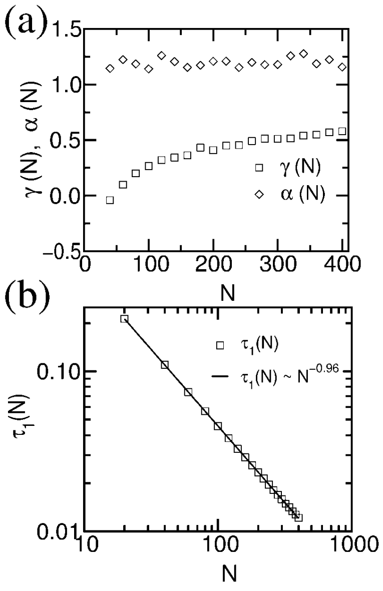

FIG. 3. Plots of the classification parameters α, γ, and τ_1 versus the number of particles for a three-dimensional harmonic trap.

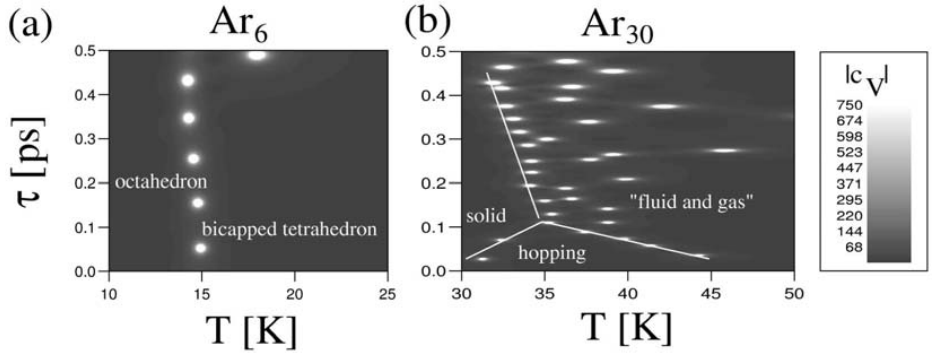

FIG. 4. Contour plots of the specific heat $|c_V|$ for Ar_6 and Ar_{30} clusters.

solid phase and the region above 45 K as a fluid phase. Because our Monte Carlo simulations are performed at zero pressure at this temperature, also the evaporation of atoms from the cluster starts which corresponds to the onset of the gas phase. The phase between these two transition lines is commonly interpreted as the melting, isomer hopping, or coexistance region. The analysis of the order of the phase transitions is quite difficult in this case and will be investigated in a more systematic study. Nevertheless the DOZ displays in a distinct manner the phase separation for Ar_{30} and can be viewed as a unique fingerprint.

In conclusion we have found that the DOZ of the canonical partition function can be used to classify phase transitions in finite systems. The DOZ of a specific system acts like a unique fingerprint. The classification scheme given above is equivalent to that given by Grossmann *et al.* but extended to the region of finite particle numbers. We have found that the zeros of the partition function act like boundary posts between different phases in the complex temperature plane. The finite size effects for the Bose-Einstein condensation are reflected by a $1/N$ dependence of the parameter τ_1 and only a slight change of the parameter α which indicates the order of the phase transition. For Ar clusters the DOZ leads to enlightening pictures of the complex process of melting or isomer hopping, identifying in a distinct manner two critical temperatures supporting an old assumption of Berry *et al.* [17]. This classification scheme developed for the canonical ensemble should also hold for other ensembles, i.e., different experimental conditions should not influence the *nature* of the systems although, e.g., the shape of the caloric curve may significantly differ.

[1] R. Berry, Nature (London) **393**, 212 (1998).
[2] M. Schmidt, B. von Issendorf, and H. Haberland, Nature (London) **393**, 238 (1998).
[3] A. Proykova and R. S. Berry, Z. Phys. D **40**, 215 (1997).
[4] O. G. Mouritsen, *Computer Studies of Phase Transitions and Critical Phenomena* (Springer-Verlag, Berlin, 1984).
[5] C. Ellert, M. Schmidt, T. Reiners, and H. Haberland, Z. Phys. D **39**, 317 (1997).
[6] P. Borrmann *et al.,* J. Chem. Phys. **111**, 10 689 (1999).
[7] D. H. E. Gross, M. E. Madjet, and O. Schapiro, Z. Phys. D **39**, 75 (1997); D. H. E. Gross, A. Ecker, and X. Z. Zhang, Ann. Phys. (Leipzig) **5**, 446 (1996).
[8] D. J. Wales and J. P. K. Doye, J. Chem. Phys. **103**, 3061 (1995).
[9] C. N. Yang and T. Lee, Phys. Rev. **97**, 404 (1952); **87**, 410 (1952).
[10] S. Grossmann and W. Rosenhauer, Z. Phys. **207**, 138 (1967); **218**, 437 (1969); S. Grossmann and V. Lehmann, Z. Phys. **218**, 449 (1969).
[11] Phase transition with respect to other thermodynamic variables can be inspected by making these quantities complex and proceeding in the same way as for the temperature.
[12] E. Titchmarsh, *The Theory of Functions* (Oxford University Press, Oxford, 1964).
[13] H. Tasaki, Phys. Rev. Lett. **80**, 1373 (1998).
[14] M. H. Anderson *et al.,* Science **269**, 198 (1995); C. C. Bradley *et al.,* Phys. Rev. Lett. **75**, 1687 (1995); K. B. Davis *et al.,* Phys. Rev. Lett. **75**, 3969 (1995).
[15] S. Bose, Z. Phys. **26**, 178 (1924); A. Einstein, Sitzungber. Preuss. Akad. Wiss. **1925**, 3 (1925).
[16] P. Borrmann and G. Franke, J. Chem. Phys. **98**, 2484 (1993); P. Borrmann, J. Harting, O. Mülken, and E. Hilf, Phys. Rev. A **60**, 1519 (1999).
[17] R. S. Berry, J. Jellinek, and G. Natanson, Phys. Rev. A **30**, 919 (1984); Chem. Phys. Lett. **107**, 227 (1984); T. Beck, J. Jellinek, and R. S. Berry, J. Chem. Phys. **87**, 545 (1987); J. Jellinek, T. L. Beck, and R. S. Berry, J. Chem. Phys. **84**, 2783 (1986).
[18] P. Labastie and R. L. Whetten, Phys. Rev. Lett. **65**, 1567 (1990); D. J. Wales and R. S. Berry, J. Chem. Phys. **92**, 4283 (1989); R. E. Kunz and R. S. Berry, Phys. Rev. E **49**, 1895 (1994).
[19] P. Borrmann, D. Gloski, and E. Hilf, Surf. Rev. Lett. **3**, 103 (1996); H. Heinze, P. Borrmann, H. Stamerjohanns, and E. Hilf, Z. Phys. D **40**, 190 (1997).
[20] P. Borrmann, Comput. Mater. Sci. **2**, 593 (1994).
[21] S. K. Nayak, R. Ramaswamy, and C. Chakravarty, Phys. Rev. E **51**, 3376 (1995).
[22] A. M. Ferrenberg and R. H. Swendsen, Phys. Rev. Lett. **63**, 1195 (1989).
[23] G. Franke, E. Hilf, and P. Borrmann, J. Chem. Phys. **98**, 3496 (1993).

3

Classification of phase transitions of finite Bose-Einstein condensates in power law traps by Fisher zeros

O. Mülken, P. Borrmann, J. Harting, and H. Stamerjohanns
Physical Review A 64, 013611 (2001)

PHYSICAL REVIEW A, VOLUME 64, 013611

Classification of phase transitions of finite Bose-Einstein condensates in power-law traps by Fisher zeros

Oliver Mülken, Peter Borrmann, Jens Harting, and Heinrich Stamerjohanns
Department of Physics, Carl von Ossietzky University Oldenburg, D-26111 Oldenburg, Germany

(Received 20 June 2000; revised manuscript received 27 November 2000; published 5 June 2001)

We present a detailed description of a classification scheme for phase transitions in finite systems based on the distribution of Fisher zeros of the canonical partition function in the complex temperature plane. We apply this scheme to finite Bose systems in power-law traps within a semi-analytic approach with a continuous one-particle density of states $\Omega(E)\sim E^{d-1}$ for different values of d and to a three-dimensional harmonically confined ideal Bose gas with discrete energy levels. Our results indicate that the order of the Bose-Einstein condensation phase transition sensitively depends on the confining potential.

DOI: 10.1103/PhysRevA.64.013611 PACS number(s): 03.75.Fi, 05.30.Jp, 05.20.−y, 64.60.−i

I. INTRODUCTION

In 1924, Bose and Einstein predicted that in a system of bosons at temperatures below a certain critical temperature T_C, the single-particle ground state is macroscopically occupied [1]. This effect is commonly referred to as Bose-Einstein condensation, and a large number of phenomena, such as the condensation phenomena in alkali-metal atoms, the superfluidity of ^{4}He, and the superconductivity, are identified as signatures of this effect. However, the physical situation is very intricate in most experiments.

Recent experiments with dilute gases of alkali-metal atoms in magnetic [2] and optical [3] traps are in some sense the best experimental approximation up to now of the ideal noninteracting Bose-Einstein system in an external power-law potential. The achievement of ultralow temperatures by laser cooling and evaporative cooling provides the opportunity to study Bose-Einstein condensation under systematic variation of adjustable external parameters, e.g., the trap geometry, the number of trapped atoms, the temperature, and by the choice of the alkali-metal atoms the effective interparticle interactions. Even in the approximation of noninteracting particles, an explanation of these experiments requires some care, because the number of bosons in these novel traps is finite and fixed and the standard grand-canonical treatment is not appropriate. The effect of the finite particle numbers on the second moments of the distribution function, e.g., the specific heat and the fluctuation of the ground-state occupation number, has been addressed in a number of publications [4,5]. In [4,6], we have presented a recursion method to calculate the canonical partition function for non-interacting bosons, and we investigated the dependency of the thermodynamic properties of the condensate on the trap geometry.

The order of the phase transition in small systems sensitively depends on finite-size effects. Compared to the macroscopic system, even for systems as simple as the three-dimensional ideal gas, the order of the phase transition might change for mesoscopic systems where the number of particles is finite or for trapped gases with different trap geometries.

In this paper, we address the classification of the phase transition of a finite number of noninteracting bosons in a power-law trap with an effective one-particle density of states $\Omega(E)=E^{d-1}$ being formally equivalent to a d-dimensional harmonic oscillator or a $2d$-dimensional ideal gas. We use a classification scheme based on the distribution of zeros of the canonical partition function initially developed by Grossman *et al.* [7] and Fisher *et al.* [8], which has been extended by us [9] as a classification scheme for finite systems. On the basis of this classification scheme, we are able to extract a qualitative difference between the order of the phase transition occurring in Bose-Einstein condensates in three-dimensional traps [10,11] and in two-dimensional traps that was recently discovered by Safonov *et al.* in a gas of hydrogen atoms absorbed on the surface of liquid helium [12]. Since we do not consider particle interactions, this difference is only due to the difference in the confining potential.

We give a detailed review of the classification scheme in Sec. II. In Sec. III, we present a method for the calculation of the canonical partition function in the complex plane and describe details of the numerical implementation. Our results for $d=1-6$ and particle numbers varying from 10 to 300 are presented in Sec. III as well as calculations for a three-dimensional parabolically confined Bose gas.

II. CLASSIFICATION SCHEME

In 1952, Yang and Lee showed that the grand-canonical partition function can be written as a function of its zeros in the complex fugacity plane, which, for systems with hard-core interactions and for the Ising model, lie on a unit circle [13].

Grossmann *et al.* [7] and Fisher [8] extended this approach to the canonical ensemble by analytic continuation of the inverse temperature to the complex plane $\beta\rightarrow\mathcal{B}=\beta+i\tau$. Within this treatment, all phenomenologically known types of phase transitions in macroscopic systems can be identified from the properties of the distribution of zeros of the canonical partition function.

In [9], we presented a classification scheme for finite systems that has its macroscopic equivalent in the scheme given by Grossmann. As usual, the canonical partition function reads

©2001 The American Physical Society

$$Z(\mathcal{B})=\int dE\,\Omega(E)\exp(-\mathcal{B}E), \tag{2.1}$$

which we write as a product $Z(\mathcal{B})=Z_{\mathrm{lim}}(\mathcal{B})Z_{\mathrm{int}}(\mathcal{B})$, where $Z_{\mathrm{lim}}(\mathcal{B})$ describes the limiting behavior of $Z(\mathcal{B})$ for $T\rightarrow\infty$, imposing that $\lim_{T\rightarrow\infty}Z_{\mathrm{int}}(\mathcal{B})=1$. This limiting partition function will only depend on the external potential applied to the system, whereas $Z_{\mathrm{int}}(\mathcal{B})$ will depend on the specific interaction between the system particles. For example, for an N-particle system in a d-dimensional harmonic trap, $Z_{\mathrm{lim}}(\mathcal{B})=\mathcal{B}^{-dN}$ and thus the zeros of $Z(\mathcal{B})$ are the same as the zeros of $Z_{\mathrm{int}}(\mathcal{B})$. Since the partition function is an integral function, the zeros $\mathcal{B}_k=\mathcal{B}^*_{-k}=\beta_k+i\tau_k(k\in\mathbb{N})$ are complex conjugate and the partition function reads

$$Z(\mathcal{B})=Z_{\mathrm{lim}}(\mathcal{B})Z_{\mathrm{int}}(0)\exp(\mathcal{B}\partial_{\mathcal{B}}\ln Z_{\mathrm{int}}(0))\times\prod_{k\in\mathbb{N}}\left(1-\frac{\mathcal{B}}{\mathcal{B}_k}\right)\left(1-\frac{\mathcal{B}}{\mathcal{B}^*_k}\right)\exp\left(\frac{\mathcal{B}}{\mathcal{B}_k}+\frac{\mathcal{B}}{\mathcal{B}^*_k}\right). \tag{2.2}$$

The zeros of $Z(\mathcal{B})$ are the poles of the Helmholtz free energy $F(\mathcal{B})=-(1/\mathcal{B})\ln Z(\mathcal{B})$, i.e. The free energy is analytic everywhere in the complex temperature plane except at the zeros of $Z(\mathcal{B})$.

Different phases are represented by regions of holomorphy that are separated by zeros lying dense on lines in the complex temperature plane. In finite systems, the zeros do not squeeze on lines, which leads to a more blurred separation of different phases. We interpret the zeros as boundary posts between two phases. The distribution of zeros contains the complete thermodynamic information about the system, and all thermodynamic properties are derivable from it. Within this picture, the interaction part of the specific heat is given by

$$C_{V,\mathrm{int}}(\mathcal{B})=-k_B\mathcal{B}^2\sum_{k\in\mathbb{N}}\left[\frac{1}{(\mathcal{B}_k-\mathcal{B})^2}+\frac{1}{(\mathcal{B}^*_k-\mathcal{B})^2}\right]. \tag{2.3}$$

The zeros of the partition function are poles of $C_V(\mathcal{B})$. As can be seen from Eq. (2.3), a zero approaching the real axis infinitely close causes a divergence at real temperature. The contribution of a zero $\mathcal{B}_k$ to the specific heat decreases with increasing imaginary part τ_k. Thus, the thermodynamic properties of a system are governed by the zeros of Z close to the real axis.

The basic idea of the classification scheme for phase transitions in small systems presented in [9] is that the distribution of zeros close to the real axis can be described approximately by three parameters, where two of them reflect the order of the phase transition and the third merely the size of the system.

We assume that the zeros lie on straight lines (see Fig. 1) with a discrete density of zeros given by

$$\phi(\tau_k)=\frac{1}{2}\left(\frac{1}{|\mathcal{B}_k-\mathcal{B}_{k-1}|}+\frac{1}{|\mathcal{B}_{k+1}-\mathcal{B}_k|}\right), \tag{2.4}$$

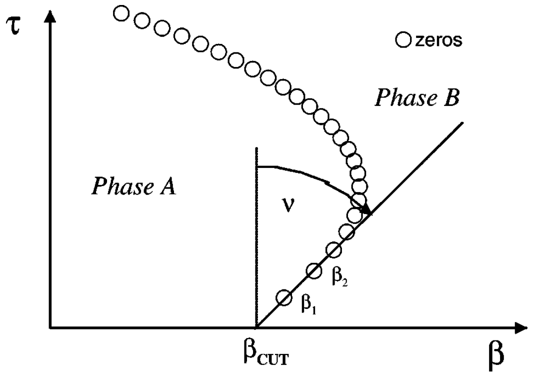

FIG. 1. Schematic illustration of the zeros in the complex temperature plane.

with $k=2,3,4,\ldots$, and we approximate for small τ the density of zeros, by a simple power law $\phi(\tau)\sim\tau^{\alpha}$. Considering only the first three zeros the exponent α can be estimated as

$$\alpha=\frac{\ln\phi(\tau_3)-\ln\phi(\tau_2)}{\ln\tau_3-\ln\tau_2}. \tag{2.5}$$

The second parameter to describe the distribution of zeros is given by $\gamma=\tan\nu\sim(\beta_2-\beta_1)/(\tau_2-\tau_1)$, where ν is the crossing angle of the line of zeros with the real axis (see Fig. 1). The *discreteness* of the system is reflected in the imaginary part τ_1 of the zero closest to the real axis.

In the thermodynamic limit, we have always $\tau_1\rightarrow 0$. In this case, the parameters α and γ coincide with those defined by Grossmann *et al* [7], who have shown how different types of phase transitions can be attributed to certain values of α and γ. They claimed that $\alpha=0$ and $\gamma=0$ correspond to a first-order phase transition, second-order transitions correspond to $0<\alpha<1$ with $\gamma=0$ or $\gamma\neq 0$, third-order transitions to $1\leqslant\alpha<2$ with arbitrary values of γ, and that all higher order phase transition correspond to $\alpha>1$. For macroscopic systems (with $\tau_1\rightarrow 0$), α cannot be smaller than zero, because this would cause a divergence of the internal energy. However, in small systems with a finite τ_1 this is possible.

In our classification scheme, we therefore define phase transitions in small systems to be of first order for $\alpha\leqslant 0$, while second- and higher-order transitions are defined in complete analogy to the Grossmann scheme augmented by the third parameter τ_1. The definition of a critical temperature β_C in small systems is crucial and ambiguous since no thermodynamic properties diverge. Thus, different definitions are possible. We define the critical temperature as $\beta_{\mathrm{cut}}=\beta_1-\gamma\tau_1$, i.e., the crossing point of the approximated line of zeros with the real temperature axis. An alternative definition is the real part of the first complex zero β_1. In the thermodynamic limit, both definitions coincide.

Comparing the specific heats calculated for different discrete distributions of zeros shows the advantages of this classification scheme. Figure 2 shows (a) three distributions of zeros lying on straight lines corresponding to a first-order transition ($\alpha=0$ and $\gamma=0$), a second-order transition (α

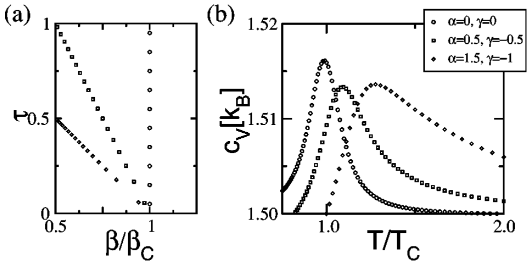

FIG. 2. Plot of (a) generated zeros lying on straight lines to simulate first- ($\alpha=0$ and $\gamma=0$), second-, ($\alpha=0.5$ and $\gamma=-0.5$), and third- ($\alpha=1.5$ and $\gamma=-1$) order phase transitions and (b) the appropriate specific heats per particle.

$=0.5$ and $\gamma=-0.5$), and a third-order phase transition ($\alpha=1.5$, and $\gamma=-1$) and (b) the pertinent specific heats. In all cases the specific heat exhibits a hump extending over a finite-temperature region and cannot be used to classify the phase transition. In contrast, even for very small systems (large τ_1), the order of the phase transition is extractable from the distribution of zeros.

The zeros of the canonical partition function have a distinct geometrical interpretation, which explains the smoothed curves of the specific heat and other thermodynamic properties in finite systems.

Figure 3 shows (a) the ground-state occupation number $|\eta_0(\mathcal{B})|/N$ in the complex temperature plane and (b) the ground-state occupation number at real temperatures for a finite ideal Bose gas of $N=120$ particles, where $\eta_0(\mathcal{B})$ is given by the derivative of the logarithm of the canonical partition function $Z(\mathcal{B})$ with respect to the ground-state energy ϵ_0, i.e., $\eta_0(\mathcal{B})=-(1/\mathcal{B})\partial_{\epsilon_0}Z(\mathcal{B})/Z(\mathcal{B})$.

Zeros of the partition function are poles of $\eta_0(\mathcal{B})$ and are indicated by dark spots, which influence the value of the ground-state occupation number at real temperatures impressively. Every pole seems to *radiate* onto the real axis and therefore determines the occupation number at real temperatures. This *radiation* extends over a broad temperature range so that the occupation number for real temperatures does not show a discontinuity but rather a smoothed curve. A closer look at Eq. (2.3) gives the mathematical explanation for this effect. The discrete distribution of zeros, i.e., $\tau_1>0$, inhibits the specific heat and all other thermodynamic properties to show a divergency at some critical temperature because the denominators of the arguments of the sum remain finite.

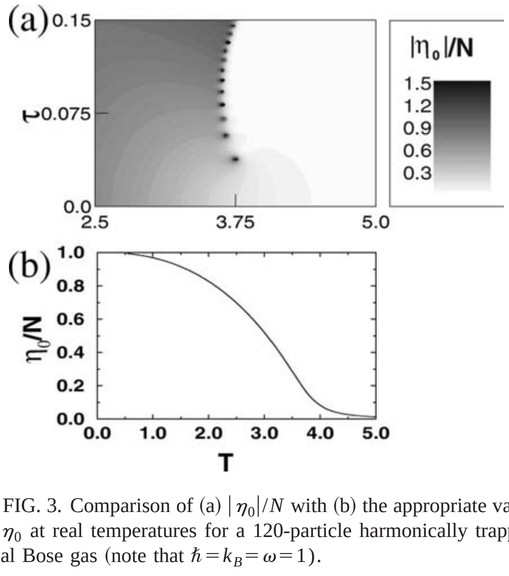

FIG. 3. Comparison of (a) $|\eta_0|/N$ with (b) the appropriate value of η_0 at real temperatures for a 120-particle harmonically trapped ideal Bose gas (note that $\hbar=k_B=\omega=1$).

Without going into a detailed analysis, we note that in the thermodynamic limit the parameter α is connected to the critical index for the specific heat by

$$C_V \sim (\beta-\beta_c)^{\alpha-1}. \tag{2.6}$$

However, since critical indices are used to describe the shape of a divergency at the critical point, an extension to small systems seems to be more or less academic.

The introduction of complex temperatures might seem artificial at first sight, but, in fact, the imaginary parts τ_k of the complex zeros $\mathcal{B}_k$ have an obvious quantum-mechanical interpretation. We write the quantum-mechanical partition function as

$$Z(\beta+i\tau/\hbar)=\mathrm{Tr}(\exp(-i\tau\hat{H}/\hbar)\exp(-\beta\hat{H})) \tag{2.7}$$

$$=\langle\Psi_{\mathrm{can}}|\exp(-i\tau\hat{H}/\hbar)|\Psi_{\mathrm{can}}\rangle \tag{2.8}$$

$$=\langle\Psi_{\mathrm{can}}(t=0)|\Psi_{\mathrm{can}}(t=\tau)\rangle, \tag{2.9}$$

introducing a *canonical state* as a sum over Boltzmann-weighted eigenstates $|\Psi_{\mathrm{can}}\rangle=\Sigma_k\exp(-\beta\epsilon_k/2)|\phi_k\rangle$. We explicitly write the imaginary part as $\tau/\hbar$ since the dimension is 1/[energy] and the imaginary part therefore can be interpreted as time. Then the imaginary parts τ_k of the zeros resemble those times for which the overlap of the initial canonical state with the time-evoluted state vanishes. However, they are not connected to a single system but to a whole ensemble of identical systems in a heat bath with an initial Boltzmann distribution.

III. BEC IN POWER-LAW TRAPS

In this section, we assume a continuous single-particle density of states $\Omega(E)=E^{d-1}$ as an approximation for a d-dimensional harmonic oscillator or a $2d$-dimensional ideal gas. For example, for the harmonic oscillator this corresponds to the limit of $\hbar\omega\rightarrow 0$ and taking only the leading term of the degeneracy of the single-particle energy levels. The one-particle partition function is given by the Laplace transformation

$$Z_1(\mathcal{B})=\int dE E^{d-1}\exp(-\mathcal{B}E)=(d-1)!\,\mathcal{B}^{-d}. \tag{3.1}$$

The canonical partition function for N noninteracting bosons can be calculated by the following recursion [6]:

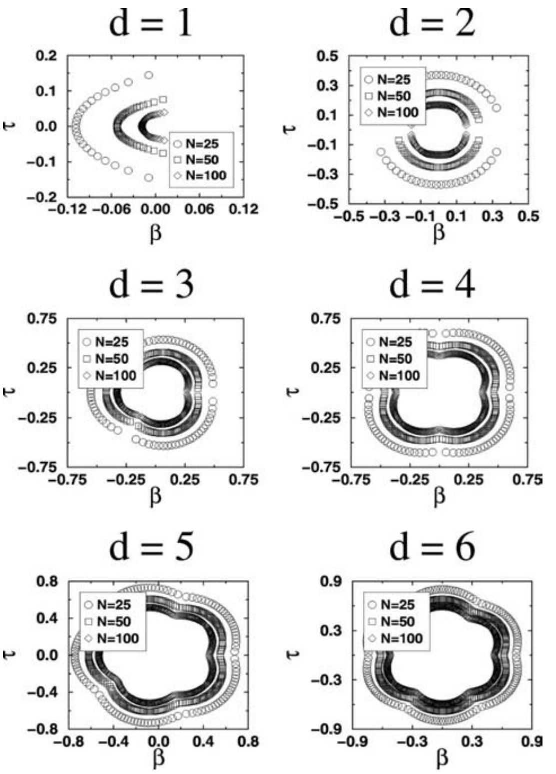

FIG. 4. Distribution of zeros for Bose-Einstein condensates with continuous one-particle density of states $\Omega(E)=E^{d-1}$ for $d=1-6$.

$$Z_N(\mathcal{B})=\frac{1}{N}\sum_{k=1}^{N} Z_1(k\mathcal{B})Z_{N-k}(\mathcal{B}), \tag{3.2}$$

where $Z_1(k\mathcal{B})=\Sigma_i\exp(-k\mathcal{B}\epsilon_i)$ is the one-particle partition function at temperature $k\mathcal{B}$ and $Z_0(\mathcal{B})=1$. For small particle numbers, this recursion works fine, even though its numerical effort grows proportional to N^2.

With Eq. (3.1) as Z_1, Eq. (3.2) leads to a polynomial of order N in $(1/\mathcal{B})^d$ for Z_N, which can be easily generated using MAPLE or MATHEMATICA. The zeros of this polynomial can be found by standard numerical methods.

Figure 4 displays the zeros of the N-particle partition function for $d=1-6$ in the complex temperature plane for particle numbers $N=25$, 50, and 100. For $d=2-6$, the zeros approach the positive real axis with increasing particle number and are shifted to higher temperatures, which is already an indicator of phase transitions. For $d=1$, the zeros approach the real axis only at negative temperature. This behavior is consistent with the usual prediction that there is no Bose-Einstein condensation for the one-dimensional harmonic oscillator and the two-dimensional ideal Bose gas [10].

The symmetry of the distributions of zeros is due to the fact that Z_N is a polynomial in $\mathcal{B}^{-d}$. For this reason, it can be inferred that for $d\rightarrow\infty$ the zeros lie on a perfect circle.

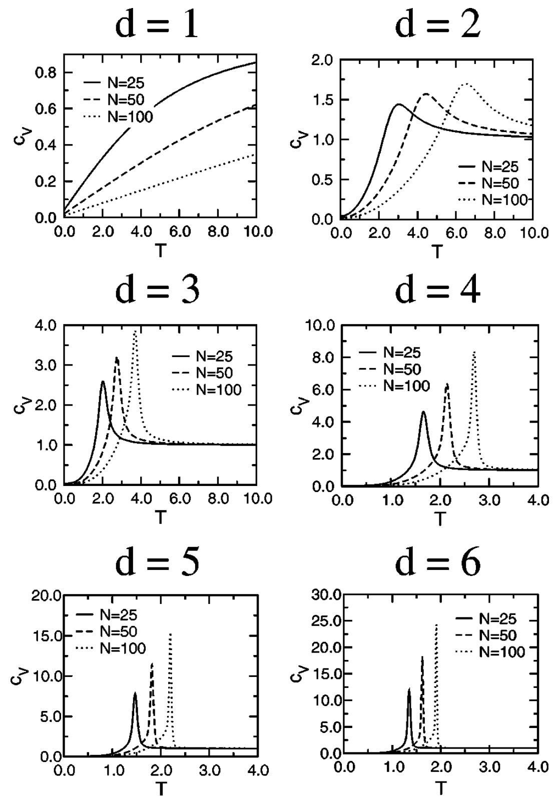

FIG. 5. Specific heat scaled by dN of Bose-Einstein condensates with continuous one-particle density of states for $d=1-6$.

Figure 5 shows the corresponding specific heats calculated using Eq. (2.3). As expected, for $d=1$ the specific heat has no hump and approaches with increasing temperature the classical value. We therefore expel the analysis of $d=1$ from the discussions below. For $d=2-6$, the specific heats show humps or peaks, which get sharper with increasing d and increasing particle number. However, from these smooth curves the orders of the phase transition cannot be deduced.

In Fig. 6, the classification parameters α,γ,τ_1 defined above are plotted for two to six dimensions and particle numbers up to $N=100$. For all values of d, the parameter α is only a slightly varying function of N and approaches very fast an almost constant value. Since α is the primary classification parameter, from Fig. 6(a) we can directly infer that the $d=2$ system exhibits a third-order phase transition ($\alpha>1$) while the transition for all higher dimensions is of second order ($0\leqslant\alpha\leqslant1$). For $N=50$, the dependence of α on d is plotted in Fig. 7(a). Since α decreases rather rapidly with increasing d, it can be speculated that systems corresponding to a large d exhibit a phase transition that is almost of first order. As mentioned above, for finite systems even values $\alpha\leqslant0$ cannot be excluded for mathematical reasons. We note that two-dimensional Bose gases are an interesting and growing field of research. As is well known, the ideal free Bose gas in two dimensions ($d=1$) does not show a phase

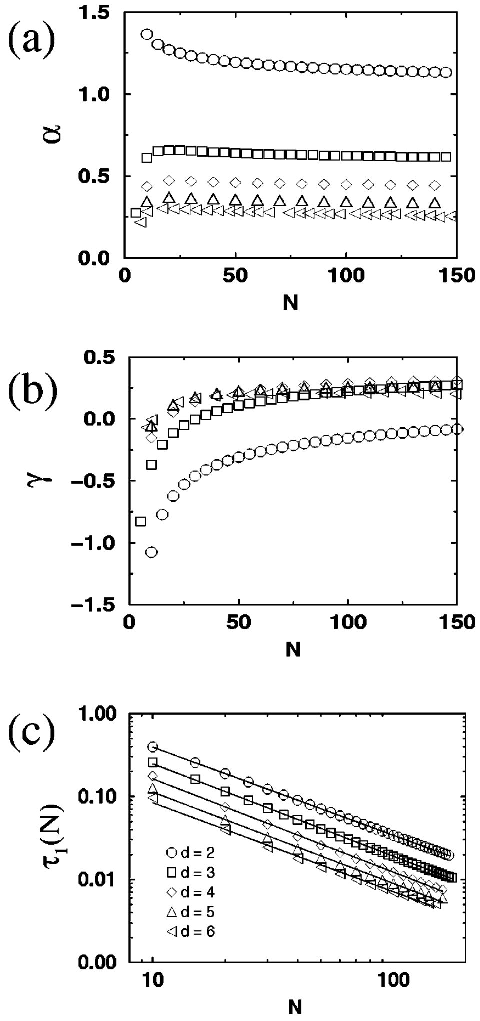

FIG. 6. Classification parameters α, γ, and τ_1 for $d=2-6$ versus particle numbers N.

transition due to thermal fluctuations that destabilize the condensate [14]. Switching on a confining potential greatly influences the properties of the gas, the thermal fluctuations are suppressed, and the gas will show Bose-Einstein condensation. Recent experiments [12] have shown that Bose-Einstein condensation is possible even though it is called a quasicondensate. In our notion, the quasicondensate is just a third-order phase transition. Thus, our results are in complete agreement with recent experiments and earlier theoretical work. An interesting question in this respect is whether the order of the transition changes for $d=2$ in the limit $N\rightarrow\infty$. Additional calculations for larger N, which are not printed in Fig. 6, indicate that α approaches 1 or might even get smaller. Note that $d=2$ is equivalent to a hypothetical four-dimensional ideal Bose gas or bosons confined in a two-dimensional parabolic trap. Our results indicate that the order of the phase transition depends sensitively on d for values around 2. This might be the reason why phase transitions in three space dimensions are sometimes classified as second- and sometimes as third-order phase transitions.

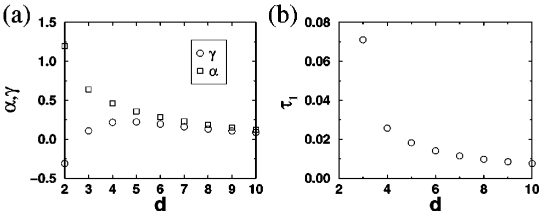

FIG. 7. Classification parameters for $N=50$ for different densities of states $\Omega(E)=E^{d-1}$ and $d=2-10$.

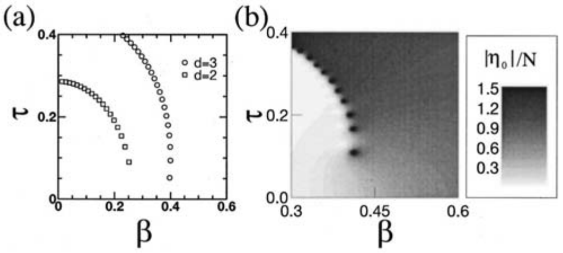

FIG. 8. Comparison between calculated zeros of the canonical partition function for three-dimensional trap geometries with (a) a continuous single-particle density of states and (b) discrete energy levels for $N=40$.

The parameter τ_1 is a measure of the finite size of the system, i.e., the scaling behavior of τ_1 as a function of N is a measure of how fast a system approaches a true nth-order phase transition in the Ehrenfest sense. The N dependence of τ_1 is displayed in Fig. 6(c). The scaling behavior can be approximated by $\tau_1 \sim N^{-\delta}$ with δ ranging between 1.06 and 1.12 for $d=2-6$.

The d dependence of the classification parameter is visualized in Fig. 7 for 50 particles. For this system size, we found $\alpha \sim d^{-4/3}$ and $\tau_1 \sim d^{-4/3}$.

The results presented above for continuous single-particle densities of states $\Omega(E)=E^{d-1}$ are obtained within semianalytical calculations. In order to compare these results to systems with a discrete level density, we adopt as a reference system the three-dimensional harmonic oscillator with the partition function given by

$$Z(\mathcal{B})=\sum_{n=0}\frac{(n+2)(n+1)}{2}\exp(-\mathcal{B}(n+3/2)), \tag{3.3}$$

with $\hbar=\omega=k_B=1$.

Figure 8(a) displays the zeros of the partition function (3.1) for $d=2$ and $d=3$. Figure 8(b) displays a contour plot of the absolute value of the ground-state occupation number $\eta_0(\mathcal{B})=-(1/\mathcal{B})\partial_{\epsilon_0}Z(\mathcal{B})/Z(\mathcal{B})$ with Z given by Eq. (3.3) calculated using an alternative recursion formula [4]. The zeros of Z are poles of η_0 and are indicated by dark spots in this figure.

Analyzing the distribution of zeros consolidates our speculation that the order of the phase transition depends sensitively on *d*. The distribution of zeros behaves like the above calculated values for $d=2$ but quantitatively like $d=3$. Since the degeneracy of the three-dimensional harmonically confined ideal Bose gas is a second-order polynomial, the quadratic term is not the only term that must be taken into account. The linear term becomes dominant for lower temperatures, so for very low temperatures the best approximation of a continuous one-particle density of states is $\Omega(E)=E$. The parameter α supports this statement [9], i.e., α resides in a region above 1, whereas the parameter γ behaves like the $d=3$ case. Finally, the parameter τ_1, which is a measure for the discreteness of the system, shows a $\tau_1 \sim N^{-0.96}$ dependence that is comparable to the one for $d=2$. Thus, for small systems the phase transition is of third order; it can be speculated whether it becomes a second-order transition in the thermodynamic limit.

Our calculations are in very good agreement with recent theoretical works, not only qualitatively but also quantitatively [15,16]. Comparing the *critical* temperature, which we defined in Sec. II, with the usually utilized temperature of the peak of the specific heat $\beta(C_{V,\max})$ or the grand canonically calculated $T_C \sim N^{1/3}$ confirms our approach. In Fig. 9, three possible definitions of the critical temperature are given that all coincide in the thermodynamic limit. All definitions show a $\beta \sim N^{-\rho}$ dependence with ρ ranging between $\frac{2}{5}$ and $\frac{1}{3}$.

IV. CONCLUSION

Starting with the old ideas of Yang and Lee and Grossmann *et al.*, we have developed a classification scheme for phase transitions in finite systems. Based on the analytic continuation of the inverse temperature β into the complex plane, we have shown the advantages of this approach. The distribution of the so-called Fisher zeros $\mathcal{B}_k$ draws enlightening pictures even for small systems, whereas the usually referred to thermodynamic properties such as the specific heat fail to classify the phase transitions properly. The classification scheme presented in this paper enables us to name the order of the transition in a nonambiguous way. The complex parts τ_k of the zeros $\mathcal{B}_k$ resemble times for which a whole ensemble of identical systems under consideration in a heat bath with an initial Boltzmann distribution loses its memory.

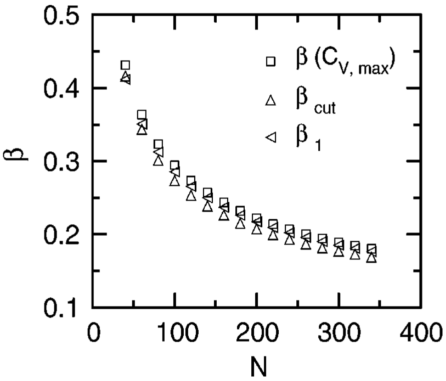

FIG. 9. Comparison between three different approaches to define a critical temperature for phase transitions in finite systems.

We have applied this to ideal noninteracting Bose gases confined in power-law traps. We have found that the order of the phase transition sensitively depends on the single-particle density of states generated by the confining potential. The distribution of zeros exactly reveals the order of the phase transition in finite systems.

---

[1] S. Bose, Z. Phys. **26**, 178 (1924); A. Einstein, Sitzungsber. K. Preuss. Akad. Wiss. **1925**, 3 (1925).

[2] M. H. Anderson, J. R. Ensher, M. R. Matthews, C. E. Wieman, and E. A. Cornell, Science **269**, 198 (1995); C. C. Bradley, C. A. Sackett, J. J. Tollett, and R. G. Hulet, Phys. Rev. Lett. **75**, 1687 (1995); K. B. Davis, M.-O. Mewes, M. R. Andrews, N. J. van Druten, D. S. Durfee, D. M. Kurn, and W. Ketterle, *ibid.* **75**, 3969 (1995).

[3] D. Stamper-Kurn, M. R. Andrews, A. P. Chikkatur, S. Inouye, H.-J. Miesner, J. Stenger, and W. Ketterle, Phys. Rev. Lett. **80**, 2027 (1998).

[4] P. Borrmann, J. Harting, O. Mülken, and E. Hilf, Phys. Rev. A **60**, 1519 (1999).

[5] S. Grossmann and M. Holthaus, Phys. Rev. Lett. **79**, 3557 (1997); S. Grossmann and M. Holthaus, Opt. Express **1**, 262 (1997); P. Navez *et al.*, Phys. Rev. Lett. **79**, 1789 (1997); M. Gajda and K. Razazewski, *ibid.* **78**, 2686 (1997).

[6] P. Borrmann and G. Franke, J. Chem. Phys. **98**, 2484 (1993).

[7] S. Grossmann and W. Rosenhauer, Z. Phys. **207**, 138 (1967); **218**, 437 (1969); S. Grossmann and W. Rosenhauer, *ibid.* **218**, 449 (1969).

[8] M. E. Fisher, in *Lectures in Theoretical Physics*, edited by W. E. Brittin (University of Colorado Press, Boulder, 1965), Vol. 7c.

[9] P. Borrmann, O. Mülken, and J. Harting, Phys. Rev. Lett. **84**, 3511 (2000).

[10] V. Bagnato and D. Kleppner, Phys. Rev. A **44**, 7439 (1991).

[11] H. Perez Rojas, Phys. Lett. A **234**, 13 (1997); S. Pearson, T. Pang, and C. Chen, Phys. Rev. A **58**, 4811 (1998); Z. Yan, *ibid.* **59**, 4657 (1999).

[12] A. I. Safonov *et al.*, Phys. Rev. Lett. **81**, 4545 (1998).

[13] C. N. Yang and T. Lee, Phys. Rev. **97**, 404 (1952); **87**, 410 (1952).

[14] W. J. Mullin, J. Low Temp. Phys. **106**, 1405 (1997); **110**, 167 (1997); F. Dalfovo, S. Giorgini, L. P. Pitaevskii, and S. Stringari, Rev. Mod. Phys. **71**, 463 (1999).

[15] N. L. Balazs and T. Bergeman, Phys. Rev. A **58**, 2359 (1998).

[16] S. Grossmann and M. Holthaus, Z. Naturforsch. A. Phys. Sci. **50**, 921 (1995).

Bibliography

[1] I.V. Abarenkov and V. Heine. Phil. Mag., **12**, 529, 1965. ➪58

[2] K.H. Ahn and P. Fulde. *Parity effects in stacked nanoscopic quantum rings*. Phys. Rev. B, **62** (8), 4813, 2000. ➪42

[3] N. Akman and M. Tomak. *Interacting electrons in a 2D quantum dot*. Physica B: Condensed Matter, **262**, 317, 1999. ➪14

[4] I.L. Aleiner, P.W. Brouwer, and L.I. Glazman. *Quantum effects in coulomb blockade*. arXiv:cond-mat, 0103008, 2001. To appear in *Phys. Reports*. ➪14

[5] Y. Alhassid. *The statistical theory of quantum dots*. Rev. Mod. Phys., **72** (4), 895, 2000. ➪14

[6] M.H. Anderson, J.R. Ensher, M.R. Matthews, C.E. Wieman, and E.A. Cornell. *Observation of Bose-Einstein condensation in a dilute atomic vapor*. Science, **269**, 198, 1995. ➪68, 74, 80

[7] M.S. Anderson and C.A. Swenson. *Experimental compressions for sodium, potassium, and rubidium metals to 20 kbar from 4.2 to 300 K.* Phys. Rev. B, **28** (10), 5395, 1983. ➪58

[8] N.W. Ashcroft and N.D. Mermin. *Solid state physics*. Saunders College Publishing, 3rd edition, 1976. ➪58

[9] R.C. Ashoori. *Electrons in artificial atoms*. Nature, **379**, 413, 1996. ➪12

[10] R.C. Ashoori, H.L. Störmer, J.S. Weiner, L.N. Pfeiffer, S.J. Pearton, K.W. Baldwin, and K.W. West. *Single-electron capacitance spectroscopy of discrete quantum levels*. Phys. Rev. Lett., **68** (20), 3088, 1992. ➪10

[11] V. Bagnato and D. Kleppner. *Bose-Einstein condensation in low-dimensional traps*. Phys. Rev. A, **44** (11), 7439, 1991. ➪80

[12] N.L. Balazs and T. Bergeman. *Statistical mechanics of ideal Bose atoms in a harmonic trap*. Phys. Rev. A, **58** (3), 2359, 1998. ➪80

[13] J. Barker. *A quantum-statistical Monte Carlo method; path integrals with boundary conditions*. J. Chem. Phys., **70** (6), 2914, 1979. ➪25

[14] R.N. Barnett, C.L. Cleveland, H. Häkkinen, C. Yannouleas, and U. Landman. *Structures and spectra of gold nanoclusters and quantum dot molecules*. Eur. Phys. J. D, **9**, 95, 1999. ➪47

[15] T. Beck, J. Jellinek, and R.S. Berry. *Rare gas clusters: Solids, liquids, slush, and magic numbers*. J. Chem. Phys., **87**, 545, 1987. ➪74

[16] R.S. Berry. *Size is everything*. Nature, **393**, 212, 1998. ➪74

[17] R.S. Berry, J. Jellinek, and G. Natanson. *Melting of clusters and melting*. Phys. Rev. A, **30** (2), 919, 1984. ➪74

[18] R.S. Berry, J. Jellinek, and G. Natanson. *Unequal freezing and melting temperatures for clusters*. Chem. Phys. Lett., **107**, 227, 1984. ➪74

[19] K. Binder and D.W. Heermann. *Monte Carlo simulation in statistical physics*. Springer-Verlag, 3rd edition, 1997. ➪21

[20] K. Binder (Ed.). *Applications of the Monte Carlo method in statistical physics*. Springer-Verlag, 1992. ➪21

[21] K. Binder (Ed.). *The Monte Carlo method in condensed matter physics*. Springer-Verlag, 2nd edition, 1992. ➪21

[22] R. Blick. *Künstliche Atome und Moleküle: Gekoppelte Quantenpunkte und Mikrowellenspektroskopie an Quantenpunkten*. Verlag Harri Deutsch, 1996. Reihe Physik Bd. 57. ➪10

[23] Bonacic-Koutecky, I. Boustani, M. Guest, and J. Koutecky. *Ab initio configuration interaction study of the electronic and geometric structures of small sodium cationic clusters*. J. Chem. Phys., **89** (8), 4861, 1988. ➪59, 60

[24] Bonacic-Koutecky, P. Fantucci, and J. Koutecky. *Systematic ab initio configuration-interaction study of alkali-metal clusters. II. Relation between electronic structure and geometry of small sodium clusters*. Phys. Rev. B, **37** (9), 4369, 1988. ➪57, 59, 60

[25] V. Bonacic-Koutecky, J. Pittner, C. Fuchs, P. Fantucci, M.F. Guest, and J. Koutecky. *Ab initio predictions of structural and optical response properties of* Na_n^+ *clusters: Interpretation of depletion spectra at low temperature*. J. Chem. Phys., **104** (4), 1427, 1996. ➪57, 59, 60, 62, 63

[26] P. Borrmann. *How should thermodynamics for small systems be done?* Computational Materials Science, **2**, 593, 1994. ➪74

[27] P. Borrmann. *Pfadintegrale und Cluster*. PhD thesis, C.v.O. Universität Oldenburg, 1995. ➪20

[28] P. Borrmann and G. Franke. *Recursion formulas for quantum statistical partition functions*. J. Chem. Phys., **98** (3), 1993. ➪68, 74, 80, 107

[29] P. Borrmann, D. Gloski, and E.R. Hilf. *Specific heat in the thermodynamics of clusters*. Surface Review and Letters, **3**, 103, 1996. ➪74

[30] P. Borrmann and J. Harting. *Order-disorder transition in nanoscopic semiconductor quantum rings*. Phys. Rev. Lett., **86** (14), 3120, 2001. ➪2, 23, 28, 42

[31] P. Borrmann, J. Harting, O. Mülken, and E.R. Hilf. *Calculation of thermodynamic properties of finite Bose-Einstein systems*. Phys. Rev. A, **60** (2), 1519, 1999. ➪3, 68, 74, 80

[32] P. Borrmann and E.R. Hilf. *Structure and stability of polarized* $Li^3He_n^+$ *ions*. Z. Phys. D, **26**, 350, 1993. ➪36, 42

[33] P. Borrmann and E.R. Hilf. *New enhancements to Feynmans path integral for fermions*. arXiv:cond-mat, 9412113, 1994. ➪22, 24

[34] P. Borrmann, O. Mülken, and J. Harting. *Classification of phase transitions in small systems*. Phys. Rev. Lett., **84** (16), 3511, 2000. ➪4, 74, 80

[35] P. Borrmann, H. Stamerjohanns, E.R. Hilf, P. Jund, S.G. Kim, and Tománek D. *Thermodynamics of finite magnetic two-isomer systems*. J. Chem. Phys., **111** (23), 10689, 1999. ➪74

[36] S.N. Bose. *Plancks Gesetz und Lichtquantenhypothese*. Z. Phys., **26**, 178, 1924. ➪74, 80

[37] M. Brack. *The physics of simple metal clusters: Self-consistent jellium model and semiclassical approaches*. Rev. Mod. Phys., **65** (3), 677, 1993. ➪57

[38] C.C. Bradley, C.A. Sackett, J.J. Tollett, and R.G. Hulet. *Evidence of Bose-Einstein condensation in an atomic gas with attractive interactions*. Phys. Rev. Lett., **75** (9), 1687, 1995. ➪68, 74, 80

[39] K. Brunner, U. Bockelmann, G. Abstreiter, M. Walther, G. Böhm, G. Tränkle, and G. Weimann. *Photoluminescence from a single GaAs/AlGaAs quantum dot*. Phys. Rev. Lett., **69** (22), 3216, 1992. ➪11

[40] F. Calvayrac, P.G. Reinhard, and E. Suraud. *Dynamics of sodium clusters in a nonadiabatic electron-ion model*. Eur. Phys. J. D, **9**, 389, 1999. ➪57

[41] J. Cao and B. Berne. *On energy estimators in path integral Monte Carlo simulations: Dependence of accuracy on algorithm*. J. Chem. Phys., **91** (10), 6359, 1989. ➪25

[42] D.M. Ceperley. *Ground state of the fermion one-component plasma: A Monte Carlo study in two and three dimensions*. Phys. Rev. B, **18** (7), 3126, 1978. ➪15

[43] D.M. Ceperley. *Path-integral calculations of normal liquid* ^3He. Phys. Rev. Lett., **69** (2), 331, 1992. ➪23, 36

[44] D.M. Ceperley. *Path integrals in the theory of condensed helium*. Rev. Mod. Phys., **67** (2), 279, 1995. ⇨19, 24, 28

[45] D.M. Ceperley and B.J. Alder. *Ground state of the electron gas by a stochastic method*. Phys. Rev. Lett., **45** (7), 566, 1980. ⇨15

[46] T. Chakraborty and P. Pietiläinen. *Electron-electron interaction and the persistent current in a quantum ring*. Phys. Rev. B, **50** (12), 8460, 1994. ⇨42

[47] L.L. Chang, L. Esaki, and R. Tsu. *Resonant tunneling in semiconductor double barriers*. Appl. Phys. Lett., **24**, 593, 1974. ⇨7

[48] A. Cho. *Film deposition by molecular beam techniques*. J. Vac. Sci. Tech., **8**, S31, 1971. ⇨9

[49] A. Cho and J. Arthur. *Molecular beam epitaxy*. Prog. Solid-State Chem., **10**, 157, 1975. ⇨9

[50] J. Cibert, P.M. Petroff, G.J. Dolan, S.J. Pearton, A.C. Gossard, and J.H. English. *Optically detected carrier confinement to one and zero dimension in GaAs quantum well wires and boxes*. Appl. Phys. Lett., **49**, 1275, 1986. ⇨7

[51] F. Dalfovo, S. Giorgini, L.P. Pitaevski, and S. Stringari. *Theory of Bose-Einstein condensation in trapped gases*. Rev. Mod. Phys., **71** (3), 463, 1999. ⇨80

[52] K.B. Davis, M.-O. Mewes, M.R. Andrews, N.J. van Druten, D.S. Durfee, D.M. Kurn, and W. Ketterle. *Bose-Einstein condensation in a gas of sodium atoms*. Phys. Rev. Lett., **75** (22), 3969, 1995. ⇨68, 74, 80

[53] H. De Raedt and A. Lagendijk. *Monte Carlo calculation of the thermodynamic properties of a quantum model: A one-dimensional fermion lattice model*. Phys. Rev. Lett., **46** (2), 77, 1981. ⇨19, 20

[54] R. Dingle, W. Wiegmann, and C.H. Henry. *Quantum states of confined carriers in very thin* $Al_xGa_{1-x}As$-*GaAs*-$Al_xGa_{1-x}As$ *heterostructures*. Phys. Rev. Lett., **33**, 827, 1974. ⇨7

[55] P.A.M. Dirac. *The lagrangian in quantum mechanics*. Phys. Z. Sow., **3** (64), 1933. ⇨17

[56] P.A.M. Dirac. *The principles of quantum mechanics*. Oxford University Press, 1933. ⇨17

[57] P.A.M. Dirac. *On the analogy between classical and quantum mechanics*. Rev. Mod. Phys., **17** (2–3), 195, 1945. ⇨17

[58] R. Egger, W. Häusler, C.H. Mak, and H. Grabert. *Crossover from Fermi liquid to Wigner molecule behavior in quantum dots*. Phys. Rev. Lett., **82** (16), 3320, 1999. ⇨14, 32, 36

[59] D.M. Eigler and E.K. Schweitzer. *Positioning single atoms with a scanning tunnelling microscope*. Nature, **344**, 524, 1990. ➪1

[60] A. Einstein. *Quantentheorie des einatomigen idealen Gases: Zweite Abhandlung*. Sitzungsbericht der Preussischen Akademie der Wissenschaft, **18**, 1925. ➪74, 80

[61] W. Ekardt. *Dynamical polarizability of small metal particles: Self-consistent spherical jellium background model*. Phys. Rev. Lett., **52** (21), 1925, 1984. ➪57

[62] W. Ekardt. *Work function of small metal particles: Self-consistent spherical jellium background model*. Phys. Rev. B, **29** (4), 1558, 1984. ➪57

[63] A. Ekert, P.M. Hayden, and H. Inamori. *Basic concepts in quantum computation*. In R. Kaiser, C. Westbrook, and F. David (editors), *Coherent atomic matter waves, Les Houches session LXXII*. Springer-Verlag, 2000. ➪47

[64] A.I. Ekimov, A.L. Efros, and A.A. Onushenko. *Quantum size effect in semiconductor microcrystals*. Solid Sate Commun., **56**, 921, 1985. ➪10

[65] C. Ellert, M. Schmidt, T. Reiners, and H. Haberland. *Transition of the electronic response from molecular-like to jellium-like in cold, small sodium clusters*. Z. Phys. D, **39**, 317, 1997. ➪57, 74

[66] A. Emperador, M. Barranco, E. Lipparini, M. Pi, and L. Serra. *Density-functional calculations of magnetoplasmons in quantum rings*. Phys. Rev. B, **59** (23), 15301, 1999. ➪42

[67] J. Faist, F. Capasso, C. Sirtori, D.L. Sivco, A.L. Hutchinson, M.S. Hybertsen, S.N.G. Chu, and A.Y. Cho. *Quantum cascade lasers without intersubband population inversion*. Phys. Rev. Lett., **76** (3), 411, 1996. ➪8

[68] A.M. Ferrenberg and R.H. Swendsen. *Optimized Monte Carlo data analysis*. Phys. Rev. Lett., **63** (12), 1195, 1989. ➪74

[69] R.P. Feynman. *Space-time approach to non-relativistic quantum mechanics*. Rev. Mod. Phys., **20** (2), 367, 1948. ➪17, 20

[70] R.P. Feynman. *There is plenty of room at the bottom*. Caltech Engineering and Sience, 1960. Talk given on 12/29/1959 at the annual APS meeting. ➪17

[71] R.P. Feynman and A.R. Hibbs. *Quantum mechanics and path integrals*. McGraw-Hill Book Company, 1965. ➪17, 23

[72] M.E. Fischer. *The nature of critical points*. Lectures in theoretical physics, **7c**, 1965. ➪80

[73] V. Fock. *Näherungsmethoden zur Lösung des quantenmechanischen Mehrkörperproblems*. Z. Phys., **61**, 126, 1930. ➪14

[74] J.A. Folk, S.R. Patel, S.F. Godijn, A.G. Huibers, S.M. Cronenwett, and C.M. Marcus. *Statistics and parametric correlations of Coulomb blockade peak fluctuations in quantum dots*. Phys. Rev. Lett., **76** (10), 1699, 1996. ➪10

[75] W.M.C. Foulkes, L. Mitas, R.J. Needs, and G. Rajagopal. *Quantum Monte Carlo simulations of solids*. Rev. Mod. Phys., **73** (1), 33, 2001. ➪23

[76] G. Franke, E.R. Hilf, and P. Borrmann. *The structure of small clusters: Multiple normal-modes model*. J. Chem. Phys., **98**, 3496, 1993. ➪74

[77] M. Fujito, A. Natori, and H. Yasunaga. *Many-electron ground states in anisotropic parabolic quantum dots*. Phys. Rev. B, **53** (15), 9952, 1996. ➪14

[78] T. Fukui, S. Ando, and Y. Tokura. *GaAs tetrahedral quantum dot structures fabricated using selective area metalorganic chemical vapor deposition*. Appl. Phys. Lett., **58**, 2018, 1991. ➪11

[79] M. Gajda and K. Rzazewski. *Fluctuations of Bose-Einstein condensate*. Phys. Rev. Lett., **78** (14), 2686, 1997. ➪68

[80] A. Giansanti and G. Jacucci. *Variance and correlation length of energy estimators in Metropolis path integral Monte Carlo*. J. Chem. Phys., **89** (12), 7454, 1988. ➪25, 36

[81] S.M. Girvin and T. Jach. *Interacting electrons in two-dimensional Landau levels: Results for small clusters*. Phys. Rev. B, **28** (8), 4506, 1983. ➪14

[82] S. Grossmann and M. Holthaus. *λ-transition to the Bose-Einstein condensate*. Z. Naturforsch., **50a**, 921, 1995. ➪80

[83] S. Grossmann and M. Holthaus. *Fluctuations of the particle number in a trapped Bose-Einstein condensate*. Phys. Rev. Lett., **79** (19), 3557, 1997. ➪68, 80

[84] S. Grossmann and M. Holthaus. *Maxwell's demon at work: Two types of Bose condensate fluctuations in power-law traps*. Optics Express 262, **1** (10), 1997. ➪68, 80

[85] S. Grossmann and V. Lehmann. *Phase transition and the distribution of temperature zeros of the partition function, II. Applications and examples*. Z. Phys., **218**, 449, 1969. ➪4, 74, 80

[86] S. Grossmann and W. Rosenhauer. *Temperature dependence near phase transition*. Z. Phys., **207**, 138, 1967. ➪4, 74, 80

[87] S. Grossmann and W. Rosenhauer. *Phase transition and the distribution of temperature zeros of the partition function, I. General relations*. Z. Phys., **218**, 437, 1969. ➪4, 74, 80

[88] H.L. Grubin, K. Hess, G.J. Iafrate, and D.K. Ferry. *The physics Of submicron structures*. Plenum Press, 1984. ➪1

[89] J. Guan, M.E. Casida, A.M. Köster, and D.R. Salahub. *All-electron local and gradient-corrected density-functional calculations of Na$_n$ dipole polarizabilities for n=1–6*. Phys. Rev. B, **52** (3), 1995. ➪57

[90] R. Gutiérrez, F. Grossmann, O. Knospe, and R. Schmidt. *Electrical transport properties of small sodium clusters*. Phys. Rev. A, **64**, 013202, 2001. ➪57

[91] H. Haberland. *Melting of Clusters*. In C. Guet and F. David (editors), *Atomic Clusters and Nanoparticles, Les Houches Session LXXIII*. Springer-Verlag, 2001. In press. ➪64

[92] H. Häkkinen and M. Manninen. *How "magic" is a magic metal cluster?* Phys. Rev. Lett., **76** (10), 1599, 1996. ➪57

[93] V. Halonen, P. Pietiläinen, and T. Chakraborty. *Optical-absorption spectra of quantum dots and rings with a repulsive scattering centre*. Europhys. Lett., **33** (5), 377, 1996. ➪42

[94] P. Harrision. *Quantum wells, wires and dots – theoretical and computational physics*. John Wiley & Sons, Inc., 1999. ➪14

[95] J. Harting. *Bose-Einstein Kondensation in magnetischen und optischen Fallen*. Master's thesis, C.v.O. Universität Oldenburg, 1999. ➪3

[96] J. Harting, O. Mülken, and P. Borrmann. *The interplay between shell effects and electron correlation in quantum dots*. Phys. Rev. B, **62** (15), 10207, 2000. ➪2, 24, 36, 42

[97] D.R. Hartree. *The wave mechanics of an atom with a non-coulomb central field. Part I. Theory and methods*. Proc. Camb. Phil. Soc., **24**, 89, 1928. ➪14

[98] D.R. Hartree. *The wave mechanics of an atom with a non-coulomb central field. Part II. Some results and discussion*. Proc. Camb. Phil. Soc., **24**, 89, 1928. ➪14

[99] P. Hawrylak. *Single-electron capacitance spectroscopy of few-electron artificial atoms in a magnetic field: Theory and experiment*. Phys. Rev. Lett., **71** (20), 3347, 1993. ➪14, 47

[100] W.A. de Heer. *The physics of simple metal clusters: Experimental aspects and simple models*. Rev. Mod. Phys., **65** (3), 611, 1993. ➪57

[101] H.H. Heinze. *Die Permanente im thermodynamischen Viel-Bosonen-Pfadintegral sowie die Bestimmung von Phasenenübergängen aus experimentellen Streuspektren atomarer Cluster*. Master's thesis, C.v.O. Universität Oldenburg, 1996. ➪24, 25

[102] H.H. Heinze, P. Borrmann, H. Stamerjohanns, and E.R. Hilf. *Temperature measurement from scattering spectra of clusters: Theoretical treatment*. Z. Phys. D, **40**, 190, 1997. ➪25, 36, 74

[103] D. Heitmann and J.P. Kotthaus. *The spectroscopy of quantum dot arrays*. Physics Today, **46**, 56, 1993. ➩12

[104] Carl Hepburn. *Britney's guide to semiconductor physics*. http://www.britneyspears.ac/lasers.html, 2000. ➩14

[105] H.F. Herman, E.J. Bruskin, and B.J. Berne. *On path integral Monte Carlo simulations*. J. Chem. Phys., **76** (10), 5150, 1982. ➩25

[106] K. Hirose and N.S. Wingreen. *Spin-density-functional theory of circular and elliptical quantum dots*. Phys. Rev. B, **59** (7), 4604, 1999. ➩15, 16, 36, 42, 48

[107] J.E. Hirsch, R.L. Sugar, D.J. Scalapino, and R. Blankenbecler. *Monte Carlo simulations of one-dimensional fermion systems*. Phys. Rev. B, **26** (9), 5033, 1982. ➩23

[108] J. O. Hirschfelder. *Classical and quantum mechanical hypervirial theorems*. J. Chem. Phys., **33** (5), 1462, 1960. ➩25

[109] F. Hofmann, T. Heinzel, D.A. Wharam, J.P. Kotthaus, G. Böhm, W. Klein, G. Tränkle, and G. Weimann. *Single electron switching in a parallel quantum dot*. Phys. Rev. B, **51** (19), 13872, 1995. ➩47

[110] P. Hohenberg and W. Kohn. *Inhomogeneous electron gas*. Phys. Rev., **136** (3b), B864, 1964. ➩15

[111] A. Imamoglu, D.D. Awschalom, G. Burkard, D.P. DiVincenzo, D. Loss, M. Sherwin, and A. Small. *Quantum information processing using quantum dot spins and cavity QED*. Phys. Rev. Lett., **83** (20), 4204, 1999. ➩47

[112] L. Jacak, P. Hawrylak, and A. Wojs. *Quantum Dots*. Springer-Verlag, 1998. ➩7, 9, 14

[113] J. Jellinek, T.L. Beck, and R.S. Berry. *Solid-liquid phase changes in simulated isoenergetic Ar13*. J. Chem. Phys., **84**, 2783, 1986. ➩74

[114] N.F. Johnson. *Quantum dots: few-body, low-dimensional systems*. Journal of Physics: Condensed Matter, **7**, 966, 1995. ➩14

[115] M. Kac. *On distribution of certain Wiener functionals*. Trans. Math. Soc. Am., **65**, 1, 1949. ➩20

[116] M. Kac. *Probability and related topics in physical science*. Wiley-Interscience, 1959. ➩20

[117] M.H. Kalos (Ed.). *Monte Carlo methods in quantum problems*. D. Reidel Publishing Company, 1982. ➩21

[118] K. Kash, A. Scherer, J.M. Worlock, H.G. Craighead, and M.C. Tamargo. *Optical spectroscopy of ultrasmall structures etched from quantum wells*. Appl. Phys. Lett., **49**, 1043, 1986. ➩7

[119] M.A. Kastner. *The single-electron transistor*. Rev. Mod. Phys., **64** (3), 849, 1992. ➪47

[120] M.A. Kastner. *Artificial atoms*. Physics Today, **46** (1), 24, 1993. ➪12

[121] R.F. Kazarinov and R.A. Suris. *Possibility of the amplification of electromagnetic waves in a semiconductor with a superlattice*. Fiz. Tech. Poluprovodn., **5** (4), 797, 1971. ➪8

[122] U.F. Keyser, H.W. Schumacher, U. Zeitler, and R.J. Haug. *Fabrication of a single-electron transistor by current-controlled local oxidation of a two-dimensional electron system*. Appl. Phys. Lett., **76** (4), 457, 2000. ➪47

[123] H. Kleinert. *Pfadintegrale in Quantenmechanik, Statistik und Polymerphysik*. BI Wissenschaftsverlag, 1993. ➪19

[124] K. v. Klitzing, G. Dorda, and M. Pepper. *New method for high-accuracy determination of the fine-structure constant based on quantized hall resistance*. Phys. Rev. Lett., **45** (6), 494, 1980. ➪7

[125] W.D. Knight, K. Clemenger, W.A. de Heer, W.A. Saunders, Y.M. Chou, and M.L. Cohen. *Electronic shell structure and abundances of sodium clusters*. Phys. Rev. Lett., **52** (24), 2141, 1984. ➪57

[126] W. Kohn. *An essay on condensed matter physics in the twentieth century*. Rev. Mod. Phys., **71** (2), S59, 1999. ➪15

[127] W. Kohn. *Nobel lecture: Electronic structure of matter-wave functions and density functionals*. Rev. Mod. Phys., **71** (5), 1253, 1999. ➪15

[128] W. Kohn and L.J. Sham. *Self consistent equations including exchange and correlation effects*. Phys. Rev., **140** (4a), A1133, 1965. ➪15

[129] J. Kolehmainen, S.M. Reimann, M. Koskinen, and M. Manninen. *Magnetic interaction between coupled quantum dots*. Eur. Phys. J. B, **13** (4), 731, 2000. ➪47

[130] H. Kono, A. Takasaka, and S.H. Lin. *Monte Carlo calculation of the quantum partition function via path integral*. J. Chem. Phys., **88** (10), 6390, 1988. ➪20, 36

[131] M. Koskinen, M. Manninen, B. Mottelson, and S.M. Reimann. *Rotational and vibrational spectra of quantum rings*. arXiv:cond-mat, 004095, 2000. ➪15, 42

[132] M. Koskinen, M. Manninen, and S.M. Reimann. *Hund's rule and spin density waves in quantum dots*. Phys. Rev. Lett., **79** (7), 1389, 1997. ➪15, 16, 42

[133] L.P. Kouwenhoven, D.G. Austing, and S. Tarucha. *Few-electron quantum dots*. Rep. Prog. Phys., **64**, 701, 2000. ➪9, 10, 13, 14

[134] L.P. Kouwenhoven, C.M. Marcus, P.L. McEuen, S. Tarucha, R.M. Westervelt, and N.S. Wingreen. *Electron transport in quantum dots*. Proceedings of the NATO advanced study institute on mesoscopic electron transport, Kluwer Series, **E345**, 105, 1997. ➪14

[135] W. Krauth. *Introduction to Monte Carlo algorithms*. arXiv:cond-mat, 9612186, 1996. ➪21

[136] F. Kuchar, H. Heinrich, and G. Bauer. *Localization and confinement of electrons in semiconductors*. Springer-Verlag, 1990. ➪1

[137] S. Kümmel. *Private communication*. ➪60

[138] S. Kümmel. *Structural and optical properties of sodium clusters studied in density functional theory*. PhD thesis, Universität Regensburg, 2000. ➪57, 58, 59

[139] S. Kümmel, M. Brack, and P.G. Reinhard. *Ionic and electronic structure of sodium clusters up to* $N = 59$. Phys. Rev. B, **62** (11), 7602, 2000. ➪58, 59, 60

[140] R.E. Kunz and R.S. Berry. *Coexistence of multiple phases in finite systems*. Phys. Rev. Lett., **71** (24), 3987, 1993. ➪68

[141] R.E. Kunz and R.S. Berry. *Multiple phase coexistence in finite systems*. Phys. Rev. E, **49** (3), 1895, 1994. ➪74

[142] R. Kusche, Th. Hippler, M. Schmidt, B. von Issendorf, and H. Haberland. *Melting of free sodium clusters*. Eur. Phys. J. D, **9**, 1, 1999. ➪57

[143] P. Labastie and R.L. Whetten. *Statistical thermodynamics of the cluster solid-liquid transition*. Phys. Rev. Lett., **65** (13), 1567, 1990. ➪74

[144] R.B. Laughlin. *Anomalous quantum Hall effect: An incompressible quantum fluid with fractionally charged excitations*. Phys. Rev. Lett., **50** (18), 1395, 1983. ➪7

[145] R.B. Laughlin. *Quantized motion of three two-dimensional electrons in a strong magnetic field*. Phys. Rev. B, **27** (6), 3383, 1983. ➪14

[146] K. Lee and J. Callaway. *Electronic structure and magnetism of small V and Cr clusters*. Phys. Rev. B, **48** (20), 15358, 1993. ➪36

[147] A. Lorke, R.J. Luyken, A.O. Govorov, J.P. Kotthaus, J.M. Garcia, and P.M. Petroff. *Spectroscopy of nanoscopic semiconductor rings*. Phys. Rev. Lett., **84** (10), 2223, 2000. ➪2, 8, 12, 42

[148] D. Loss and P. DiVincenzo. *Quantum computation with quantum dots*. Phys. Rev. A, **57** (1), 120, 1998. ➪47

[149] S. Lüscher, A. Fuhrer, R. Held, T. Heinzel, K. Ensslin, W. Wegscheider, and M. Bichler. *In-plane gate single electron transistor fabricated by AFM lithography*. J. Low Temp. Phys., **118**, 333, 2000. ➪10, 47

[150] A.P. Lyubartsev and P.N. Vorontsov-Velayaminov. *Path integral Monte Carlo method in quantum statistics for a system of N identical fermions*. Phys. Rev. A, **48** (6), 4075, 1993. ➪23

[151] M. Macucci, K. Hess, and G.J. Iafrate. *Electronic energy spectrum and the concept of capacitance in quantum dots*. Phys. Rev. B, **48** (23), 17354, 1993. ➪15

[152] D. Mailly, C. Chapelier, and A. Benoit. *Experimental observation of persistent currents in a GaAs-AlGaAs single loop*. Phys. Rev. Lett., **70** (13), 2020, 1993. ➪8, 42

[153] C.H. Mak, R. Egger, and H. Weber-Gottschick. *Multilevel blocking approach to the fermion sign problem in path-integral Monte Carlo simulations*. Phys. Rev. Lett., **81**, 4533, 1998. ➪32, 36

[154] P.A. Maksym and T. Chakraborty. *Quantum dots in a magnetic field: Role of electron-electron interactions*. Phys. Rev. Lett., **65** (1), 108, 1990. ➪14, 15

[155] H.C. Manoharan, C.P. Lutz, and D.M. Eigler. *Quantum mirages formed by coherent projection of electronic structure*. Nature, **403**, 512, 2000. ➪1

[156] D.W. Marquardt. *An algorithm for the least-squares estimation of nonlinear parameters*. J. Soc. Ind. Appl. Math., **11** (2), 431, 1963. ➪62

[157] J.L. Martins and J. Buttet. *Equilibrium geometries and electronic structures of small sodium clusters*. Phys. Rev. Lett., **53** (7), 655, 1984. ➪57, 59, 60

[158] J.L. Martins, J. Buttet, and R. Car. *Electronic and structural properties of sodium clusters*. Phys. Rev. B, **31** (4), 1804, 1985. ➪57, 59, 60, 61

[159] T. Mayer-Kuckuk. *Atomphysik*. Teubner Studienbücher, 5th edition, 1997. ➪13

[160] U. Merkt, J. Huser, and M. Wagner. *Energy spectra of two electrons in a harmonic quantum dot*. Phys. Rev. B, **43** (9), 7320, 1991. ➪14

[161] N. Metropolis, A. Rosenbluth, N.N. Rosenbluth, A.H. Teller, and E. Teller. *Equation of state calculations by fast computing machines*. J. Chem. Phys., **21** (6), 1087, 1953. ➪21

[162] K. Mishima, K. Yamashita, and A. Bandrauk. *Isomers and transition states of the* Na_4^+ *clusters. Ab initio studies of geometries and absorption spectra*. J. Phys. Chem. A, **102** (18), 3157, 1998. ➪57, 61, 62, 63

[163] I. Morgenstern. *Quantum Monte Carlo simulations for fermionic systems*. Z. Phys. B, **77**, 267, 1989. ➪23, 36

[164] I. Moullet, J.L. Martins, F. Reuse, and J. Buttet. *Static electric polarizabilities of sodium clusters*. Phys. Rev. B, **42** (18), 11598, 1990. ➪57, 59, 60

[165] O.G. Mouritsen. *Computer studies of phase transitions and critical phenomena*. Springer-Verlag, 1984. ➪74

[166] O. Mülken, P. Borrmann, J. Harting, and H. Stamerjohanns. *Classification of phase transitions of finite BEC in power law traps by Fisher zeros*. Phys. Rev. A, **64**, 013611, 2001. ➪4, 80

[167] H.M. Müller and S.E. Koonin. *Phase transitions in quantum dots*. Phys. Rev. B, **54** (20), 14532, 1996. ➪14

[168] W.J. Mullin. *Bose-Einstein condensation in a harmonic potential*. J. Low Temp. Phys., **106** (5/6), 615, 1997. ➪80

[169] W.J. Mullin. *A study of Bose-Einstein condensation in a two-dimensional trapped gas*. J. Low Temp. Phys., **110** (1/2), 167, 1998. ➪80

[170] P. Navez, D. Bitouk, M. Gajda, Z. Idziaszek, and K. Rzazewski. *Fourth statistical ensemble for the Bose-Einstein condensate*. Phys. Rev. Lett., **79**, 1789, 1997. ➪68

[171] S.K. Nayak, Ramaswamy, and C. Chakravarty. *Maximal Lyapunov exponents in small atomic clusters*. Phys. Rev. E, **51**, 3376, 1995. ➪74

[172] W. H. Newman and A. Kuki. *Improved methods for path integral Monte Carlo integration in fermionic systems*. J. Chem. Phys., **96** (2), 1409, 1992. ➪23, 36

[173] T.H. Ooosterkamp, T. Fujisawa, W.G. van der Wiel, K. Ishibashi, R.V. Hijman, S. Tarucha, and L.P. Kouwenhoven. *Microwave spectroscopy of a quantum-dot molecule*. Nature, **395**, 873, 1998. ➪8, 47

[174] J.J. Palacios and P. Hawrylak. *Correlated few-electron states in vertical double-quantum-dot systems*. Phys. Rev. B, **51** (3), 1769, 1995. ➪8, 47

[175] J.J. Palacios, L. Martin-Moreno, G. Chiappe, E. Louis, and C. Tejedor. *Capacitance spectroscopy in quantum dots: Addition spectra and decrease of tunneling rates*. Phys. Rev. B, **50** (8), 5760, 1994. ➪14

[176] R.G. Parr and W. Yang. *Density functional theory of atoms and molecules*. Oxford University Press, 1989. ➪16

[177] S. Pearson, T. Pang, and C. Chen. *Bose-Einstein condensation in two dimensions: A quantum Monte Carlo study*. Phys. Rev. A, **58** (6), 4811, 1998. ➪80

[178] H. Perez Rojas. *On Bose condensation in any dimension*. Phys. Lett. A, **234**, 13, 1997. ➪80

[179] P.M. Petroff and S.P. Denbaars. *MBE and MOCVD growth and properties of self-assembling quantum dot arrays in III-V semiconductor structures*. Superlattices and Microstructures, **15**, 15, 1994. ➪11

[180] P.M. Petroff, A.C. Gossard, R.A. Logan, and W. Wiegmann. *Toward quantum well wires: Fabrication and optical properties*. Appl. Phys. Lett., **41**, 635, 1982. ➪7

[181] D. Pfannkuche, V. Gudmundsson, and P.A. Maksym. *Comparison of a Hartree, a Hartree-Fock, and an exact treatment of quantum-dot helium*. Phys. Rev. B, **47** (4), 2244, 1993. ➪14, 36

[182] R. Pino. *Exact solution of the Thomas-Fermi two-dimensional N-electron quantum dot*. Phys. Rev. B, **58** (8), 4644, 1998. ➪36

[183] R. Poteau and F. Spiegelmann. *Distance-dependent Hückel-type model for the study of sodium clusters*. Phys. Rev. B, **45** (4), 1878, 1992. ➪57

[184] W.H. Press, S.A. Teukolsky, W.T. Vetterling, and B.P. Flannery. *Numerical recipes in Fortran 77 - the art of scientific computing*, volume I. EXXON Research and Engineering Company, 2nd edition, 1996. ➪21

[185] A. Proykova and R.S. Berry. *Analogues in clusters of second-order phase transitions*. Z. Phys. D, **40**, 215, 1997. ➪74

[186] D. Rayane, A.R. Allouche, E. Benichou, R. Antoine, M. Aubert-Frecon, Ph. Dugourd, and M. Broyer. *Static electric dipole polarizabilities of alkali clusters*. Eur. Phys. J. D, **9**, 243, 1999. ➪57

[187] M.A. Reed. *Quantum dots*. Scientific American, **268** (1), 118, 1993. ➪7

[188] M.A. Reed, R.T. Bate, K. Bradshaw, W.M. Duncan, W.M. Frensley, J.W. Lee, and H.D. Smith. *Spatial quantization in GaAs-AlGaAs multiple quantum dots*. J. Vacuum Sci. Tech. B, **4**, 358, 1986. ➪7, 9

[189] B. Reusch, W. Häusler, and H. Grabert. *Wigner Molecules in quantum dots*. Phys. Rev. B, **63**, 113313, 2001. ➪14

[190] M.C. Roco, S. Williams, and P. Alivisatos. *Nanotechnology research directions*. IWGN Workshop Report, 1999. ➪1

[191] G. Roepstorff. *Path integral approach to quantum physics*. Springer-Verlag, 2nd edition, 1996. ➪19

[192] A. Rytkönen and M. Manninen. *Fragmentation of small sodium clusters*. J. Chem. Phys., **113** (11), 4647, 2000. ➪57

[193] A.I. Safonov, S.A. Vasilyev, I.S. Yasnikov, I.I. Lukashevich, and S. Jaakkola. *Observation of quasicondensate in two-dimensional atomic hydrogen*. Phys. Rev. Lett., **81** (21), 4545, 1998. ➪80

[194] M. Schmidt, C. Ellert, W. Kronmüller, and H. Haberland. *Temperature dependence of the optical response of sodium cluster ions Na*$_n^+$*, with* $4 \leq n \leq 16$. Phys. Rev. B, **59** (16), 10970, 1999. ➪57

[195] M. Schmidt, B. von Issendorf, and H. Haberland. *Irregular variations in the melting point of size-selected atomic clusters*. Nature, **393**, 238, 1998. ➪74

[196] T. Schmidt, R.J. Haug, K. v. Klitzing, A. Förster, and H. Lüth. *Spectroscopy of the single-particle states of a quantum-dot molecule*. Phys. Rev. Lett., **78** (8), 1544, 1997. ➪8, 47

[197] H.W. Schumacher, U.F. Keyser, U. Zeitler, R.J. Haug, and K. Eberl. *Nanomachining of mesoscopic electronic devices using an atomic force microscope*. Appl. Phys. Lett., **75** (8), 1107, 1999. ➪47

[198] A.Y. Shik. *Quantum wells – Physics and electronics of two-dimensional systems*. World Scientific Publishing Co Pte Ltd., 1998. ➪1, 7, 14

[199] G. Springholz, M. Pinczolits, P. Mayer, V. Holy, G. Bauer, H.H. Kang, and L. Salamanca-Riba. *Tuning of vertical and lateral correlations in self-organized PbSe/Pb*$_{1-x}$*Eu*$_x$*Te quantum dot superlattices*. Phys. Rev. Lett., **84**, 4669, 2000. ➪11

[200] A. Staene. *Quantum computing*. Rep. Prog. Phys., **61** (2), 117, 1998. ➪47

[201] D.M. Stamper-Kurn, M.R. Andrews, A.P. Chikkatur, S. Inouye, H.-J. Miesner, J. Stenger, and W. Ketterle. *Optical confinement of a Bose-Einstein condensate*. Phys. Rev. Lett., **80** (10), 2027, 1998. ➪68, 80

[202] M. Stopa. *Quantum dot self-consistent electronic structure and the Coulomb blockade*. Phys. Rev. B, **54** (19), 13767, 1996. ➪15

[203] I.N. Stranski and L. Krastanow. Akad. Wiss. Let. Mainz Math. Natur K1 IIb, **146**, 797, 1939. ➪11

[204] M. Takahashi and M. Imada. *Monte Carlo calculations of quantum systems*. J. Phys. Soc. Jpn., **53** (3), 936, 1984. ➪20, 21, 24, 36, 42

[205] M. Takahashi and M. Imada. *Monte Carlo calculations of quantum systems. II. Higher order correction*. J. Phys. Soc. Jpn., **53** (11), 3765, 1984. ➪20, 36, 42

[206] S. Tarucha, D.G. Austing, and T. Honda. *Shell filling and spin effects in a few electron quantum dot*. Phys. Rev. Lett., **77** (17), 3613, 1996. ➪2, 13, 36

[207] H. Temkin, G.J. Dolan, M.B. Panish, and S.N.G. Chu. *Low-temperature photoluminescence from InGaAs/InP quantum wires and boxes*. Appl. Phys. Lett., **50**, 413, 1987. ➪7

[208] D.J. Thouless. *The quantum mechanics of many-body systems*. BI Hochschultaschenbücher, 1961. ➪14

[209] E.C. Titchmarsh. *The theory of functions*. Oxford University Press, 1964. ➪74

[210] H.F. Trotter. *On the product of semi-groups of operators*. Proc. Math. Soc. Am., **10**, 545, 1959. ➪19

[211] D.C. Tsui, H.L. Störmer, and A.C. Gossard. *Two-dimensional magnetotransport in the extreme quantum limit*. Phys. Rev. Lett., **48** (22), 1559, 1982. ➪7

[212] W.G. van der Wiel, T. Fujisawa, T.H. Ooosterkamp, and L.P. Kouwenhoven. *Microwave spectroscopy of a quantum dot in the low- and high-power regime*. Physica B: Condensed Matter, **272**, 31, 1999. ➪47

[213] D.J. Wales and R.S. Berry. *Melting and freezing of small Argon clusters*. J. Chem. Phys., **92**, 4283, 1990. ➪74

[214] D.J. Wales and R.S. Berry. *Coexistence in finite systems*. Phys. Rev. Lett., **73**, 2875, 1994. ➪68

[215] R.J. Warburton, C. Schäflein, D. Haft, F. Bickel, A. Lorke, K. Karrai, J.M. Garcia, W. Schoenfeld, and P.M. Petroff. *Optical emission from a charge-tunable quantum ring*. Nature, **405**, 926, 2000. ➪2, 42

[216] C. Weiss and M. Wilkens. *Particle number counting statistics in ideal Bose gases*. Optics Express, **1** (10), 272, 1997. ➪68

[217] L. Wendler and V.M. Fomin. *Persistent currents in finite-width mesoscopic rings*. Phys. Stat. Sol. B, **191**, 409, 1995. ➪8, 42

[218] L. Wendler, V.M. Fomin, A.V. Chaplik, and A.O. Govorov. *Optical properties of two interacting electrons in quantum rings: Optical absorption and inelastic light scattering*. Phys. Rev. B, **54** (7), 4794, 1996. ➪8, 42

[219] E. Wigner. *On the interaction of electrons in metals*. Phys. Rev., **46** (11), 1002, 1934. ➪36

[220] Interagency working group on nanoscience – engineering and technology. *Nanotechnology - Shaping the world atom by atom*. IWGN, 1999. ➪1

[221] K. Yabana and G.F. Bertsch. *Time-dependent local-density approximation in real time*. Phys. Rev. B, **54** (7), 4484, 1996. ➪57

[222] Z. Yan. *Bose-Einstein condensation of a trapped gas in n dimensions*. Phys. Rev. A, **59** (6), 4657, 1999. ➪80

[223] C.N. Yang and T.D. Lee. *Statistical theory of equations of state and phase transitions, I. Condensation*. Phys. Rev., **97** (3), 404, 1952. ➪74, 80

[224] C.N. Yang and T.D. Lee. *Statistical theory of equations of state and phase transitions, II. Lattice gas and Ising model*. Phys. Rev., **87** (3), 410, 1952. ➪74, 80

[225] C. Yannouleas and U. Landman. *Spantaneous symmetry breaking in single and molecular quantum dots*. Phys. Rev. Lett., **82**, 5325, 1998. ➪14, 36, 42

[226] N.B. Zhitenev, R.C. Ashoori, L.N. Pfeiffer, and K.W. West. *Periodic and aperiodic bunching in the addition spectra of quantum dots*. Phys. Rev. Lett., **79**, 2308, 1997. ➪36

Acknowledgment

First, I would like to thank the members of the small systems group for the great work atmosphere. The last few years have been very productive and more like working with friends than with colleagues from work.

Special thank goes to Peter Borrmann. Without his ideas and skills, this thesis would not have been possible. His encouragement and critique led to many new insights, and it was a great pleasure being in his group. For me, it was a major loss when he had to leave the university.

It has been a pleasure to spend most of the time in close contact to Oliver Mülken. Fruitful discussions, friendly talks, useful comments, similar problems, good times, and the stimulating smell from his coffee machine always filled the air in our office(s).

Heinrich Stamerjohanns has been a great officemate and his computer experience made it seem like we were working in a 'biotope'. While everybody was talking about problems with the computer infrastructure, the words 'downtime' or 'crash' were never heard at our place.

Eberhard Hilf was always available to answer my questions and I benefitted from his great experience many times. He even spent his free time proofreading the manuscript and his comments were very encouraging. Thank you, Ebs !

My financial situation has been a little uncertain after the expiration of my university position. I would like to thank Martin Holthaus and Birger Kollmeier for their unconventional support in the last few months and Jutta Kunz-Drolshagen for her engagement to find new ways of funding.

I wish to thank Matti Manninen and Martin Holthaus for refereeing this thesis.

Matt Bulow read most of the manuscript and helped me to straighten out the linguistic deficiencies of the text. Thank you for being my LEKTOR !

I am deeply grateful to my parents for supporting me for the last 27 years and enabling me to study the most exciting field there is: Physics.

Thank you Christine, for your support over the last months, your helpful comments, and for just being there.

Curriculum Vitae

Name:	Jens Harting
Date of birth:	January, 9th 1974
Place of birth:	Twistringen
Citizenship:	German

School

1980 - 1984	Primary school: Grundschule Twistringen
1984 - 1993	High school: Gymnasium Syke
1993	Graduation: Abitur

University

1993 - 1995	Undergraduate studies, University of Oldenburg
1995	Vordiplom
1995 - 1998	Graduate studies, University of Oldenburg
1998 - 1999	Diploma thesis: ’Bose-Einstein Kondensation in magnetischen und optischen Fallen’
1999	Diploma
1999 - 2001	Doctoral candidate, University of Oldenburg

Statements

Comment on my contributions to the work presented in this thesis

The first part of this thesis is based on my own intensive review of the literature on path integral methods and nanoscopic semiconductor structures. I also performed the convergence studies presented in Section 3 of Chapter I-2.

The path integral Monte Carlo code used for the simulations presented in Part II was originally written and developed by P. Borrmann. Later improvements and enhancements of the code have been implemented by both of us. I performed most of the numerical simulations and wrote all of the shell scripts and Fortran programs used to automate the simulation process. While I have been in charge of the technical part of the data analysis including graphics and data handling, all authors of the published articles contributed by discussing the results and suggesting various simulation configurations. I created the graphics and tables in the published articles and refined them after discussions. I contributed sections to Chapter II-1 and wrote the first draft of Chapter II-2. The basic concepts presented in Chapter II-3 were developed in cooperation with P. Borrmann, and all further work including needed changes of the code and data analysis I performed myself. Chapter II-4 is based on an idea of P. Borrmann, who also introduced the pseudopotential to the program. I contributed the numerical simulations and data analysis.

My contributions to Chapter III-1 were the analytical reference calculations of the one-particle energy eigenvalues and their numerical implementation. Furthermore, I did the numerical simulations using P. Borrmann's Fortran code for his recursion formula, and I have been deeply involved in the whole publication process.

The classification scheme of Chapter III-2 and III-3 was developed by P. Borrmann and O. Mülken. I wrote the Fortran program used to perform the numerical studies of the properties of Bose-Einstein condensates. It utilizes the recursion formulae given in [28] and Chapter III-1 to calculate the ground state occupation numbers and specific heats as presented in Chapters III-2 and III-3. Additionally, I took part in the discussions during the publication process of the article presented in Chapter III-2 and contributed to the introduction of Chapter III-3.

Erklärung gemäß §8(2) der Promotionsordnung

Ich versichere hiermit, daß ich die vorliegende Arbeit selbst verfaßt und keine anderen als die angegebenen Quellen und Hilfsmittel verwendet habe.

Oldenburg, den 3. Januar 2002

(Jens Harting)